Novel Organic Materials for Light Emitting Diodes and Neuromorphic Devices

by

Samuel Shin

A Dissertation Presented in Partial Fulfilment
of the Requirements for the Degree
Doctor of Philosophy

Approved July 2021 by the
Graduate Supervisory Committee:

Jian Li, Chair
James Adams
Terry Alford

ARIZONA STATE UNIVERSITY

August 2021

ABSTRACT

Organic materials have emerged as an attractive component of electronics over the past few decades, particularly in the development of efficient and stable organic light-emitting diodes (OLEDs) and organic neuromorphic devices. The electrical, chemical, physical, and optical studies of organic materials and their corresponding devices have been conducted for efficient and stable electronics.

The development of efficient and stable deep blue OLED devices remains a challenge that has obstructed the progress of large-scale OLED commercialization. One approach was taken to achieve a deep blue emitter through a color tuning strategy. A new complex, PtNONS56-dtb, was designed and synthesized by controlling the energy gap between T_1 and T_2 energy states to achieve narrowed and blueshifted emission spectra. This emitter material showed an emission spectrum at 460 nm with a FWHM of 59 nm at room temperature in PMMA, and the PtNONS56-dtb-based device exhibited a peak EQE of 8.5% with CIE coordinates of (0.14, 0.27).

A newly developed host and electron blocking materials were demonstrated to achieve efficient and stable OLED devices. The indolocarbazole-based materials were designed to have good hole mobility and high triplet energy. BCN34 as an electron blocking material achieved the estimated LT_{80} of 12509 h at 1000 cd m^{-2} with a peak EQE of 30.3% in devices employing Pd3O3 emitter. Additionally, a device with bi-layer emissive layer structure, using BCN34 and CBP as host materials doped with PtN3N emitter, achieved a peak EQE of 16.5% with the LT_{97} of 351 h at 1000 cd m^{-2}.

A new neuromorphic device using $Ru(bpy)_3(PF_6)_2$ as an active layer was designed to emulate the short-term characteristics of a biological synapse. This memristive device showed a similar operational mechanism with biological synapse through the movement of ions and electronic charges. Furthermore, the performance of the device showed tunability by adding salt. Ultimately, the device with 2% $LiClO_4$ salt shows similar timescales to short-term plasticity characteristics of biological synapses.

ACKNOWLEDGEMENTS

I firstly would like to thank my advisor, Dr. Jian Li. He graciously gave me an opportunity to work in exciting projects about OLED devices and has shown me steadfast support for my research at Arizona State University. Over the past four years, he challenged my thinking as a Ph.D. student and guided my professional development. I appreciate his patience and guidance, which could make my work possible. Additional thanks are owed to Dr. Zhi-Qiang Zhu for his teaching about chemical synthesis and being a friend of mine. I also want to thank my friends, Linyu Cao and Lydia Ameri, for helping in material synthesis and device testing.

Secondly, I would like to thank my mentor, Dr. Inho Kim. I could work in the Neuromorphic device engineering field for a year during my Ph.D. because he thankfully offered me to work at Korea Institute of Science and Technology. I appreciate his support and guidance that completely changed my attitude to research. Also, I owe thanks to Dr. Youngsuk Lee, who has been a good friend of mine in the Institute. My thanks are owed to all collaborating engineers who are not named here at Arizona State University and Korea Institute of Science and Technology.

Most of all, I thank my parents for their unfailing love, support, sacrifice, and prayer. Without them, I could not make this work. I also thank my sister and brother-in-law for their prayer and encouragement.

Finally, I thank almighty God.

TABLE OF CONTENTS

Page

LIST OF TABLES

Table Page

LIST OF FIGURES

Figure Page

Figure Page

Figure Page

Figure Page

Figure Page

Figure Page

Figure Page

LIST OF EQUATIONS

Equation Page

1. INTRODUCTION

1.1 Organic semiconductor

Organic semiconductors are under massive investigation as active layers in electronic devices owing to their low power consumption, low-temperature fabrication, capability to grow on flexible substrates, and tunability of their optical and electrical properties. These distinctive advantages make organic semiconductors desirable components in various applications such as organic light-emitting diodes (OLEDs) [1], organic photovoltaics (OPVs) [2], organic thin-film transistors (OTFTs) [3], and organic memristors [4]. Figure 1 shows the standard structures of the organic semiconductor devices.

Fundamental properties of organic semiconductors are typically attributed to the combination of their atomic constituents and band structures, which will be demonstrated in detail by using a comparison between organic semiconductors and conventional inorganic semiconductors.

First of all, inorganic semiconductors are mainly crystalline structures composed of one or a few atoms, such as silicon, germanium, or gallium arsenide. These atoms are covalently bonded to each other, making inorganic semiconductors generally hard and brittle with a high melting point [5]. On the other hand, organic semiconductors are typically pi-bonded molecules made up of carbon and hydrogen atoms. Their composition can also include nitrogen, oxygen, sulfur, or some transition metals. These molecules are bound by weak van der Waals force in bulk, which leads to amorphous

arrangements of organic molecules. This is why organic semiconductors are usually soft and light with a low melting point [6].

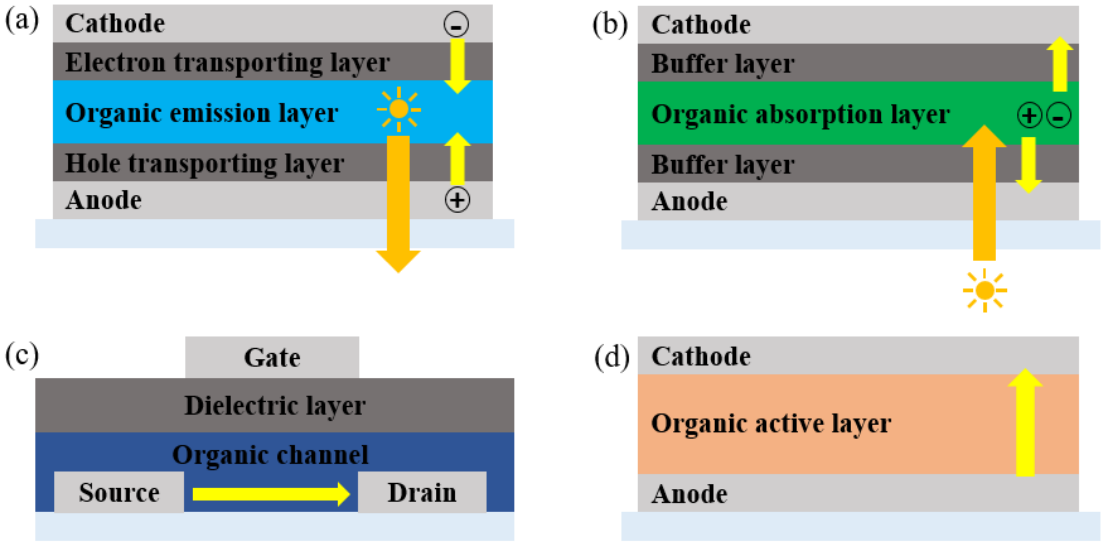

Figure 1. Schematic showing of the standard structures in organic semiconductor devices. (a) organic light-emitting diodes (OLEDs), (b) organic photovoltaics (OPVs), (C) organic thin-film transistors (OTFTs), and (d) organic memristor.

Secondly, inorganic semiconductors usually consist of a single crystal with minor defects. This well-ordered and close-packed structure across the crystal allows the element to form continuous bands of electron orbitals known as conduction band and valence band. Also, there is a bandgap between the conduction and valence bands where no electronic states can exist (Figure 2a). The valence band is normally filled with electrons, while the conduction band is partially filled or vacant of electrons depending on temperature because the Fermi level of an intrinsic semiconductor is located in the bandgap. However, the inorganic semiconductor can conduct electrical current when the conduction band is occupied with electrons through electrical, optical, or thermal excitation [7]. On the other hand, organic semiconductors comprise randomly oriented

molecules that are loosely bound by van der Waals force based on weak dipole-dipole interactions [8]. This amorphous arrangement and chemical impurities let the charge carriers localize each molecule and form discontinuous energy levels.

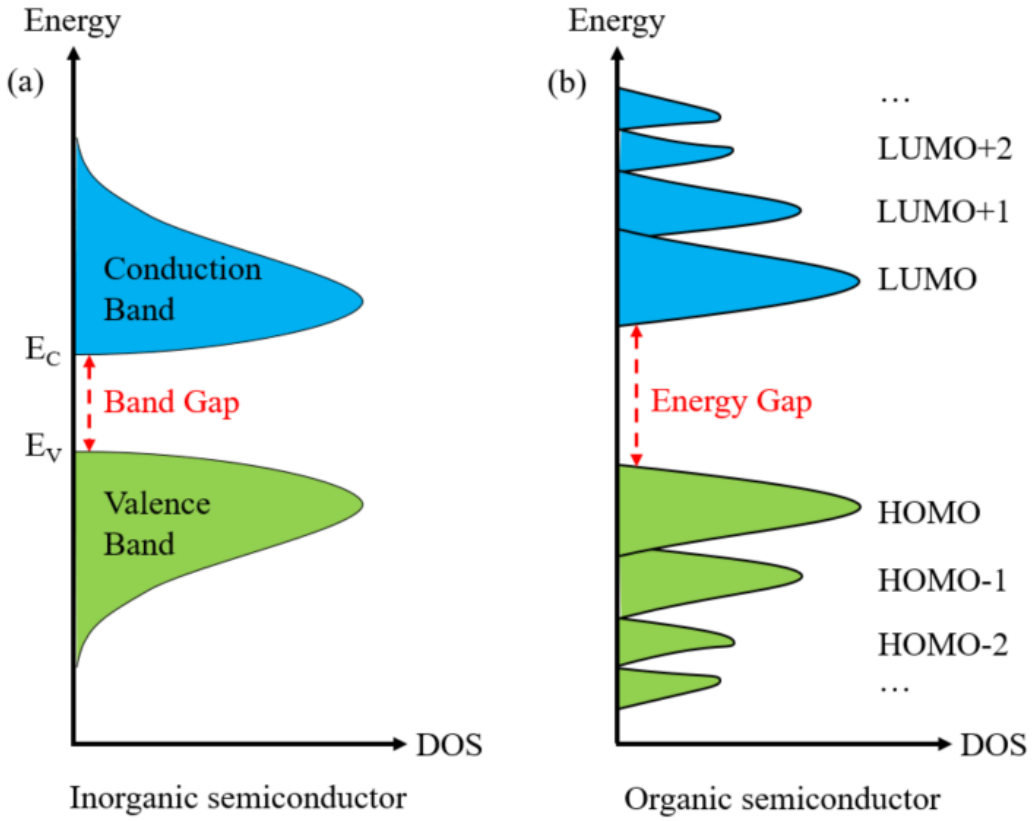

Figure 2. The density of states (DOS) diagram of (a) inorganic semiconductors and (b) organic semiconductors.

The discrete energy levels in organic semiconductors are named highest occupied molecular orbital (HOMO) and lowest unoccupied molecular orbital (LUMO), corresponding to the valence band edge (E_V) and conduction band edge (E_C) of the inorganic counterparts, respectively, as shown in Figure 2b. The molecular orbitals below the HOMO and above the LUMO are referred to as HOMO-1, HOMO-2, … and

LUMO+1, LUMO+2, …, respectively. The energy gap and the frontier molecular orbitals, including HOMO and LUMO, play a crucial role in determining the electrical and optical properties of the organic semiconductors, such as charge transport, absorption, and emission.

The charge transport in organic semiconductors is primarily governed by the weak intermolecular coupling of amorphous materials. Therefore, the charge migration mechanism of organic semiconductors is limited by hopping between localized sites instead of delocalized charge transport in bands [9]. Compared with the inorganic semiconductor mobility (coherent band transport, $\mu > 1000$ cm^2/Vs for the electron in Si), the mobility of organic semiconductors (incoherent hopping transport) is limited to $\mu <$ 0.1 cm^2/Vs as demonstrated in Figure 3 [10].

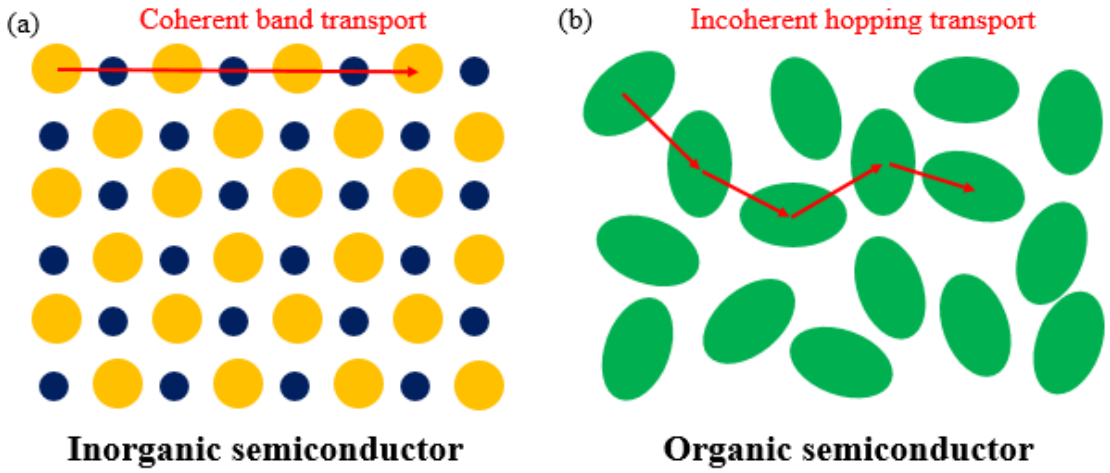

Figure 3. The charge transporting mechanisms of (a) inorganic semiconductors and (b) organic semiconductors.

Due to the large energy gap of organic semiconductor (3-5 eV), its concentration of intrinsic charge carrier is negligible, which cause that the organic semiconductor is intrinsically an insulator, and its charge conduction depends on the injected charges from the electrodes or intentionally doped structure.

When light is absorbed in organic semiconductors, an electron in the HOMO jumps to the LUMO or higher energy orbitals and leaves a hole in HOMO. Then these electrons and holes are attracted by Coulomb force and form Frenkel excitons localized on a single molecule. These excitons are transferred between molecules, and this exciton energy transfer can affect the performance of organic electronics such as OLEDs and organic memristors.

Additionally, organic semiconductors can be grown on any medium substrate due to their amorphous characteristics, which is different from inorganic semiconductors that require lattice-matching. As long as the surface is atomically smooth, the organic semiconductors can be deposited on flexible substrates, which enable fordable, curved, or stretchable electronics.

1.2 Organic light-emitting diodes

Among the many applications of organic electronics, organic light-emitting diode (OLED) is one of the widely used components in electronic devices. Particularly, the advantages of the OLEDs such as low power consumption, ability to be fabricated on flexible substrates, and tunability of optoelectronic properties have made them to be used in the displays of smart phones and televisions as demonstrated in Figure 4 [11]–[13].

Figure 4. Personal electronics employing OLEDs. Images of Samsung fordable smartphone, LG curved television, and LG rollable television are included.

1.2.1. A brief history of OLEDs

The first electroluminescence spectra in organic materials were observed in the 1960s by applying a voltage to anthracene and tetracene-doped anthracene crystals [14]. And the first efficient OLED was demonstrated by Tang and VanSlyke in 1987 using a fluorescent emitter, tris(8-hydroxyquinolinato)aluminum (Alq_3) [1]. This first OLED device achieved high external quantum efficiency (EQE) of ~1% with a multilayer structure, composing indium-tin-oxide (ITO) as the anode, 4,4′-Cyclohexylidenebis[N,N-bis(4-methylphenyl)benzenamine] (TATC) as the hole transporting layer (HTL), Alq_3 as the electron transporting layer (ETL) and the emissive layer (EML), and Mg:Ag as the cathode. Then, the host-guest system was first applied by doping a small volume of fluorescent dopant in a host material by Tang in 1989 and achieved EQE of 2.5% [15]. These advanced systems, incorporating multilayer and host-guest structures, have been primarily adopted in OLED devices these days. The multilayer structure and host-guest systems will be discussed in Chapter 3 in detail.

The first generation of OLED devices has employed fluorescent emitters that only harvest singlet excitons. Since the singlet exciton is a quarter of the generated excitons, the internal quantum efficiency (IQE) is limited to 25%. However, Forrest and Thompson dramatically increased the efficiency of OLED devices by utilizing both singlet and triplet excitons through strong spin-orbit coupling (SOC) with heavy metals such as Pt(II) [16] and Ir(III) [17] in 1998. The devices using this mechanism, which is called phosphorescent OLED, could achieve 100% of IQE. Nowadays, efficient red and green OLED devices employ phosphorescent emitters because they show higher efficiency than fluorescent emitters. The phosphorescent emitters will be discussed in Chapter 2 in detail. Another important approach of utilizing both singlet and triplet excitons is the delayed fluorescence process through the lowest triplet energy state (T_1) to the lowest singlet energy state (S_1) up-conversion. In order to overcome the intrinsic limitation of fluorescent device efficiency, thermally assisted delayed fluorescence (TADF) OLEDs have been developed and achieved 100% IQE through a brilliant molecular design strategy in 2012 [18]. Although the high efficiency TADF OLED devices have been reported, the operational stability of devices is insufficient to be commercialized [19], [20].

1.2.2. OLED operational principals

Advanced OLED devices are comprised of several functional organic and organometallic layers sandwiched between two electrodes. Figure 5 shows the standard OLED device structure. The organic layers adjacent to the electrodes are called the hole injection layer (HIL) and electron injection layer (EIL) that are for facilitating the charge injection. The injected holes and electrons are transported through the hole transporting

layer (HTL) and electron transporting layer (ETL), respectively. Then, charges can recombine within the emissive layer (EML), and the recombined electrons and holes generate photons via the electroluminescence process. Electron blocking layer (EBL) and hole blocking layer (HBL) can also be employed to confine charges within the EML because of the imbalanced electron and hole transporting abilities of organic materials. The requirements and examples of EBL will be discussed in Chapter 3 in detail.

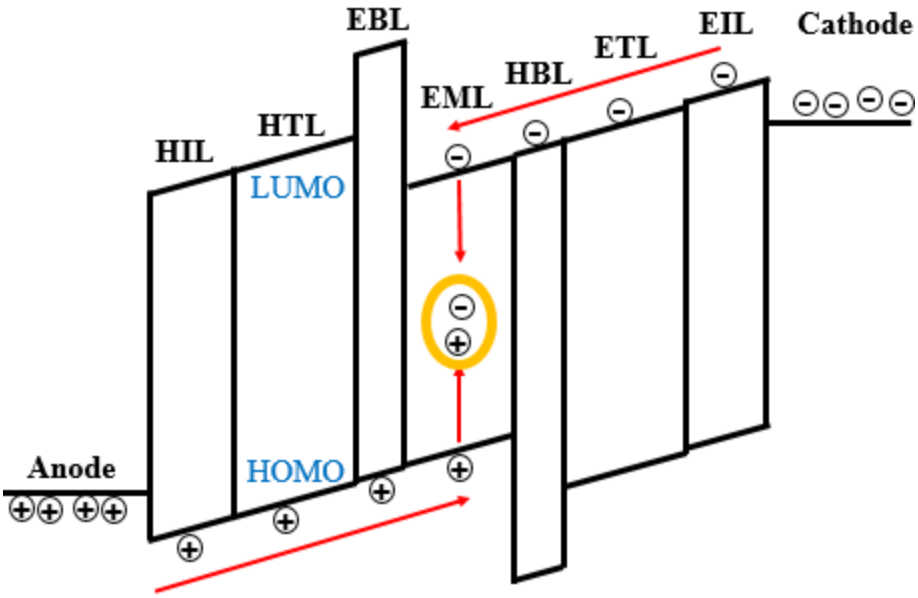

Figure 5. A standard OLED device structure.

For the discussion of OLED operations, it is crucial to understand the concepts of hole and electron. The electron is a negatively charged subatomic particle. On the other hand, a hole, which does not physically exist, is a positive charge that occurs after an electron is missing. Figure 6 shows HOMO and LUMO level occupation in 4 different states.

The ground state is a neutral state of the molecule with a zero spin, representing the molecules in the OLED device before the external voltage is applied. A pair of electrons exist at the HOMO level, and the LUMO level is empty (Figure 6a). Figure 6b demonstrates a hole polaron which is a state of a positive charge on the molecule due to the missing of one electron. The positive charge pulls the HOMO and LUMO levels close to each other. The electron polaron state in Figure 6c is a molecule that gained an extra electron at the LUMO level, leading to a negative charge. In the OLED device structure, the hole polarons and electron polarons are generated at the anode, and cathode, respectively, when the external bias is applied. As mentioned above, the holes and electrons migrate via hopping towards the EML and form excitons as depicted in Figure 6d.

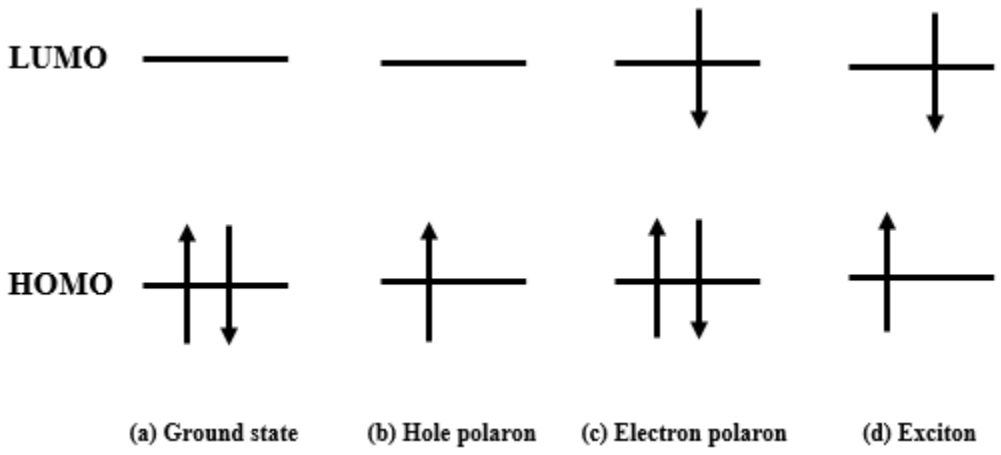

Figure 6. A Scheme of HOMO and LUMO level occupation in 4 different states, (a) ground state, (b) hole polaron, (c) electron polaron, and (d) exciton.

Frenkel exciton is formed in OLEDs because of the amorphous nature of organic films. The Pauli exclusion principle demonstrates that two or more identical fermions must not occupy the same quantum state within a quantum system at the same time. This indicates that a pair of electrons trying to occupy the same state must have opposite spins.

Two types of excitons exist, singlet excitons and triplet excitons. The spin statistics identify that only 25% of the electron pairs have opposite spins, and this exciton is commonly called a singlet exciton. The singlet excitons have a net spin value of 0 and show a short transient lifetime on the order of nanoseconds. On the other hand, the other 75% of the electron pairs will have the same direction or out of phase spins, which is referred to as triplet exciton. The triplet excitons have a net spin value of -1, 0, or 1 and show longer lifetimes on the order of microseconds. Singlet and triplet excitons will be discussed in detail below because they are the driving mechanism of fluorescent and phosphorescent emission, respectively.

There are two main processes that can explain excion diffusion, Föster resonant energy transfer (or dipole-dipole coupling) and Dexter energy transfer (or electron exchange). The diagrams of these two processes are depicted in Figure 7.

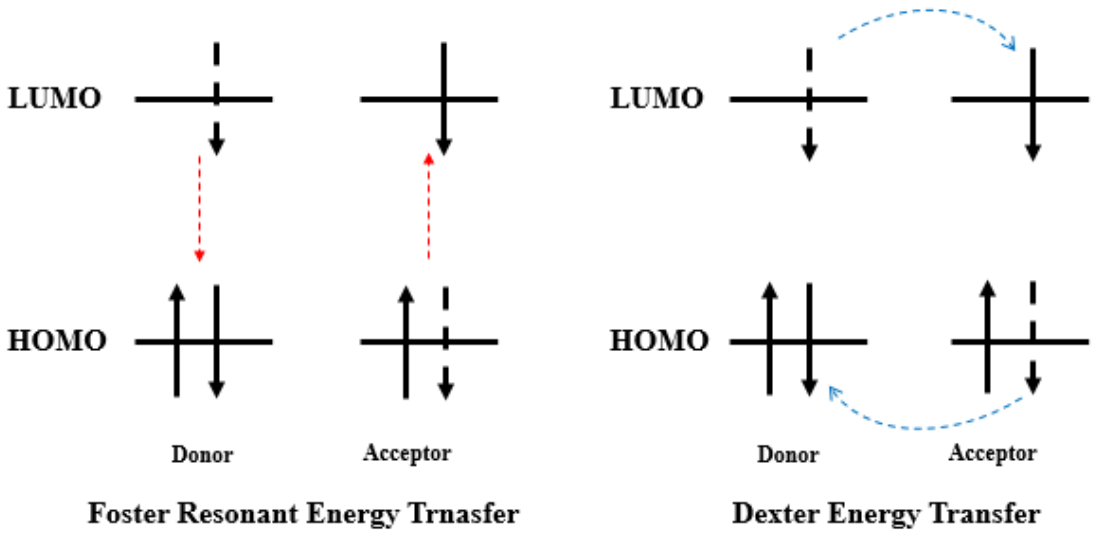

Figure 7. Diagram showing Foster resonant energy transfer and Dexter energy transfer.

Föster resonant energy transfer is a non-contact process that generally appears between molecules with a length scale of 1-10 nm. Between an excited molecule and a ground state molecule, the intermolecular dipole interaction can occur. Figure 7 shows that the energy is transferred through dipole coupling to an electron in the ground state molecule's HOMO level when an electron in the excited molecule's LUMO level relaxes to its HOMO level. This leads to an energy transfer that excites an electron in the ground state molecule's LUMO level.

On the other hand, Dexter energy transfer appears through a direct electron exchange when the excited molecule and ground state molecule are in close contact. Figure 7 demonstrates an electron in the excited molecule's LUMO level hops to the ground state molecule's LUMO level. At the same time, an electron in the ground state molecule's HOMO level hops to the excited molecule's HOMO level. Of these two processes, Föster resonant energy transfer occurs in OLEDs and is a driving process of

exciton diffusion.

Electroluminescence (EL) is a basic light-emitting process of OLEDs. When an exciton relaxes from the excited state to its ground state, a new generation of energy should accompany based on the law of conservation of energy. The newly generated energy is equal to the exciton starting energy. In the EL process in OLEDs, a photon is generated through the exciton relaxation.

A singlet exciton occupies a higher energy state comped to its triplet counterpart. In a pure organic material, singlet excitons generate fluorescent emission by decaying from their excited state to their ground state as shown in Figure 8. The timescale of transition from the S_1 state to the ground state (S_0) is around 1-100 ns. On the other hand, the transition from the S_1 state to the T_1 state is considerably slower (0.1-1 μs). These lead to nearly 100% radiative decay of singlet excitons. However, all the triplet excitons decay non-radiatively in fluorescent systems, which leads to a net exciton to the photon conversion efficiency of 25%.

In the case of phosphorescent systems, the triplet excitons can also decay radiatively by adding a transition metal to the organic molecule ligand. Spin-orbit coupling between the metal and the excitons allows radiative decay from the T_1 state to the S_0 state as depicted in Figure 8. This is because the S_1 state to T_1 state transition, which is called intersystem crossing (ISC), is faster than the S_1 state to S_0 state. Since the ISC process is fast and efficient, the phosphorescent emitters can achieve an exciton to the photon conversion efficiency of 100% by harvesting both singlet excitons and triplet excitons.

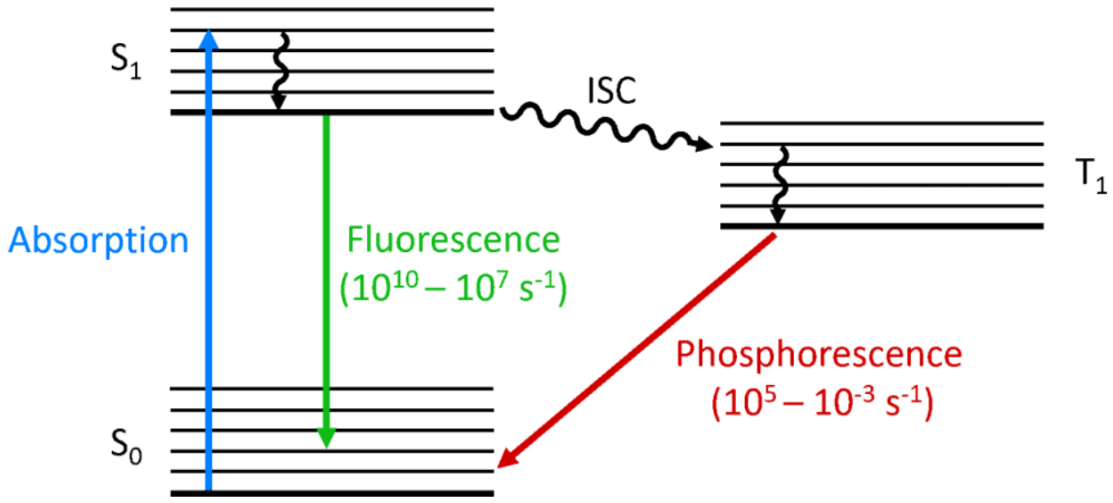

Figure 8. Jablonski diagram of fluorescence and phosphorescence processes.

Although the fluorescence and the phosphorescence are primarily used in commercial OLEDs, a new unique subset of fluorescent emission has been researched. It is referred to as Thermally activated delayed fluorescence (TADF). Delayed fluorescence is from reverse intersystem crossing (RISC), resulting in triplet excitons being up-converted to the singlet state to decay radiatively. The RISC singlet transition to S_0 shows much slower decay between microseconds and milliseconds than a standard singlet, which is a result of the excitons spending a long time in the triplet state. TADF occurs through the thermal excitations at room temperature, which provides enough energy to make RISC because the energy gap between S_1 and T_1 is reduced by designing organic materials.

OLED display emits the light directly from each RGB (Red, Green, and Blue) pixel, which is one of the reasons why OLEDs are preferable in display applications compared to conventional liquid crystal displays (LCDs). On the other hand, LCD has a

different mechanism filtering the white back-light to express the color, which makes it less efficient than OLEDs. Also, the improved contrast ratio and dynamic color range from the direct light-emitting demonstrate that the OLEDs are the future of displays. For a better understanding of the light emission process of OLED devices, the energy diagram in Figure 8 needs to be discussed in more detail.

Figure 8 shows a Jablonski diagram that has multiple vibronic states in organic molecules. When an organic molecule is excited by absorbing light or other energy, electrons jump from S_0 state to S_1 or S_2 state, depending on the applied energy. Then, the excited electrons will transit to S_1 state or T_1 state that was previously discussed. When the excited electrons decay from S_1 state or T_1 state to the S_0 state, the energy difference between S_0 state and those two excited states will stand for the emission energy of the material. Thus, it is crucial to consider all the vibronic states in organic emitters. In a real energy states system, there is a wide range of vibronic delocalized states due to the molecular distortions in the emitting molecule, thermal excitations, and vibrational energy. This results in the broad emission in OLEDs.

The electromagnetic spectrum is shown in Figure 9 to demonstrate a visual correlation between the wavelength and the emission color. In the next chapter, a more in-depth discussion of device testing, device physics, OLEDs performance parameters, and color coordinates will follow.

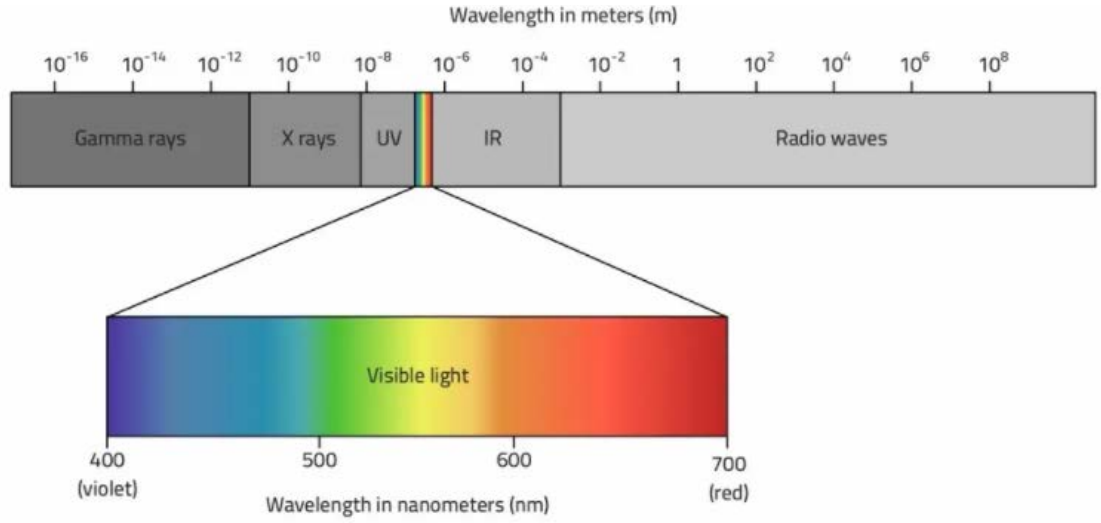

Figure 9. The electromagnetic spectrum in terms of wavelength.

1.2.3. OLED performance and characterization

In this chapter, the characterization for OLEDs and performance parameters are introduced and discussed. A widely used testing for OLED devices is the JVL test that stands for current density for J, voltage for V, and luminance for L. Figure 10a indicates a diagram of JVL test processing. A glass substrate is placed on a substrate holder that is in close contact with a silicon photodiode. Then, the OLED device is hooked up to the Keithley machine as a voltage source, and the voltage is swept from 0 V to higher voltage (generally ranging from 5-20 V). The current and resistance changes of the OLED device can be measured during the voltage swept. At the same time, the emitted light can be collected to a silicon photodiode that generates current to record using a high-resolution ammeter.

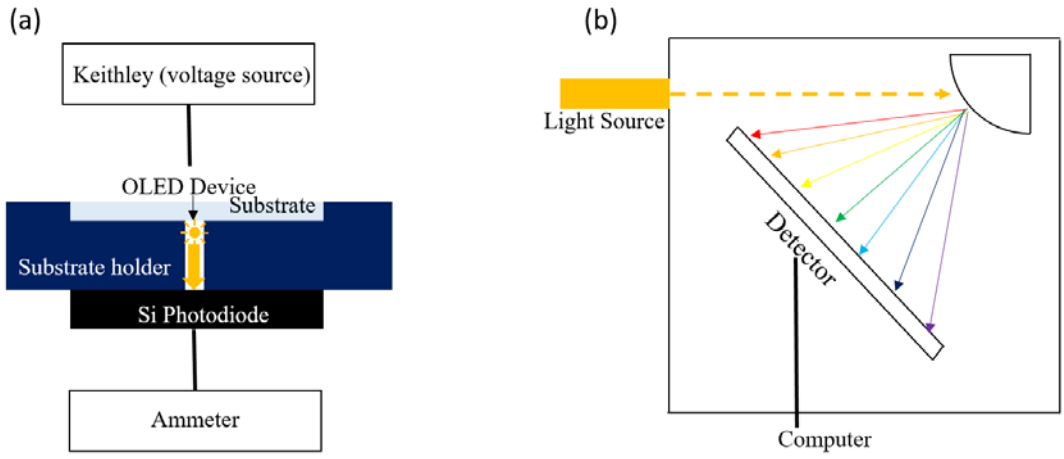

Figure 10. (a) Diagram of OLED JVL test and (b) schematic of spectrometer operation.

On the other hand, the electroluminescent spectra of the OLED device can be measured by using a spectrometer. Figure 10b demonstrates a scheme of the spectrometer operational mechanism. When light enters into the spectrometer, a diffraction grating reflects the incoming light. Then, the light diffracts at different angles according to its wavelength and is directed to a photodetector. Through the spectrometer, the light intensity versus wavelength graph can be obtained. And the brightness of the light from the OLED device can be calculated through the combination of the electroluminescence spectrum and the photodiode responsivity by converting the photocurrent into a value of lumens.

Through the JVL test and spectrometer data, various performance parameters can be acquired for evaluating OLED devices. The first commonly used performance parameter, power efficiency (PE), is a ratio of the power of the emitted light to the electrical power input, and its unit is lumens per watt (Lm/W). The power efficiency of OLED devices is a generally used metric for comparing to other lighting sources.

The second performance, EQE, is the efficiency of the injected hole-electron pairs to the emitted photon conversion process. The hole-electron pairs injected into the device and photons escaped from the device can be quantified by using the JV characteristic and the brightness, respectively. However, the JVL measurement cannot collect all the photons emitted from the device because there are losses of photons at high angle emission. This loss value (i.e., geometry factor) can be calculated through a calibrated device with brightness to avoid undercalculating the EQE of OLED devices. And the most accurate method to measure the brightness of the OLED device is integrating sphere. This technique can measure all directions of emitted light of the OLED device.

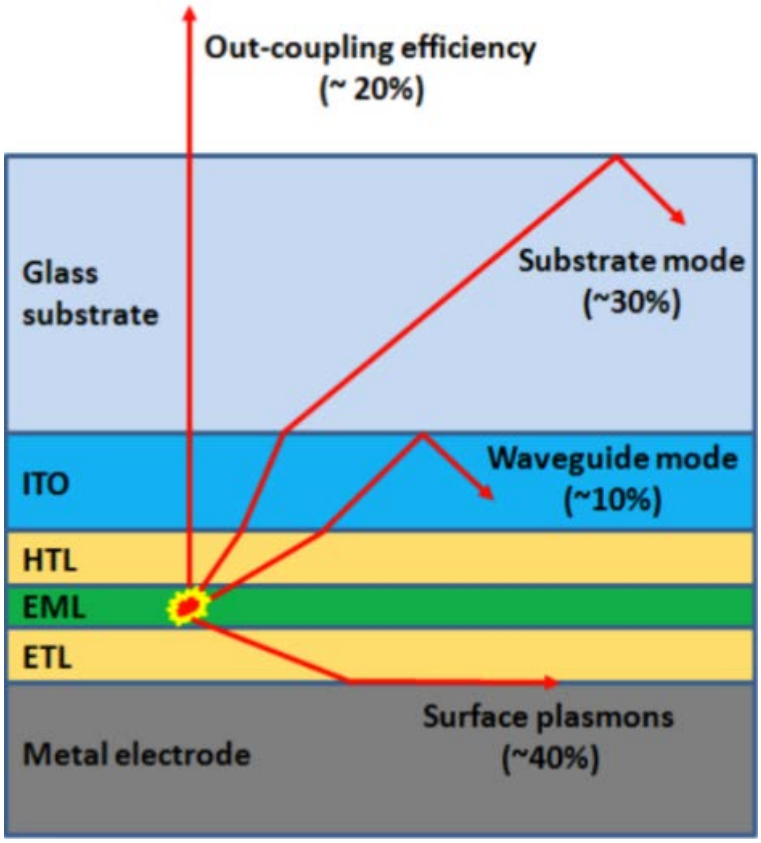

Figure 11. Scheme of light out-coupling losses in ordinary OLEDs.

The following performance parameter is the IQE of an OLED. The IQE is a ratio of the generated photons to injected hole-electron pairs in the OLED device. Therefore, the IQE is a parameter that does not consider the out-coupling losses from the EQE metric. Several techniques need to be combined to achieve an estimation of IQE. Figure 11 demonstrates a variety of optical pathways through which generated photons can take in the OLED device. Surface plasmon quenching, optical absorption, and internal reflections in the organic layers, the transparent conductive oxide (TCO including ITO), and the glass substrate are responsible for around 80% of the loss of emitted light. The optical losses of emitted light make it difficult to quantify the total number of photons which are electrically generated in the OLED device.

The first technique that can be combined to estimate the IQE is photoluminescent quantum yield (PLQY). Electroluminescence is a method to emit photons through electrically generated excitons. On the other hand, photoluminescence is the other method to emit photons via optically generated excitons. When high energy light (such as UV light) irradiates an organic photoluminescent molecule, the material absorbs the high energy light, leading to electrons being excited to the LUMO level and making excitons. Then, the excitons relax to the molecule's ground state, and the material emits photons, which is a similar process with electroluminescence. For measuring a PLQY of organic material, a sample is placed in the integrating sphere that is fitted to a monochromatic light source, a high-resolution detector, and a spectrometer.

During the PLQY measurement, the material is illuminated by the light source of a specific intensity, and the emitted light is collected in the detector and processed in the spectrometer. Then, the number of photons absorbed in the sample material can be quantified by the intensity of the excitation source, which will be compared with the final intensity of the source. The number of photons emitted from the sample material will also be measured. The ratio of absorbed photons to emitted photons indicates the PLQY of the sample material. This PLQY is correlated with the IQE; however, it cannot be assumed to be accurate because electroluminescence and photoluminescence have different mechanisms.

The following technique for estimating the IQE of OLED devices is optical modeling based on the dipole emission model. This can simulate the device structure that already has information of orientation, optical constants, thickness, and IQE with high accuracy. The dipole emission model will make a device, and the combination of the thickness, optical constants, and IQE will allow simulation of the quantity of light to reach the air. The optical model will not lead to any significant conclusions unless validated with real OLED devices. A series of devices can be made where the thickness of one or more layers is varied. For example, if an OLED device which has a well-known charge confining structure is employed, then the only losses in the device setting can be assumed to be optical losses. Also, the input IQE value of the model can be used to set the theoretical and experimental data by building an optical to match the devices with varying layer thickness. Currently, the combination of optical modeling and device test is the best way to achieve an accurate value of IQE.

One of the most important performance parameters is the operational lifetime of the OLED device. The stability of the device is essential for commercialization. Therefore, the operational lifetime needs to be measured in a standardized way for an accurate comparison with other device performances. For calculating this, the luminescent decay of the OLED device is measured by driving at a constant current density and detecting the brightness decay over time through a silicon photodiode. Then, a time to some percentage decay of the initial brightness can be obtained.

The percentage decay values of 50% (LT_{50}), 70% (LT_{70}), 80% (LT_{80}), 97% (LT_{97}) and the initial brightness of 1000 cd/m^2 are generally used for lifetime testing. For accelerated testing of the device, a higher starting brightness (10000-20000 cd/m^2) is usually driven to reduce the time needed to screen the device. The stretched exponential decay model shows an equation that makes the lifetime of the OLED device be estimated from a lower starting brightness.

Equation 1

$$LT(L1) = LT\ (L_0)*(L_0/L_1)^N$$

where $LT(L_0)$ is a lifetime of the device from an initial brightness of L_0, $LT(L_1)$ is a calculated lifetime of the device at brightness L_1, and N is the escalation factor. The value of N is dependent on the material and degradation mechanism of the device. However, it is widely estimated to be N=1.7.

The last parameter is the color rendering index (CRI) which is a quantitative measurement of the ability of a light source to reveal the colors of various objects in comparison with an ideal light source. This index is assigned to a number between 0 to 100, where 0 means no matching and 100 means a perfect matching to standardized

daylight (blackbody). For a desirable light source, a CRI value above 80 is required.

The most widely used characterizing the chromaticity of light is a coordinate plot developed by the Commission Internationale del'Eclairange (CIE) in 1931 as shown in Figure 12. The CIE coordinates only demonstrate in terms of x and y, which makes easy 2D plotting on the CIE plot. The CRI and CIE coordinates provide a standardized method to quantify the color of light.

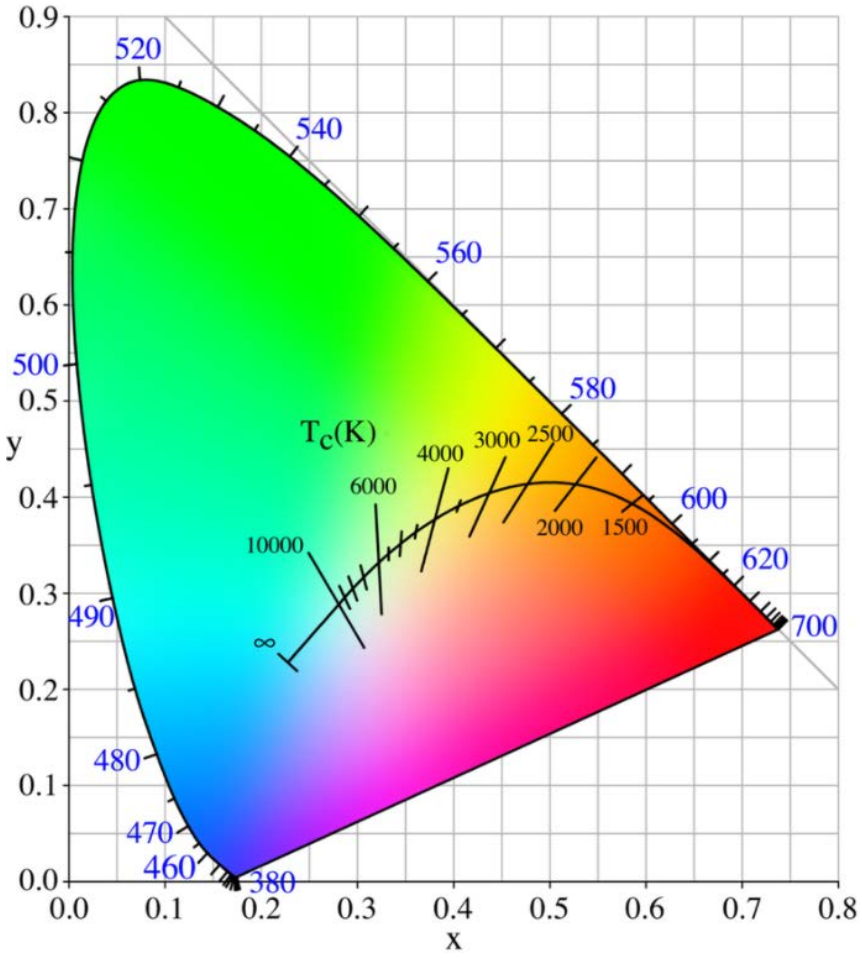

Figure 12. Commission Internationale de l'Eclairange 1931 XY chromaticity plot.

1.3 Organic neuromorphic device

The neuromorphic computing system was firstly described by Carver Mead [21]. It emulates the biological neural structures in the nervous system by employing electronic circuits based on both analog and digital components for future computing systems [22]. In order to understand the necessity of neuromorphic devices, the limitations of the conventional computing system will be firstly described.

1.3.1 Limitations of the conventional computing system

Nowadays, with the growth of big data technologies, Internet-of-Things (IoT), and artificial intelligence (AI), high-performing and energy-efficient computing systems are required. However, conventional computing systems encounter formidable obstacles, such as the end of Moore's Law and the von Neumann bottleneck.

Moore's Law was proposed by Dr. Gordon Moore in 1965 to predict the number of transistors in a dense integrated circuit double about every 18 months [23]. It has been a relatively accurate guide to the growth of the semiconductor industry for decades. As a result, semiconductor industries could prepare long-term planning and set the targets of research and development, and now billions of transistors are on a tiny chip and show powerful computing systems. But, Moore's Law no longer centered its research and development plan and will likely end soon because transistors eventually would reach the scaling limits of miniaturization at atomic levels [24], [25].

The other major limitation of the conventional computing system is the von Neumann bottleneck. John von Neumann proposed a computing architecture in 1945 which separates logic computations, data memory, and program as shown in Figure 13

[26]. However, this computing architecture has a fundamental drawback that the separation of processing unit and memory requires a constant data movement taking significant time and energy to perform. Especially with the growth of big data technologies in recent years, the speed of data movement is restricted, which eventually decreases computing performance. This is called the von Neumann bottleneck that has become a significant hurdle by consuming enormous power and time during operation [27]–[30].

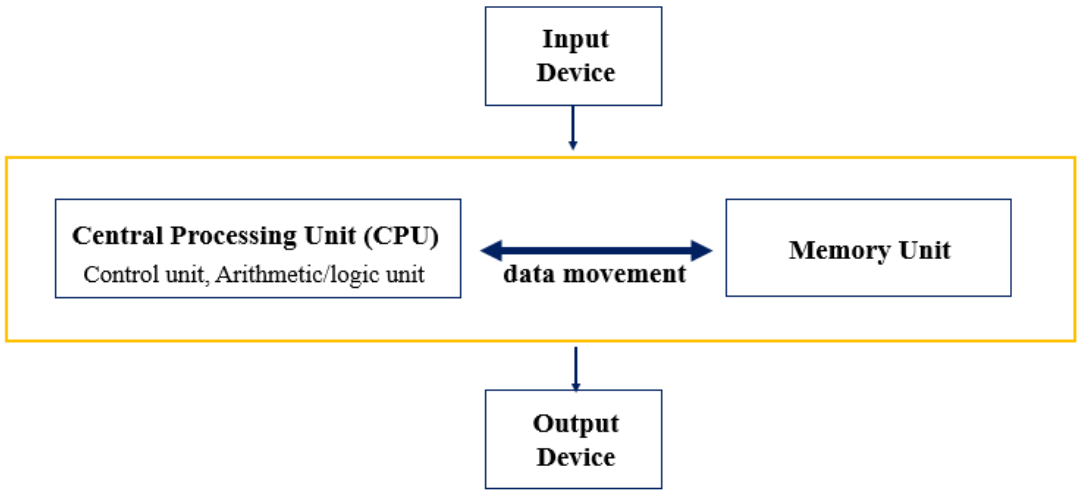

Figure 13. Scheme of the von Neumann Architecture.

To overcome these roadblocks, the semiconductor industries are required to explore solutions on the basis of a new computing system. And, inspired by the biological system, neuromorphic computing has been researched for decades as a promising candidate in the future.

1.3.2 Neuromorphic computing

An efficient computing framework is found in biological brain systems performing analog computations through massively parallel networks of neurons and synapses. The human brain, as an example, consumes only 20 watts from blood flow measurements to fulfilling all of its functions through analog computations, which store the synaptic weight and simultaneously regulate signal transmission [31]. Inspired by the brain systems, the idea of neuromorphic computing was introduced in 1990 by Carver Mead and has been researched for decades (Figure 14) [21], [32]. Mead pointed out that the key of the human brain's energy efficiency is analog computation, integration of logic and memory through neuron's parallel networks, and the learning ability. Therefore, many research groups have tried to find appropriate electronic devices that perform analog computing with simultaneously storing information and transmitting a signal to prevent the von Neumann bottleneck. By showing the information through the analog signals in computing hardware, the neuromorphic device can achieve orders of magnitude energy efficiency compared to conventional computing systems [33].

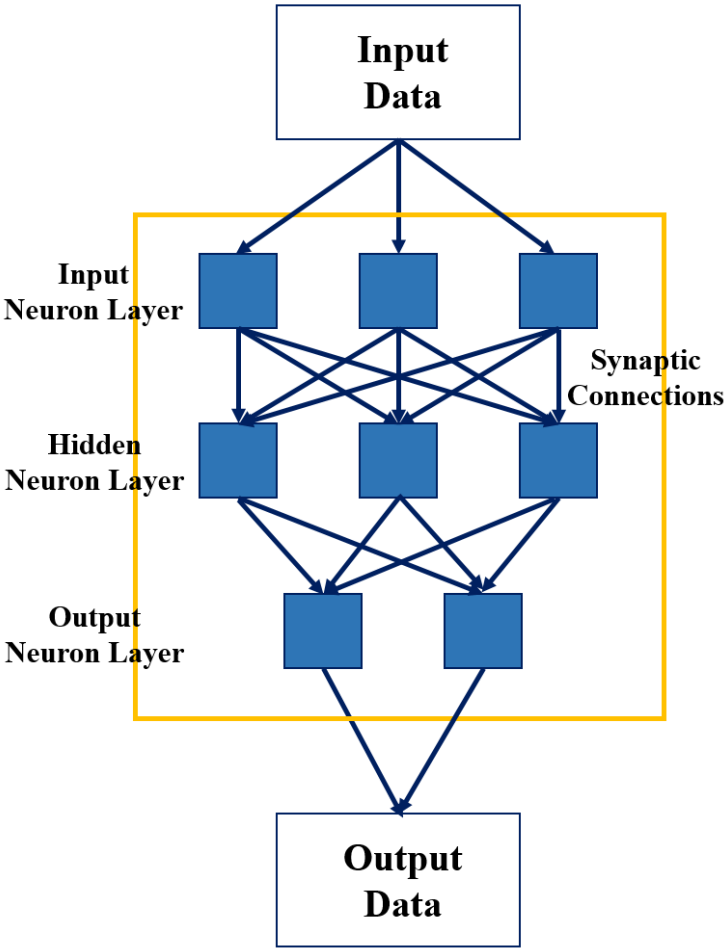

Figure 14. Scheme of the neuromorphic computing Architecture.

On the one hand, complementary metal-oxide-semiconductor (CMOS) based neuromorphic devices have been developed to emulate event-driven and large-scale spiking neural networks with highly efficient computing architectures [34], [35]. Such architectures have been applied in neuromorphic hardware designs like Neurogrid, BrainScaleS, TrueNorth, SpiNNaker, and Loihi [36]–[40]. Despite this remarkable progress, there are crucial challenges for CMOS-based neuromorphic devices in terms of scalability and power consumption as an ideal neuromorphic system [41], [42]. On the

other hand, a new class of emerging neuromorphic devices, namely, memristor or resistive random access memory (ReRAM), has been vigorously investigated.

1.3.3 Memristor

Memristors (or memristive devices) are two-terminal electric devices that encode information in their resistance states according to the history of applied stimulations through the physical mechanism of ion or oxygen vacancy drift [43]–[45]. This portmanteau (i.e., memristor) is the combination of memory and resistor, which indicates its operational principle [46], [47]. It is important to note that such a character makes the memristors an alternative to the current computer architectures based on simultaneously performing the roles of memory and processor.

The initial concept of memristor was introduced in 1971 by Dr. Leon Chua [43]. The original definition of the memristor was related to electric charge and magnetic flux linkage, as depicted in Figure 15. However, it has been vigorously investigated in the last few years owing to its similarity with the biological synapse mechanism with regard to computing and memorizing at the same time.

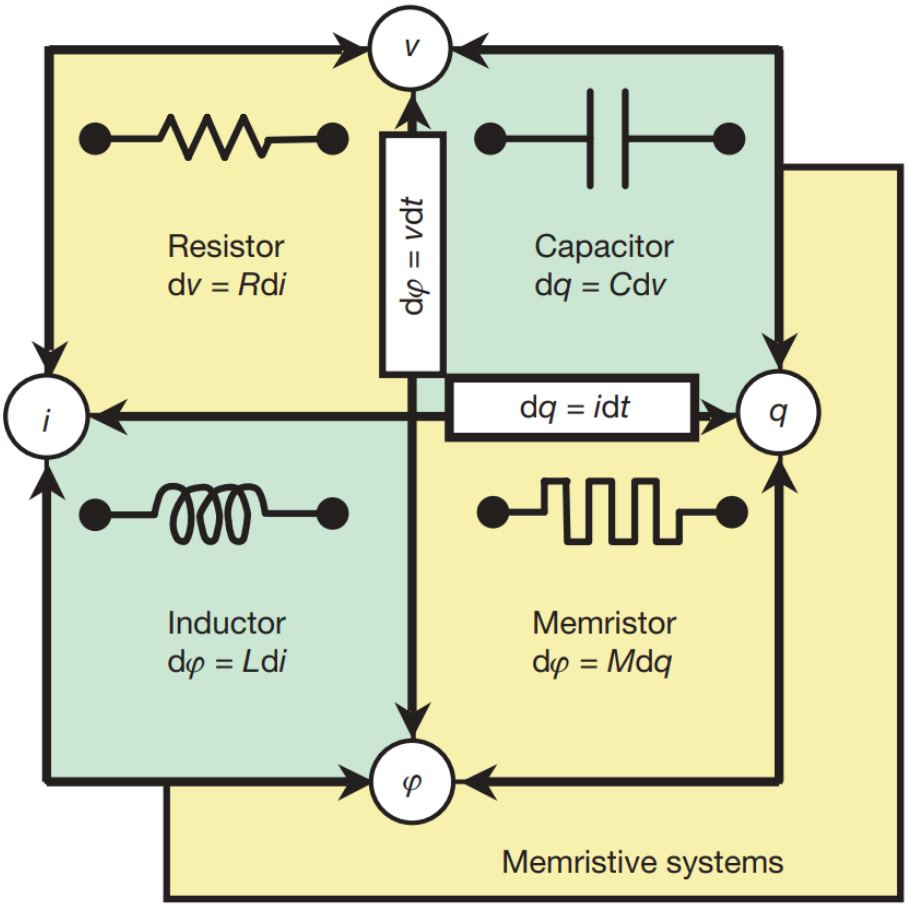

Figure 15. The four fundamental electrical elements: resistor, capacitor, inductor, and memristor [47].

2. DEVELOPMENT OF NEW EMITTER MATERIALS FOR DEEP BLUE OLED DEVICES

The development of efficient and stable OLEDs has been a challenging goal to pursue the next-generation display and solid-state lighting technologies [48]. Therefore, phosphorescent emitters which are able to harvest both electrogenerated single and triplet excitons due to the strong spin-orbit coupling (SOC) have primarily been developed and employed for highly efficient and stable OLED devices [49]–[53]. Through the phosphorescent emitters, 100% electron-to-photon conversion efficiencies can be achieved, and the operational lifetimes of state-of-the-art red and green OLED devices are long enough to satisfy the commercial requirements [53]–[56]. Despite this remarkable progress, the development of efficient and stable deep blue phosphorescent emitters remains a critical challenge [57], [58]. For further advancement of OLED technology, it is vital to surmount such a hurdle.

Recently, our group reported a series of tetradentate cyclometalated Pt(*ppz*-O-CbPy-R) complexes, namely, PtON1 analogs, with various substitution groups on the pyridyl ring, where *ppz* is 3,5-dimethyl-1-phenyl-pyrazole and CbPy is carbazolyl-pyridine [59]. In the paper, the PtON1 analogs that added electron-donating groups (such as -tBu, -Me, or -NMe_2) on the 4-position of the pyridyl ring exhibited significantly narrowed emission spectra with full-width at half-maximum (FWHM) values of 15-20 nm and deep-blue colors at room temperature as shown in Figure 16. However, PtON1 analogs have not demonstrated reasonable operational stability in the device settings owing to the potential instability of the phenyl-pyrazole moiety. On the other hand, a platinum metal with carbazolyl-pyridine-based tetradentate cyclometalated ligand, i.e.,

PtNON, exhibited better stability with high triplet energy of 2.83 eV [56]. A PtNON-based device with strong charge confinement demonstrated a peak external quantum efficiency (EQE) of 24.4% [56], while an optimized PtNON device exhibited an estimated operational lifetime to 70% of the initial luminance (LT_{70}) over 1300 h with an EQE of 17.4% at 1000 cd/m^2 [60]. Despite these progresses, the broad emission spectra of PtNON-based devices make unsatisfactory performance due to the poor quality of blue emission color. It is believed that the small energy gap between the lowest triplet state (T_1) and the second-lowest triplet state (T_2) of PtNON causes dual emission originated from T_1 and T_2, leading to the broad and sky blue emission spectrum of PtNON.

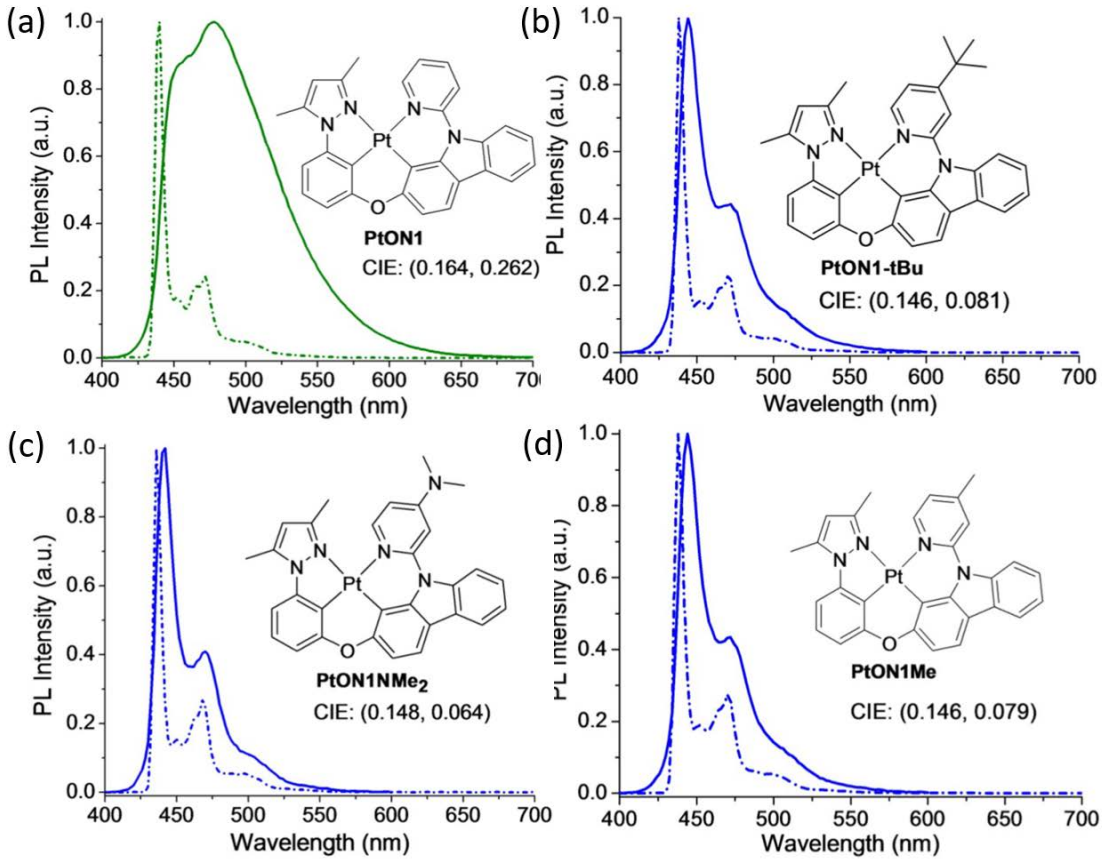

Figure 16. Luminescence spectra of (a) PtON1, (b) PtON1-tBu, (c) $PtON1NMe_2$, and (d)

PtON1Me at room temperature in CH_2Cl_2 (solid lines) and 77 K in 2-Me-THF (dash-dotted lines). The chemical structures and CIE coordinates at room temperature of each material are shown in the inset [59].

This chapter will report new platinum complexes, PtNONS56 and PtNONS56-dtb, designed to achieve narrower and blueshifted emission spectra through a color tuning strategy that increases the energy gap between T_1 and T_2 of PtNON. The electrochemical measurement exhibits that the structure modification from PtNON to PtNONS56 has a negligible effect on both oxidation and reduction potential of the complex while the structure modification from PtNONS56 to PtNONS56-dtb shifts the reduction potential to a more negative value without a change in the oxidation potential. Both new complexes are highly emissive in solution and PMMA films with reasonably short luminescent lifetimes. Also, they are thermally stable for sublimation. Notably, PtNONS56-dtb showed a significantly blueshifted and narrowed emission spectrum at 460 nm with a full-width at half-maximum (FWHM) of 59 nm compared to PtNON at 480 nm with a FWHM of 87 nm at room temperature in PMMA thin film. Additionally, PtNONS56-dtb in a device achieved a higher peak EQE of 8.5%, lower turn-on voltage of 2.5 V, and blueshifted emission peak at 470 nm with a narrowed FWHM of 60nm compared to PtNON, which showed peak EQE of 7.5%, turn-on voltage of 3 V, and emission peak at 494 nm with a FWHM of 86 nm in the same device setting.

2.1. Color tuning strategies for deep blue emitters

Deep blue emitters are an essential component of efficient blue OLED devices. They require high emission energy in the range of 2.7 eV to 2.8 eV. Despite its only 25% of exciton harvesting efficiency, many commercial displays still use fluorescent blue

emitters owing to their good operational stability [61]. Therefore, the design of efficient and stable deep blue phosphorescent metal complexes is necessary.

The progress of blue phosphorescent emitters has primarily been accomplished through designing Ir complexes for high efficiencies and deep blue colors [58], [62], [63]. A suitable starting material of color tuning is typically studied green phosphorescent emitter, *fac*-Ir(ppy)$_3$, which showed an estimated operational lifetime to 50% of the initial luminance (LT_{50}) of 160,000 h [64]. Using this prototypical phosphorescent complex, *fac*-Ir(ppy)$_3$, as a starting point, the green emission color can be sufficiently blueshifted through the modification of the phenyl-pyridine cyclometalated ligand as shown in the pathways of Scheme 1.

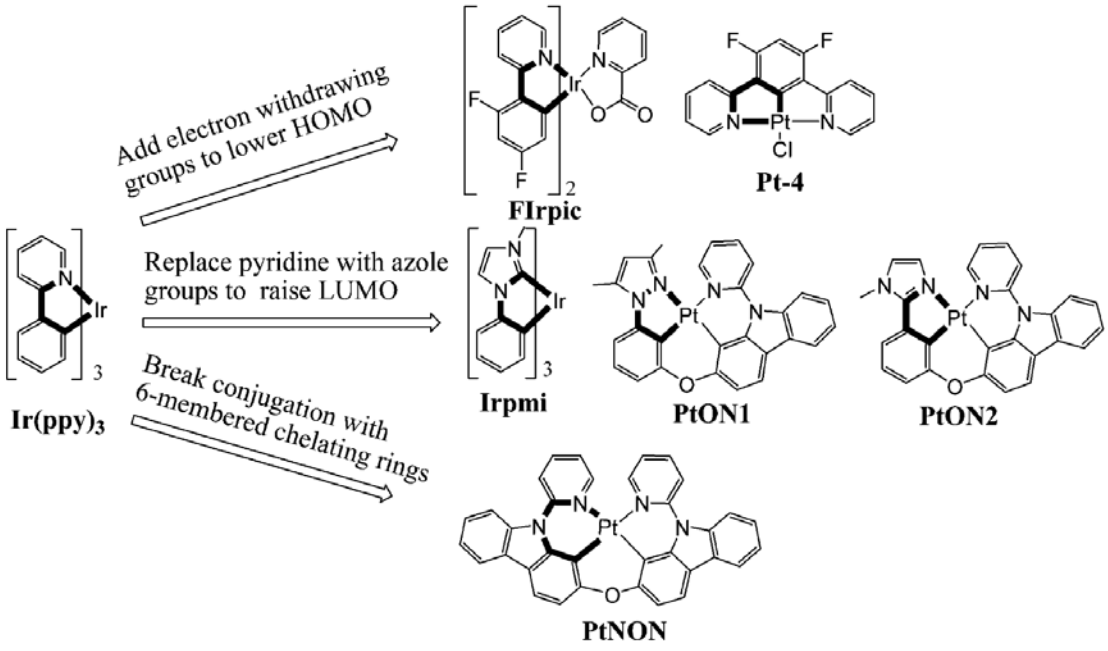

Figure 17. Color tuning strategies for blue emitters from Ir(ppy)$_3$ [56].

First, the emission energy is blueshifted by lowering the highest occupied molecular orbital (HOMO) energy by adding electron-withdrawing groups on the phenyl ring, which is the most widely used for the blue emitters such as FIrpic, FIr6, FPt, and Pt-4 [65], [66]. This strategy successfully shifted the emission spectrum to higher energy and achieved high efficiencies. However, the poor electrochemical stability of fluorine-containing emitters leads to rapid degradation of the molecules and consequently the low operational lifetime of the OLED devices.

Second, another pathway is raising the lowest unoccupied molecular orbital (LUMO) energy by replacing the pyridine ring with isoelectronic azolyl rings, such as pyrazole or imidazole [66]–[69]. Through this route, deep blue emission color and high efficiencies have been achieved with OLED devices. As mentioned above, PtON1, as an example, reached a peak EQE of 25.2% and CIE coordinates of (0.15, 0.13). Nevertheless, the operational lifetime of these emitter-based OLED devices is dramatically shorter than their phenyl-pyridine analogs. For either strategy, fluorinated or azole-based emitters, nearly all of the existing researches have demonstrated that their operational lifetimes are orders of magnitude lower than the green or red emitters employing phenyl-pyridine moieties.

An alternative method was recently introduced to achieve an efficient blue phosphorescent emitter by breaking the conjugation between the donor and acceptor portions and forming 6-membered metal chelation rings. From this strategy, PtNON was designed and achieved high efficiency with a long operational lifetime in a device, as mentioned above [56]. Despite its achievements, PtNON-based devices produce a broad emission spectrum that lies within the sky blue region of the visible spectrum. It is

believed that the small energy gap between T_1 and T_2 of PtNON leads to the T_2 emission and consequently the broad and sky blue emission spectrum in OLED devices. Therefore, PtNONS56 and PtNONS56-dtb were designed to achieve narrower and blueshifted emission spectra through a color tuning strategy that increases the band gap between T_1 and T_2 of PtNON.

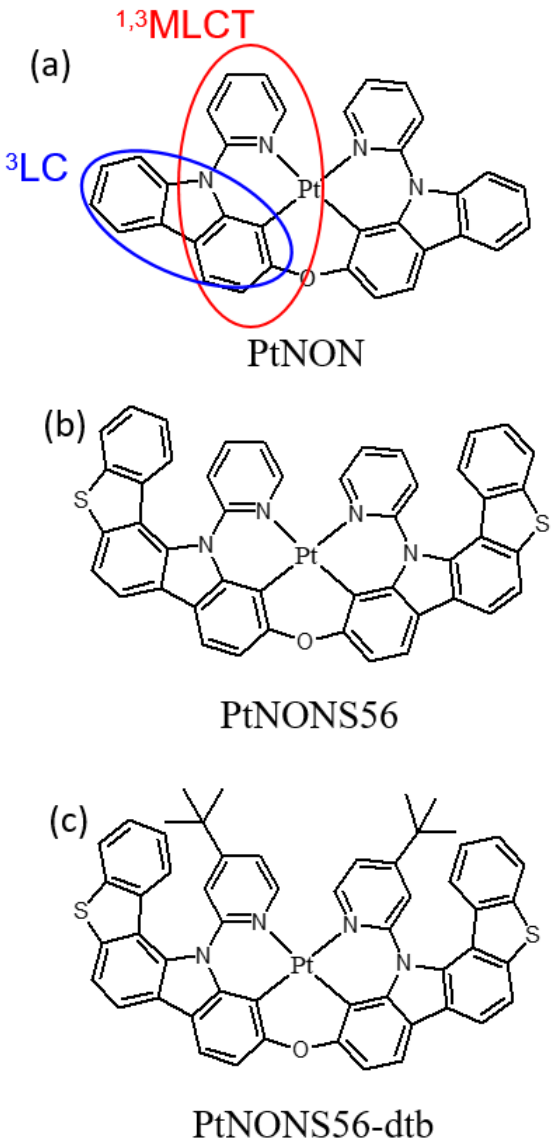

Figure 18. Structures of the (a) PtNON, (b) PtNONS56, and (c) PtNONS56-dtb.

2.2. Experimental section

Synthesis of Materials. The tetradentate Pt(II) complex, PtNON, has a symmetric structure Pt(CbPy-O-CbPy), where CbPy is carbazolyl-pyridine (Figure 18). Two CbPys are connected through an oxygen atom to form the N^C*C^N cyclometalating ligand. PtNONS56 is designed by extending the conjugation (i.e., addition of dihydrobenzothiophenes) on 5 and 6 positions of both phenyl rings in PtNON (Figure 18). And PtNONS56-dtb is formed through the incorporation of two *tert*-butyl groups (*t*-Bu) on the 4-positions (para positions) of both pyridyl moieties in PtNONS56 (Figure 18).

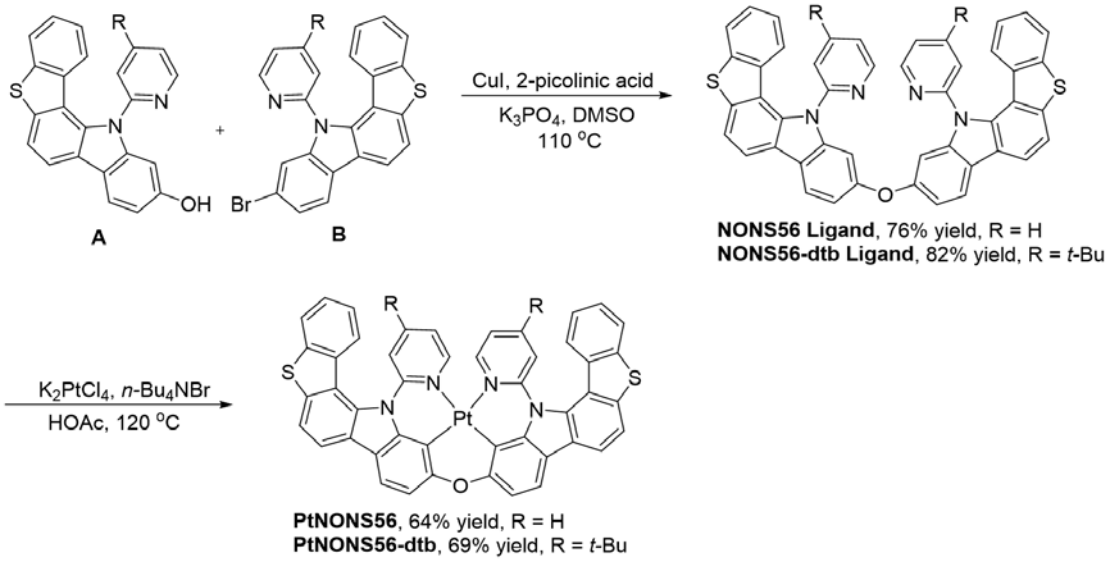

Figure 19. Synthesis of the ligands and complexes of PtNONS56 and PtNONS56-dtb.

PtNONS56 and PtNONS56-dtb were synthesized through the routes as described in Figure 19. The synthetic routes for intermediates A and B are depicted in Figure 20 and

Figure 21, respectively. NONS56 and NONS56-dtb ligands were synthesized through a direct C-O cross-coupling reaction of intermediates A and B catalyzed by copper(I) iodide. With these two ligands in hand, PtNONS56 and PtNONS56-dtb were then synthesized by metalation with potassium tetrachloroplatinate (K_2PtCl_4) in acetic acid. These two Pt(II) complexes were characterized by ^1H NMR spectroscopy (Figure 22 and Figure 23).

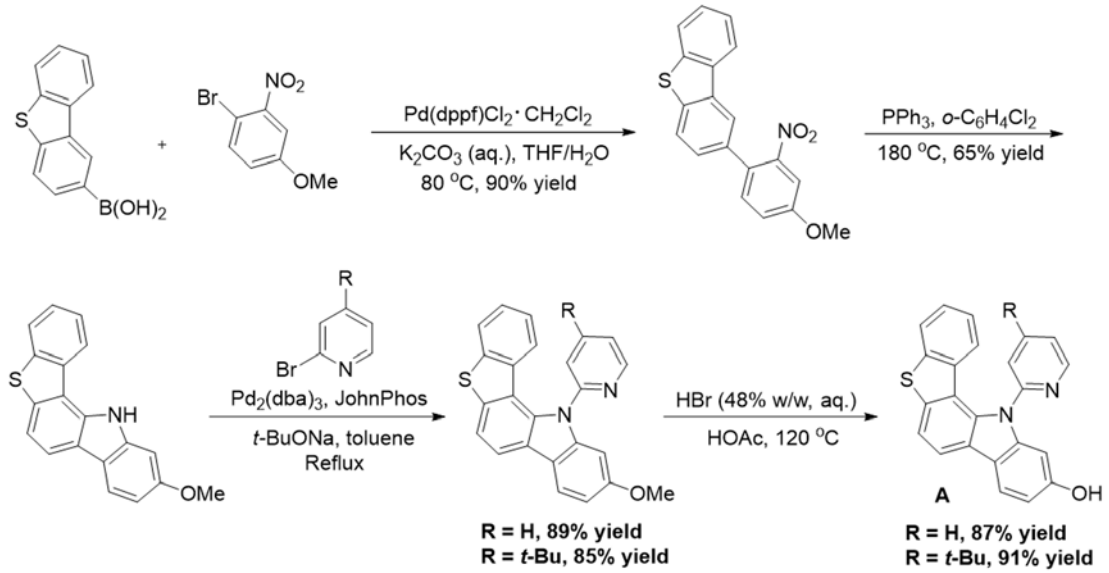

Figure 20. Synthetic route and conditions of compound A.

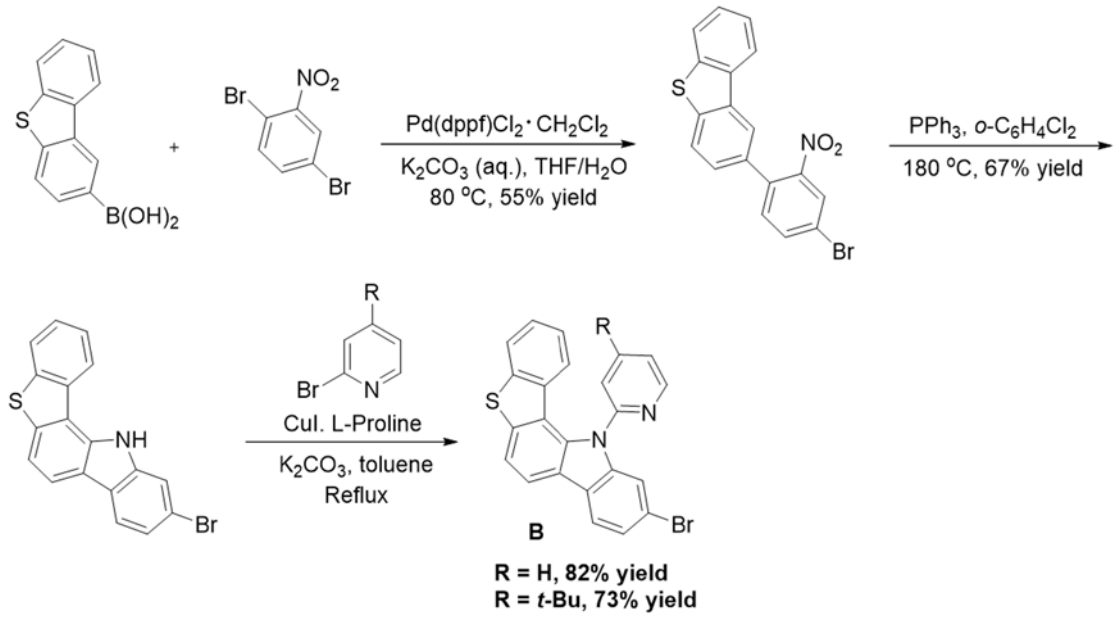

Figure 21. Synthetic route and conditions of compound B.

Platinum(II) 10,10'-oxybis(12-(pyridin-2-yl-κN)-12*H*-benzo[4,5]thieno[3,2-a]carbazol-11-yl-κC) (**PtNONS56**):

To a solution of NONS56 ligand (179 mg, 0.25 mmol) in HOAc (15 mL, 0.017 M) were added K_2PtCl_4 (125 mg, 0.3 mmol) and *n*-Bu_4NBr (8 mg, 0.025 mmol). The mixture was heated to reflux for 3 days. The reaction mixture was cooled down to room temperature and filtered through a short pad of silica gel. The filtrate was concentrated under reduced pressure. Purification by column chromatography (hexanes:DCM = 1:1 to 1:2) gave the PtNONS56 (145 mg, 0.16 mmol, yield: 64%) as a light yellow solid. ^{1}H NMR (400 MHz, DMSO-d_6, δ): 9.36 (d, *J* = 5.9 Hz, 2 H), 8.43 (d, *J* = 8.2 Hz, 2 H), 8.18 (t, *J* = 7.8 Hz, 4 H), 8.06 (d, *J* = 8.2 Hz, 2 H), 7.89 (t, *J* = 7.8 Hz, 2 H), 7.61-7.52 (m, 4 H), 7.42 (t, *J* = 7.7 Hz,

2 H), 7.30 (d, *J* = 8.3 Hz, 2 H), 7.21 (d, *J* = 8.3 Hz, 2 H), 7.11 (d, *J* = 8.3 H z, 2 H).

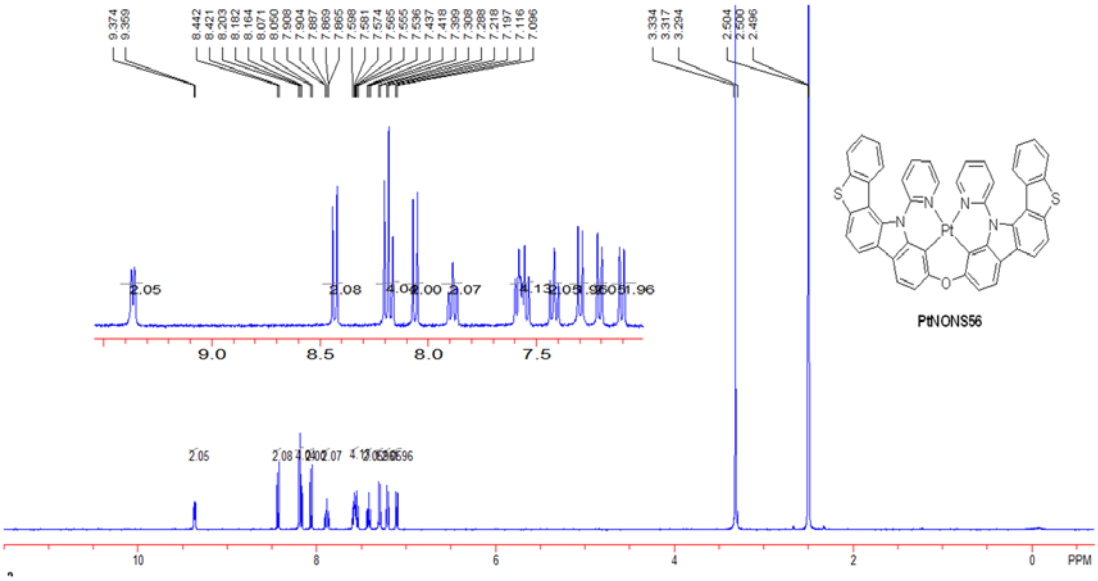

Figure 22. ^{1}H NMR spectrum of PtNONS56 at 400 MHz instrument in DMSO-d_6 solution.

Platinum(II) 10,10'-oxybis(12-(4-(tert-butyl)pyridin-2-yl-κN)-12*H*-benzo[4,5]thi eno[3,2-a]carbazol-11-yl-κC) (**PtNONS56-dtb**):

To a solution of NONS56-dtb ligand (156 mg, 0.189 mmol) in HOAc (11 mL, 0. 017 M) were added K_2PtCl_4 (94 mg, 0.227 mmol) and *n*-Bu_4NBr (6 mg, 0.019 m mol). The mixture was heated to reflux for 3 days. The reaction mixture was coo led down to room temperature and filtered through a short pad of silica gel. The filtrate was concentrated under reduced pressure. Purification by column chromatog raphy (hexanes:DCM = 1:1 to 1:2) gave the PtNONS56-dtb (133 mg, 0.13 mmol, yield: 69%) as a light yellow solid. ^{1}H NMR (400 MHz, DMSO-d_6, δ): 9.24 (d,

J = 6.3 Hz, 2 H), 8.45 (d, *J* = 8.2 Hz, 2 H), 8.19 (d, *J* = 7.9 Hz, 4 H), 8.07 (d, *J* = 8.2 Hz, 2 H), 7.65 (dd, *J* = 6.4, 2.0 Hz, 2 H), 7.57 (t, *J* = 7.5 Hz, 2 H), 7.40 (t, *J* = 7.5 Hz, 2 H), 7.30 (d, *J* = 8.3 Hz, 2 H), 7.16 (d, *J* = 8.3 Hz, 2 H), 6.91 (d, *J* = 1.6 Hz, 2 H), 0.76 (s, 18 H).

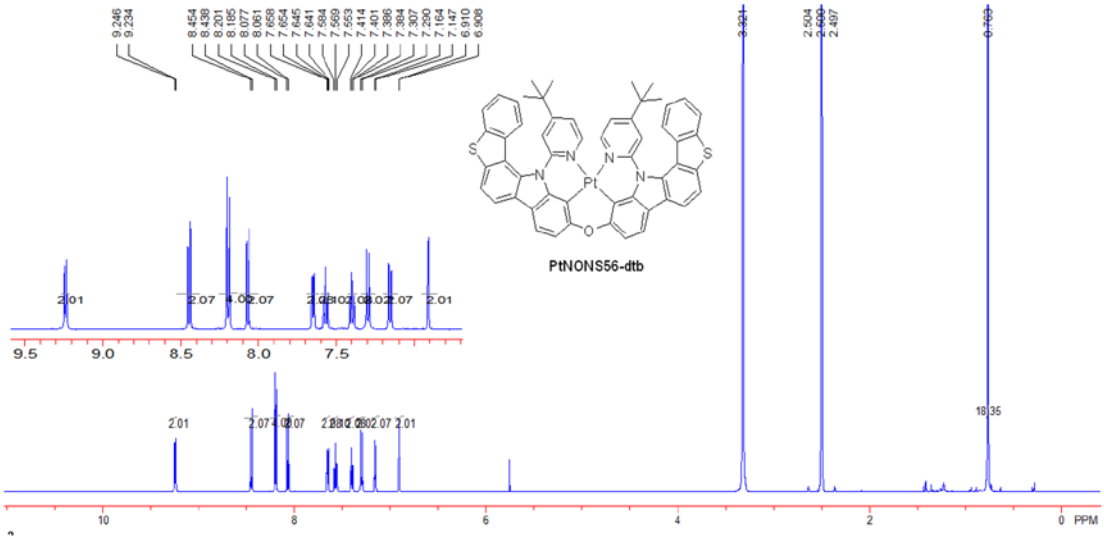

Figure 23. ^{1}H NMR spectrum of PtNONS56-dtb at 400 MHz instrument in DMSO-d_6 solution.

Theoretical Calculation. Titan software package was used for all chemical calculations. Molecular geometry of materials were optimized with density functional theory method.

Electrochemistry. A CH Instrument 610B electrochemical analyzer was used for the Cyclic voltammetry (CV) and different pulsed voltammetry (DPV) measurements. 0.1 M tetra(*n*-butyl) ammonium hexafluorophosphate was used as the supporting electrolyte and anhydrous dimethylformamide was used as the solvent under a nitrogen atmosphere. A platinum wire, silver wire, and carbon were used as the counter electrode, pseudo-

reference electrode, and working electrode, respectively.

Photophysical Measurements. The absorption spectra were recorded on an Agilent 8453 UV-Visible Spectrometer. The room temperature photoluminescence (PL) spectra were obtained on a Horiba Jobin Yvon FluoroLog-3 spectrometer in a dichloromethane solution. The cryogenic PL spectra were experiments were performed in 2-MeTHF at 77 K cooled with liquid nitrogen. PLQY was measured on a Hamamatsu absolute PL quantum yield spectrometer model C11347.

Device Fabrication and Characterization. Pre-patterned ITO coated glass substrates were cleaned by deionized water, acetone, and isopropyl alcohol. Organic materials were purified by sublimation with a four-zone thermal-gradient furnace under high vacuum. Organic layers were deposited in the custom-made vacuum thermal evaporation build by Travato Man. The based pressure was between 10^{-8} and 10^{-7} torr. The depositing rates of organic materials were between 0.2 and 1.0 Å s^{-1} monitored by quart crystal, and the aluminum cathode was deposited through a shadow mask without breaking vacuum, defining device area of 0.04 cm^2. The current-voltage-luminance and EQE were measured by a Keithley 2400 source meter with a Thorlabs FDS10X10 Si photodiode under a nitrogen atmosphere. EL spectra were measured by a Horiba Jobin Yvon FluoroLog-3 spectrometer.

2.3. Results and discussion

Theoretical Investigation. Density functional theory (DFT) calculations of PtNON and PtNONS56 were computed using the Titan software package (wave function, INC.) at the B3LYP/LACVP** level. Similar theoretical investigations have also been

used in the previously reported cyclometalated Ir(III) and Pt(II) complexes through minimizing singlet geometry for the approximation of ground and excited states [65], [70]–[73]. Both PtNON and PtNONS56 show considerable distortion on the carbazolyl-pyridine (CbPy) portion to accommodate square planar coordination to the metal (Figure 24 and Figure 25).

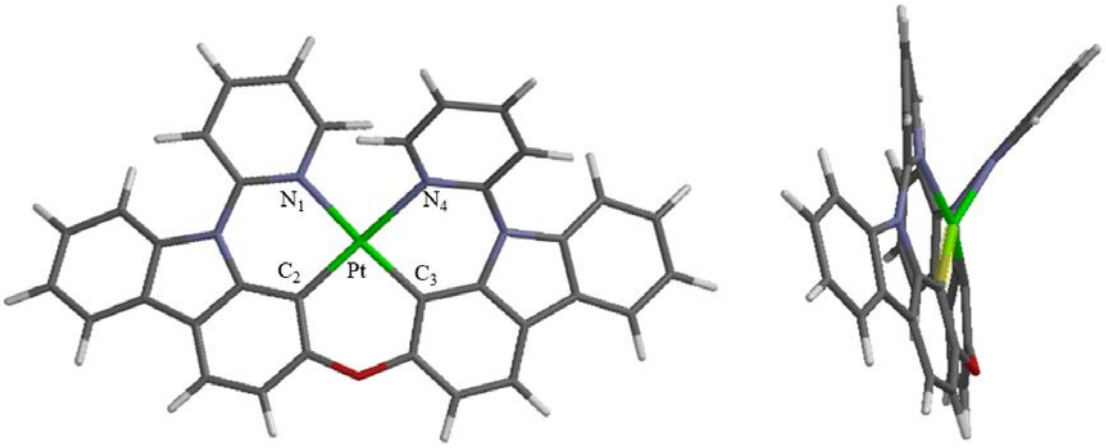

Figure 24. Optimized molecular structure of PtNON based on the DFT calculation, top view (left) and side-view (right).

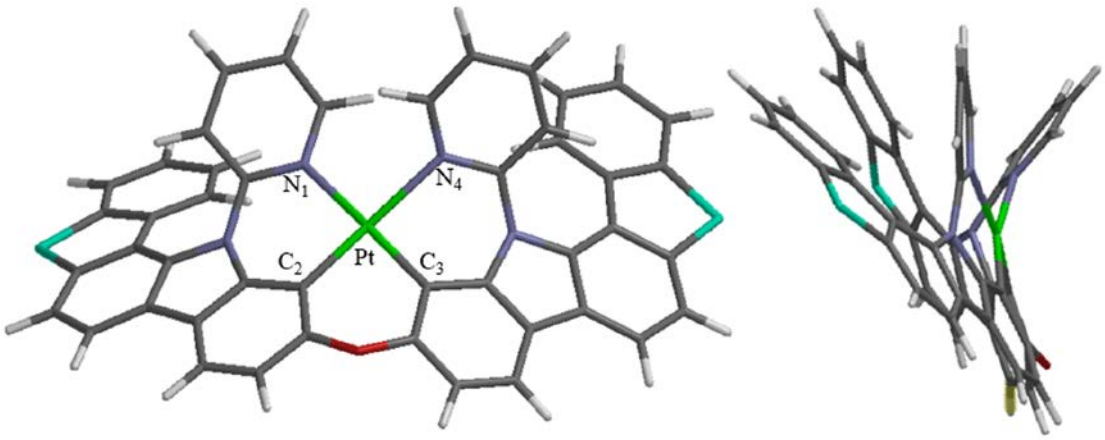

Figure 25. Optimized molecular structure of PtNONS56 based on the DFT calculation, top view (left) and side-view (right).

The structural modification from PtNON to PtNONS56 (i.e. extending the conjugation) significantly affects the geometric structure of the Pt(N^C^C^N) coordination. The bond lengths of Pt-C_2 (1.99 Å) and Pt-C_3 (1.99 Å) in PtNONS56 are identical to those in PtNON. On the other hand, bond lengths of Pt-N_1 (2.24 Å) and Pt-N_4 (2.24 Å) in PtNONS56 are relatively longer than those of Pt-N_1 (2.21 Å) and Pt-N_4 (2.22 Å) in PtNON. These bond lengths within the metal coordination are comparable to PtON1, PtON6, and PtON7 (Figure 26), which have a similar platinum core structure (Table 1) [57], [59]. The bond angles of PtNONS56 in the metal coordination are mostly similar to PtNON except the bond angles of N_4-Pt-N_1 (97.03°) and N_1-Pt-C_3 (171.79°) in PtNONS56 which are larger than those in PtNON (93.84° and 167.81°, respectively) (Table 2).

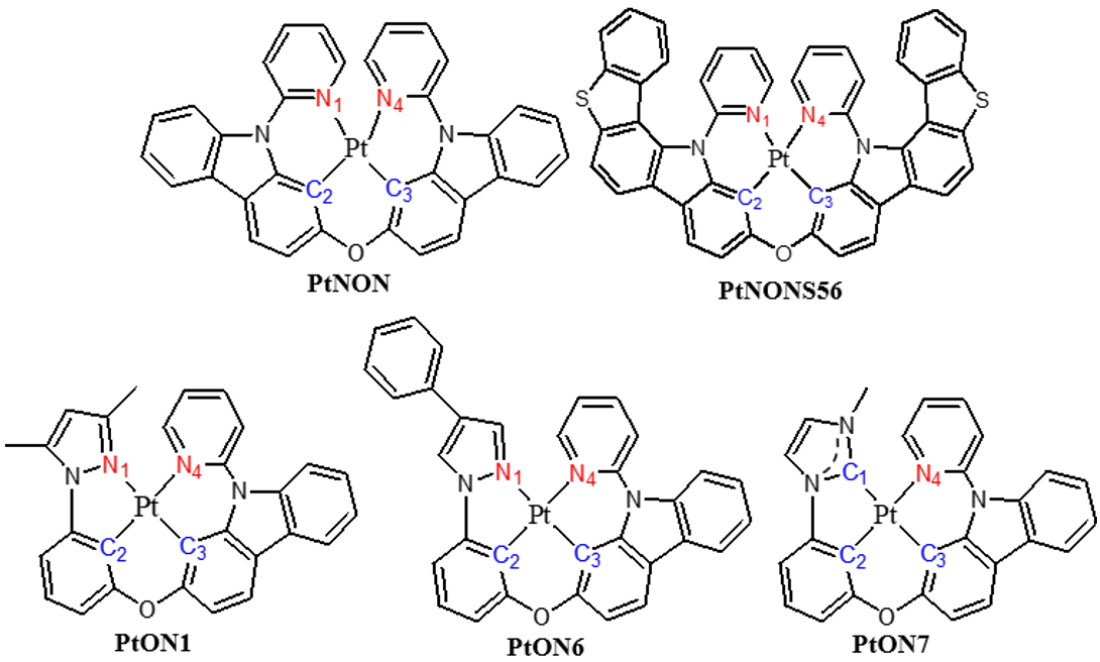

Figure 26. Chemical structures of PtNON, PtNONS56, PtON1, PtON6, and PtON7.

Table 1. Selected bond lengths for PtNON, PtNONS56 based on the DFT calculation.

Pt complexes	Pt-N_1(C_1) (Å)	Pt-C_2 (Å)	Pt-C_3 (Å)	Pt-N_4 (Å)
PtNON	2.21	1.99	1.99	2.22
PtNONS56	2.24	1.99	1.99	2.24
PtON1	2.18	1.98	1.98	2.19
PtON6	2.18	1.98	1.98	2.17
PtON7	2.08	1.99	2.02	2.19

Table 2. Selected bond angles for PtNON, PtNONS56 based on the DFT calculation.

Pt complexes	N_1-Pt-C_2 (°)	C_2-Pt-C_3 (°)	C_3-Pt-N_4 (°)	N_4-Pt-N_1 (°)	N_1-Pt-C_3 (°)	C_2-Pt-N_4 (°)
PtNON	91.03	91.62	86.50	93.84	167.81	165.48
PtNONS56	90.35	90.18	84.35	97.03	171.79	165.18

Electrochemical properties. Cyclic voltammetry (CV) and differential pulsed voltammetry (DPV) were used to examine the electrochemical properties of PtNON, PtNONS56, and PtNONS56-dtb. The oxidation and reduction potentials reported here were measured relative to an internal ferrocenium/ferrocene (Fc^+/Fc) reference in anhydrous dimethylformamide (DMF) solution under nitrogen atmosphere. The redox potentials are summarized in Table 3. All three complexes showed irreversible oxidation at around 0.42 V. The potential reactivity of the solvent with the square planar Pt(III) metal centers can contribute to the irreversible oxidation process of Pt(II) complexes [74], [75]. PtNON and PtNONS56 exhibited quasi-reversible reduction at -2.48 V and -2.44 V, respectively, while PtNONS56-dtb demonstrated a well-defined reversible reduction process at -2.6 V (Figure 27). It is found that the structural modification from PtNON to PtNONS56 (i.e., addition of dihydrobenzothiophenes on carbazoles) had a

negligible effect on both the oxidation and reduction potential of the complex. On the other hand, the reduction potential was dramatically influenced by introducing two *t*-butyl groups on the 4-position of the pyridyl rings (i.e., from PtNONS56 to PtNONS56-dtb) without a change in the oxidation potential. The reduction potential of PtNONS56-dtb was found to be 160 mV more negative than PtNONS56. A similar trend has been observed in previously reported PtON1 analogs that the addition of electron-donating groups (such as -tBu, -Me, or -NMe_2) on the 4-position of the pyridyl ring significantly shifted the reduction potential to 110-370 mV more negative with negligible changes in the oxidation potential [59]. The calculated HOMO levels of all three complexes are 5.2 eV and the LUMO levels of PtNON, PtNONS56, and PtNONS56-dtb are 1.9 eV, 1.9 eV, and 1.77 eV respectively [76], [77].

Table 3. Photophysical and electrochemical properties.
The room temperature (RT) absorption and emission spectra were measured in a solution of dichloromethane or in doped poly(methyl methacrylate) (PMMA) thin film and low temperature (77K) emission spectra were measured in a solution of 2-methyl-THF.

complex	absorption at RT	emission at RT in solution			emission at RT in doped PMMA film					emission at 77K			
	λ_{max} (nm) {ε, $10^3 cm^{-1}M^{-1}$}	λ_{max} (nm) {FWHM, nm}	τ (μs)	Φ (±10 %)	λ_{max} (nm) {FWHM, nm}	τ (μs)	Φ (±10 %)	k_r (10^4 s^{-1})	k_{nr} (10^4 s^{-1})	λ_{max} (nm)	τ (μs)	E_{ox} (V)	E_{red} (V)
PtNON	263{56.2}, 278{53.1}, 318{39.0}, 339{45.0}, 371{14.0}, 436{0.37}	508 {94}	2.6	31	480 {87}	3.8	83	21.8	4.5	438	11.7	0.41	-2.48
PtNONS56	258{88.6}, 280{64.5}, 307{41.1}, 346{42.2}, 371{30.5}, 448{0.38}	520 {96}	1.9	48	489 {87}	4.3	81	18.8	4.4	452	21.3	0.42	-2.44
PtNONS56-dtb	258{88.0}, 280{62.3}, 307{43.0}, 345{44.5}, 361{31.6}, 449{0.09}	490 {86}	6.7	86	460 {59}	15.2	90	5.9	0.7	452	32.3	0.42	-2.60

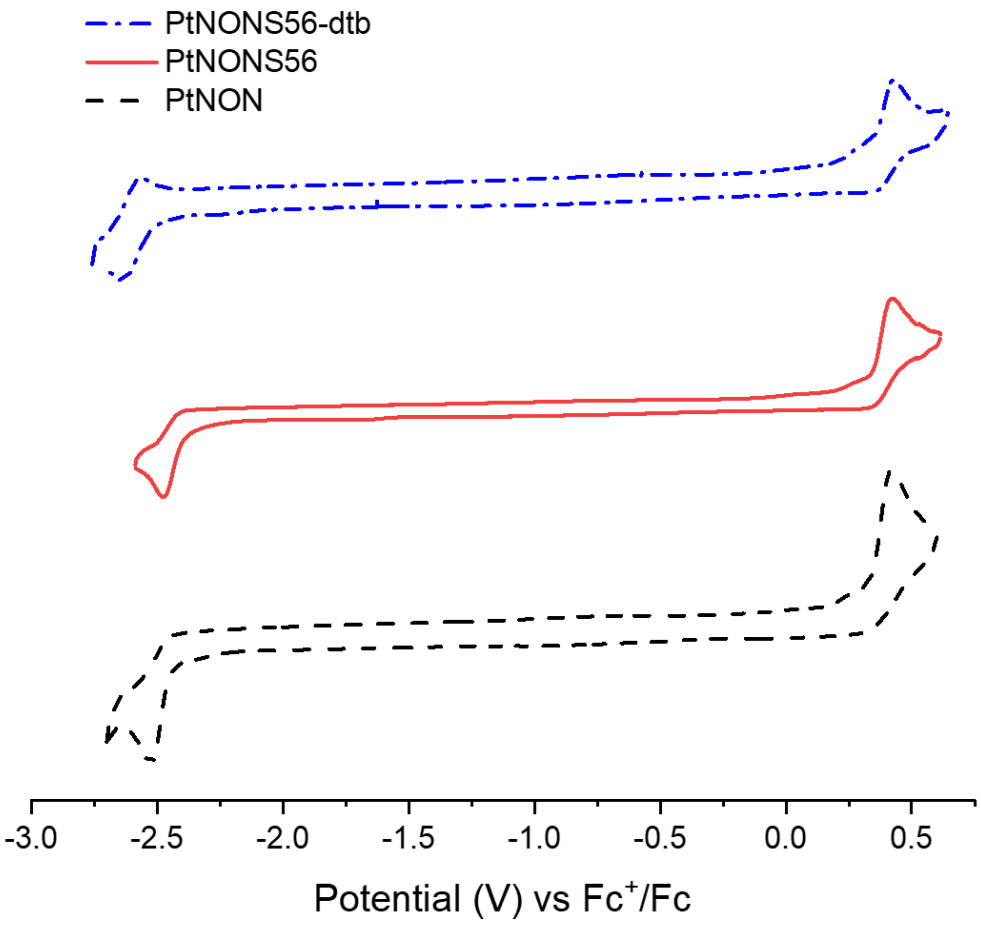

Figure 27. Cyclic voltammograms for PtNON (black dashed line), PtNONS56 (red solid line), and PtNONS56-dtb (blue dash-dotted line).

Photophysical Properties. The absorption and emission spectra of PtNON, PtNONS56, and PtNONS56-dtb were measured, and the data are summarized in Table 3. The absorption spectra at room temperature are shown in Figure 28. For these complexes, the strong absorption bands between 250 and 280 nm ($\varepsilon > 5 \times 10^4$ cm^{-1} M^{-1}) can be assigned to $^1(\pi\text{-}\pi^*)$ transitions on the ligands (LC) [78], [79]. The extinction coefficients of these bands at 258 nm for PtNONS56 ($\varepsilon = 8.86 \times 10^4$ cm^{-1} M^{-1}) and PtNONS56-dtb ($\varepsilon = 8.8 \times 10^4$ cm^{-1} M^{-1}) were greater than that of PtNON at 263 nm ($\varepsilon = 5.62 \times 10^4$ cm^{-1}

M^{-1}) due to the greater amount of phenyl rings in both PtNONS56 and PtNONS56-dtb compared to PtNON. The weaker absorption bands between 350 and 425 nm (ε = 1000 - 4500 $cm^{-1}\,M^{-1}$) can be identified as metal-to-ligand charge-transfer (MLCT) transitions that involve both the ligands and the platinum metal ions [80]. The lowest energy absorption bands between 425 and 500 nm (ε < 400 $cm^{-1}\,M^{-1}$) can be explained by transitions to the lowest triplet state based on the energy shift between absorption and emission [81]. The extinction coefficient of these bands at 449 nm for PtNONS56-dtb (ε = 90 $cm^{-1}\,M^{-1}$) had smaller value than those of PtNON at 436 nm (ε = 370 $cm^{-1}\,M^{-1}$) and PtNONS56 at 448 nm (ε = 380 $cm^{-1}\,M^{-1}$) (Table 3).

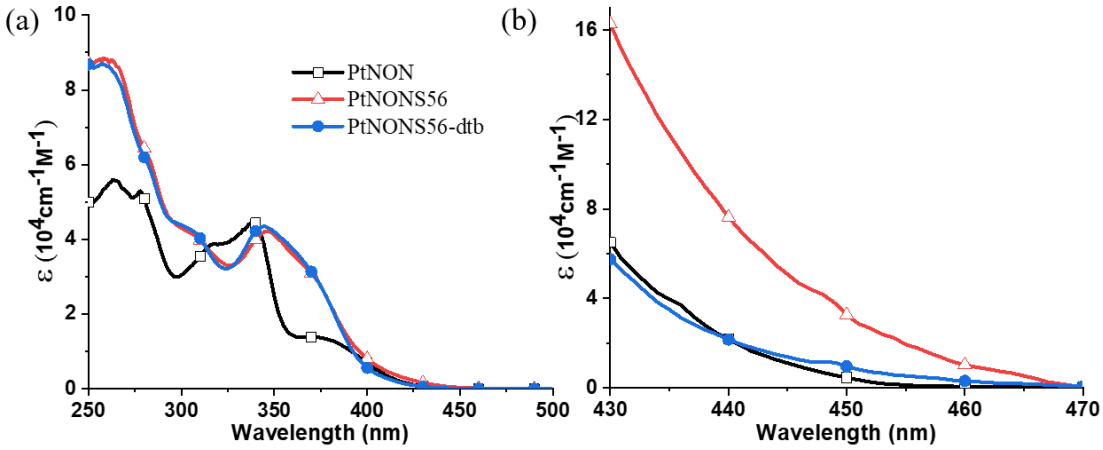

Figure 28. (a) Comparison of room temperature absorption spectra of PtNON (black squares), PtNONS56 (red triangles), and PtNONS56-dtb (blue solid circles) in CH_2Cl_2. The triplet absorption spectra are presented in (b).

The emission spectra of PtNON, PtNONS56, and PtNONS56-dtb at 77 K and room temperature are depicted in Figure 29. The structural modifications of the Pt complexes reveal substantial differences in their emission spectra and luminescent

lifetimes. Both PtNONS56 and PtNONS56-dtb had the redshifted emission peak (λ_{max}) at 452 nm, indicating lower T_1 emission energy (E_{T1}) of 2.74 eV, compared to those of PtNON (λ_{max} = 438 nm and E_{T1} = 2.83 eV) at 77 K. And the three Pt complexes exhibited the luminescent lifetime (τ) values of 11.7 μs for PtNON, 12.3 μs for PtNONS56, and 32.3 μs for PtNONS56-dtb at 77 K. On the other hand, at room temperature in dichloromethane solution, the emission spectrum of PtNONS56-dtb demonstrated a considerably blueshifted emission peak at 490 nm with a narrowed FWHM of 86 nm, while PtNON and PtNONS56 had an emission peak at 508 nm with a FWHM of 94 nm and 520 nm with a FWHM of 96 nm, respectively. Furthermore, the luminescent lifetime of PtNONS56-dtb was 6.7 μs, which is longer than PtNON with a τ of 2.6 μs and PtNONS56 with a τ of 1.9 μs at room temperature in solution. At room temperature in PMMA thin film, PtNONS56-dtb also showed a blueshifted emission peak at 460 nm with a significantly narrowed FWHM of 59 nm compared with those of PtNON (λ_{max} = 480 nm, FWHM = 87 nm) and PtNONS56 (λ_{max} = 489 nm, FWHM = 87 nm). Moreover, at room temperature in the thin film, PtNONS56-dtb indicated an increased luminescent lifetime of 15.2 μs compared to PtNON (3.8 μs) and PtNONS56 (4.3 μs).

All three complexes were intensely emissive at room temperature both in solution (Φ = 31 ± 10% for PtNON, 48 ± 10% for PtNONS56, and 86 ± 10% for PtNONS56-dtb) and in PMMA film (Φ = 83 ± 10% for PtNON, 81 ± 10% for PtNONS56, and 90 ± 10% for PtNONS56-dtb). The radiative decay rate (k_r) and nonradiative decay rate (k_{nr}) were calculated by the equations;

Equation 2

$$k_r = \Phi/\tau \text{ and } k_{nr} = (1 - \Phi)/\tau \quad (35)$$

The k_r values of PtNON, PtNONS56, and PtNONS56-dtb were in the range of 5.9×10^4 s^{-1} to 21.8×10^4 s^{-1}, and k_{nr} values of the complexes had a relatively narrower range of 7×10^3 s^{-1} to 4.5×10^4 s^{-1} at room temperature in PMMA film. PtNON and PtNONS56 had similar k_r and k_{nr}, whereas PtNONS56-dtb had a lower k_r value of 5.9×10^4 s^{-1}, indicating that k_r was strongly affected by structural modification on the pyridyl ring. A similar phenomenon was found in PtON1 analogs that k_r value was decreased by incorporating the electron-donating groups on the 4-position of the pyridyl ring [59]. Additionally, the close to unity emission efficiency of PtNONS56-dtb can be attributed to its small k_{nr} value of 7×10^3 s^{-1} (Table 3) [82].

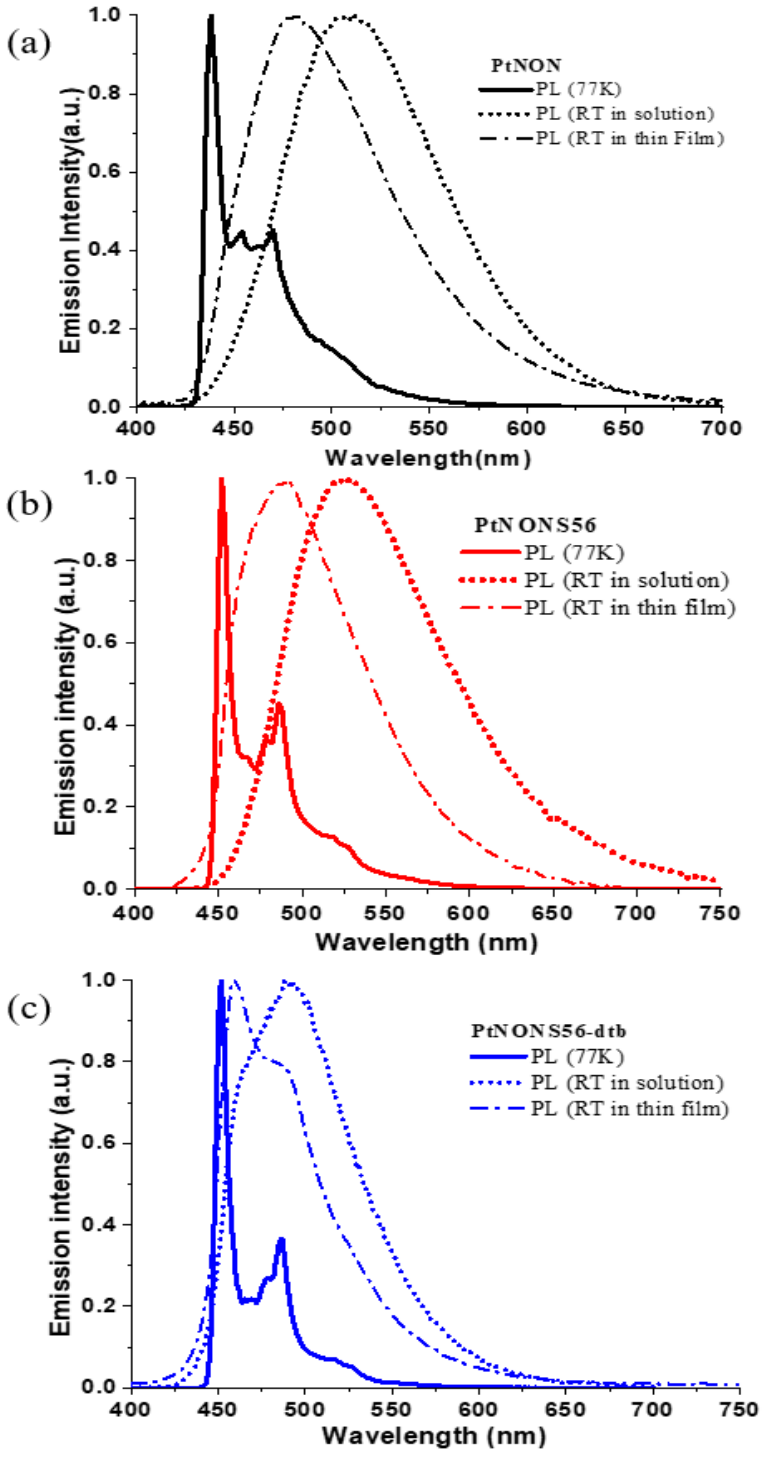

Figure 29. Plots of emission spectra of (a) PtNON, (b) PtNONS56, (c) PtNONS56-dtb in 2-Me-THF (solid lines) at 77 K, in CH_2Cl_2 (dotted lines) and in PMMA thin film (dash-dotted lines) at room temperature.

Ground-state and Excited-state Properties. PtNON, PtNONS56, and PtNONS56-dtb have dominant emission peaks with vibronic emission sidebands at 77 K, as shown in Figure 29, which indicated that the lowest triplet excited state (T_1) emission arises from the majority of ligand-centered charge-transfer (^{3}LC) mixed with small metal-to-ligand charge-transfer (^{1}MLCT/^{3}MLCT) character due to the strong spin-orbit coupling [17], [83], [84]. At 77 K, the dominant emission peak (λ_{max}) of PtNONS56 is redshifted by adding dihydrobenzothiophenes on carbazoles which is the ^{3}LC portion of PtNON as presented in Figure 18. Therefore, the structure modification from PtNON to PtNONS56 reduces the energy level of the ^{3}LC state, and consequently, the T_1 is lowered. On the other hand, PtNONS56-dtb has the same energy level of T_1 as PtNONS56 despite incorporating the electron-donating group (-tBu) on the 4-position of pyridyl ring where ^{1}MLCT/^{3}MLCT states are located (Figure S1). This indicates the structure modification from PtNONS56 to PtNONS56-dtb has a negligible effect on the T_1.

At room temperature, the second-lowest triplet energy state (T_2), which is assumed to be the same energy level as the ^{3}MLCT state for these Pt complexes, is thermally accessible. Consequently, the emission spectra of PtNON, PtNONS56, and PtNONS56-dtb significantly vary at room temperature (Figure 29). The emission spectrum of PtNON at room temperature is believed to originate from both T_1 and T_2 owing to their small energy gap, as depicted in Figure 30a. Therefore, PtNON exhibits broad and structureless emission spectra at room temperature in both solution and thin film, which can be attributed to the broad shape of T_2 emission spectrum. In PtNONS56, the addition of dihydrobenzothiophenes on carbazoles of PtNON lowers the energy level of T_1, which can lead to a larger energy gap between T_1 and T_2. However, it is assumed

that the emission spectrum of PtNONS56 is also originated from both T_1 and T_2 at room temperature due to their still small energy gap (Figure 30b). This can be assisted by the fact that PtNONS56 has broad and Gaussian-shaped emission spectra at room temperature in both dichloromethane solution and PMMA thin film. On the other hand, PtNONS56-dtb demonstrates significantly narrowed and blueshifted emission spectra at room temperature in both solution and thin film, which can be ascribed to the raised energy level of T_2. The introduction of the electron-donating group (-tBu) on the 4-position of the pyridyl ring shifts the reduction potential more negative and raises the ^{1}MLCT/^{3}MLCT states since the electron-donating group can make pyridyl ring less electron poor region [59].

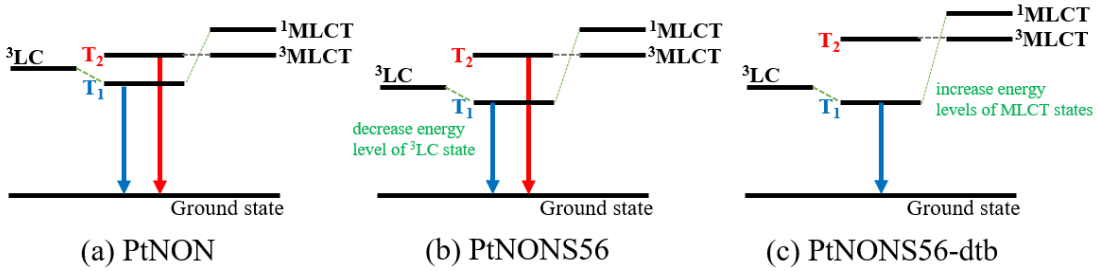

Figure 30. (a−c) Schematic energy level diagram related to T_1 and T_2 with the origin of emission in PtNON, PtNONS56, and PtNONS56-dtb at room temperature.

Thus, the PtNONS56-dtb emission is believed to originate from T_1 owing to the sufficiently raised energy level of T_2 through the structure modification (Figure 30c). This analysis can be further supported by the results that PtNONS56-dtb has a vibronic structure of emission spectrum, a longer luminescent lifetime, and a lower k_r value compared to PtNON or PtNONS56 at room temperature. It is worth noting that the tetradentate Pt(II) complex's emission energy is easily tuned through a simple structural

modification, which is important to design a pure blue phosphorescent emitter.

Device performance. To evaluate the utility of PtNONS56-dtb as an emitter in a device setting, devices were fabricated and tested using a known stable structure, ITO /HATCN (10 nm) /NPD (40 nm) /TrisPCz (10 nm) /5% emitter:mCBT (10 nm) /BALq (10 nm) /BPyTP (40 nm) /Liq (2 nm) /Al where HATCN is 1,4,5,8,9,11-hexaazatriphenylene-hexacarbonitrile, NPD is N,N′-diphenyl-N,N′-bis(1-naphthyl)-1,1′-biphenyl-4,4″-diamine, TrisPCz is 9,9′,9″-triphenyl-9H,9′H,9″H-3,3′:6′3″-tercarbazole, mCBT is 2,8-di(9Hcarbazol-9-yl)dibenzo[b,d]-thiophene, BAlq is bis(2-methyl-8-quinolinolato) (biphenyl-4-olato)aluminum, and BPyTP is 2,7-di(2,2′-bipyridin-5-yl)triphenylene [56], [60], [85]–[88]. The corresponding emitters are PtNONS56-dtb for device 1 and PtNON for device 2. mCBT and BALq were used as a host and a hole blocking material, respectively, for the narrowed electroluminescent spectra and stability of the device.

External quantum efficiency (EQE) versus luminance plots, power efficiency versus luminance plots, electroluminescent (EL) spectra, current density-voltage (J-V) characteristics, CIE coordinates, and normalized intensity versus device operational time of devices are presented in Figure 31, and the device performances are summarized in Table 4.

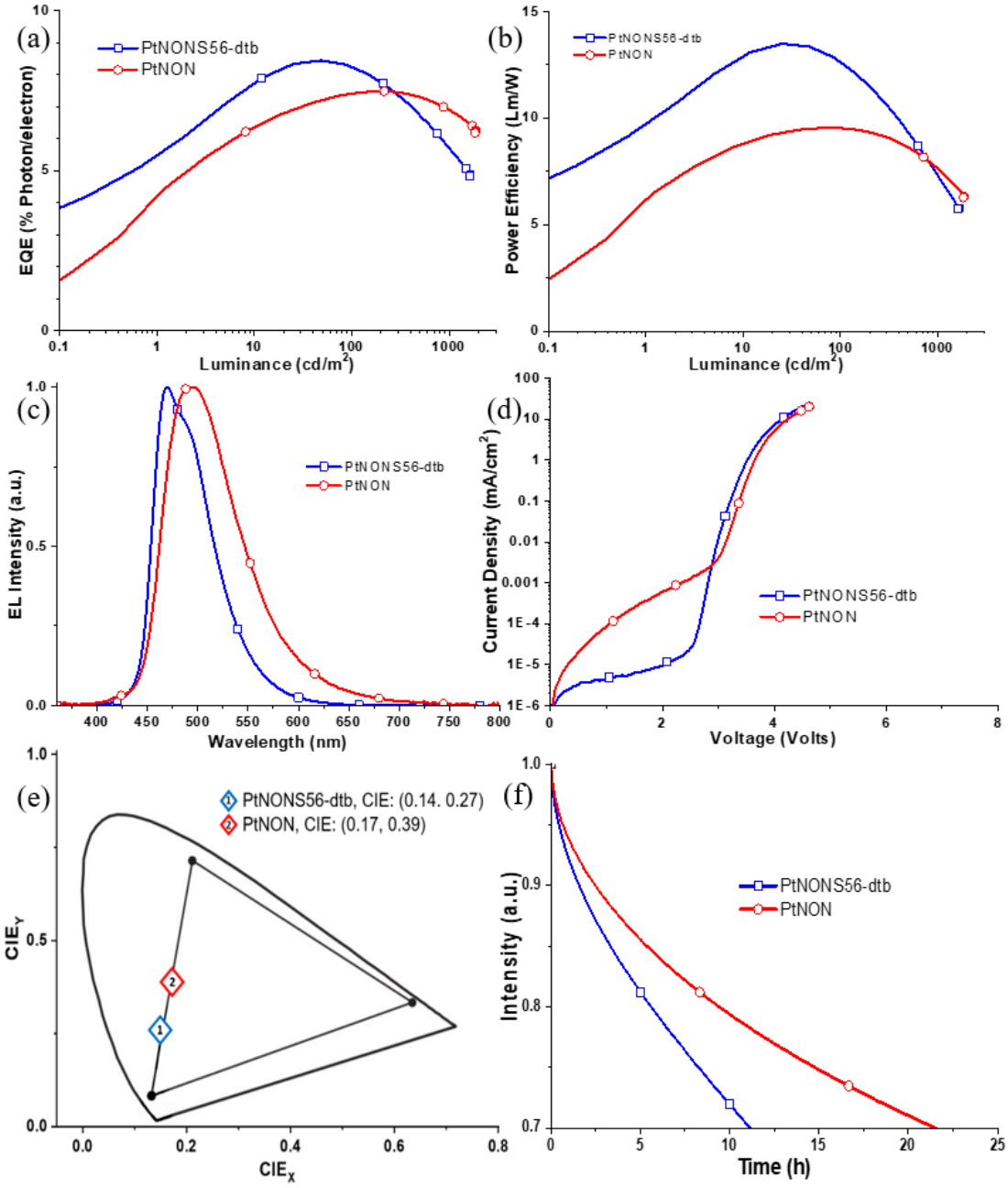

Figure 31. (a) External quantum efficiency versus luminance, (b) power efficiency versus luminance, (c) normalized electroluminescent spectra, (d) current density-voltage charactersitics (e) CIE coordinates, (f) normalized intensity versus device operational time of device 1 and device 2. Device structure: ITO/HATCN (10 nm)/NPD (40 nm)/TrisPCz (10 nm)/ 5% emitter:mCBT (10 nm)/BALq (10 nm)/BPyTP (40 nm)/Liq (2 nm)/Al with corresponding emitters of PtNONS56-dtb for device 1 and PtNON for device 2.

Device 1 achieved a peak EQE of 8.5%, which is superior to a peak EQE of device 2 (7.5%), as shown in Figure 31a. These two devices exhibited EQEs lower than 10%, which can be attributed to the thin emissive layer (10 nm). The peak power efficiency of device 1 is also higher than device 2 (Figure 31b). In the case of EL spectra in Figure 31c, device 1 exhibited an emission peak at 470 nm with a FWHM of 60 nm. On the other hand, device 2 showed an emission peak at 494 nm with a FWHM of 86nm, indicating the EL spectrum of the PtNONS56-dtb-based device is blueshifted and narrower than that of the PtNON-based device. The turn-on voltage, which is defined as the voltage required to reach an external brightness of 1 cd/m^2, of both devices was at about 2-3 V (Figure 31d).

Device 1 exhibited blue emission with a CIE coordinate of (0.14, 0.27) while device 2 yielded aqua blue emission with a CIE coordinate of (0.17, 0.39) at room temperature. These results support the design strategy of PtNONS56-dtb that has only T_1 emission by increasing the energy gap between T_1 and T_2. The stability of complexes was examined by device operational lifetime at a constant driving current of 20 mA/cm^2. Device 1 had the estimated operational lifetime to 70% of the initial luminance (LT_{70}) of 26.4 h at 1000 cd/m^2, which was inferior to device 2 (62.5 h at 1000 cd/m^2). The performances of operational lifetime indicate that the new complex, PtNONS56-dtb, has less molecular stability than PtNON in a device, which is possibly attributed to significant distortion on the extended conjugation and *t*-butyl portion of PtNONS56-dtb.

Table 4. Summary of device performances

[a)] Device structure: ITO /HATCN /NPD / TrisPCz /5% emitter:mCBT /BALq /BPyTP /Liq /Al
[b)] Estimated from the equation $LT(L_1) = LT(L_0)\cdot(L_0/L_1)^n$, where n is chosen to be 1.7.

Device [a)]	emitter	EQE (%)		Power efficiency (%)	EL spectrum		LT_{70} (h)		CIE
		peak	100 cd/m^2	peak	λ_{max} (nm) {FWHM, nm}	L_0 (cd/m^2)	L = L_0	L = 1000 cd/m^2 [b)]	(x, y)
1	PtNONS56-dtb	8.5	8.2	13.5	470 {60}	1648	11.3	26.4	(0.14, 0.27)
2	PtNON	7.5	7.4	9.5	494 {86}	1878	21.4	62.5	(0.17, 0.39)

2.4. Conclusion

In this chapter, new platinum complexes, PtNONS56 and PtNONS56-dtb, were designed and synthesized by the color tuning strategy that controls the energy gap between T_1 and T_2 to achieve narrowed and blueshifted emission spectra. For the characterization of these complexes, the electrochemical and photophysical properties were discussed in detail. The electrochemical properties of these Pt(II) complexes indicated that extending the conjugation has a negligible effect on both oxidation and reduction potential of the complex while introducing the electron-donating groups (-tBu) on the 4-position of the pyridyl rings shifts the reduction potential to more negative value without a change in the oxidation potential. Furthermore, these Pt complexes were highly emissive in solution and doped PMMA thin films with a luminescent lifetime in the range of microseconds. Additionally, the excited state properties of PtNONS56 and PtNONS56-dtb were strongly reliant on the structure modification on carbazole and pyridyl rings. Consequently, PtNONS56-dtb at room temperature in PMMA thin film demonstrated a significantly narrowed and blueshifted emission spectrum at 460 nm with a FWHM of 59 nm through the molecular structure modification strategy. Also, PtNONS56-dtb in a device achieved a peak EQE of 8.5% with CIE coordinates of (0.14, 0.27). With the incorporation of state-of-the-art host and blocking materials, the performance of PtNONS56-dtb devices will be further improved.

3. DEVELOPMENT OF NEW HOST AND CHARGE BLOCKING MATERIALS FOR EFFICIENT AND STABLE OLED DEVICES

Advanced OLED devices typically have multilayer structures including injecting, transporting, blocking, and emitting layers [89]. Therefore, it is essential to employ appropriate materials for each layer, which can greatly affect the recombination efficiency of holes and electrons in the emissive layer (EML) [60], [88]–[91]. In particular, the design of suitable host materials for the corresponding dopants is crucial because the high concentration of phosphorescent emitters can bring about triplet-triplet annihilation (TTA) or triplet-polaron quenching (TPQ) that possibly reduces device efficiency and operational lifetime [92]–[94]. Consequently, host-dopant systems are ordinarily adopted for EML in OLED devices. One of the important roles of host material is transferring the energy that is excited through the hole-electron recombination to the emitters effectively. Thus, host materials are required to have higher triplet energy (E_T) than phosphorescent emitters for preventing the undesirable reverse transfer of energy and confining triplet excitons in the emitter molecules efficiently. Also, the ability to inject and transport the charge carriers is essential for host materials with respect to the operational mechanism of OLED. It is preferred that holes and electrons have high and balanced mobilities in the host material for high charge recombination efficiency within the EML [95]. Additionally, the electron blocking layer (EBL) is another critical element to fabricate stable and efficient OLED devices. In general, triplet excitons of host materials or emitters have a long diffusion length to the adjacent layers due to their long lifetime [96], [97]. Therefore, blocking materials are required to have high E_T for preventing unwanted energy transfer and confining the triplet excitons within EML. The

appropriate HOMO and high LUMO levels of the EBL materials are desirable as well for injecting holes into EML and blocking electrons effectively [98].

Here, we designed two new regioisomer materials, i.e., 5,12-diphenyl-5,12-dihydroindolo[3,2-a]carbazole (BCN34) and 5,7-diphenyl-5,7-dihydroindolo[2,3-b]carbazole (BCN54), which can be employed as either host materials or EBL materials (Figure 32). The synthesis, electrochemical, and photophysical properties of two materials will be dicussed in detail. Both materials were used as EBL materials in devices employing Pd3O3 as an emitter to examine their molecular stabilities. Notably, the device using BCN34 as an EBL showed good molecular stability by achieving the estimated operational lifetime to 80% of the initial luminance (LT_{80}) of 12509 h at 1000 cd m^{-2} with a peak EQE of 30.3%. And then, BCN34 was employed as a host material in devices. The device with a bi-layer EML structure, which used BCN34 and CBP as host materials doped with PtN3N emitter, achieved a peak EQE of 16.5% with the estimated operational lifetime to 97% of the initial luminance (LT_{97}) of 351 h at 1000 cd m^{-2}.

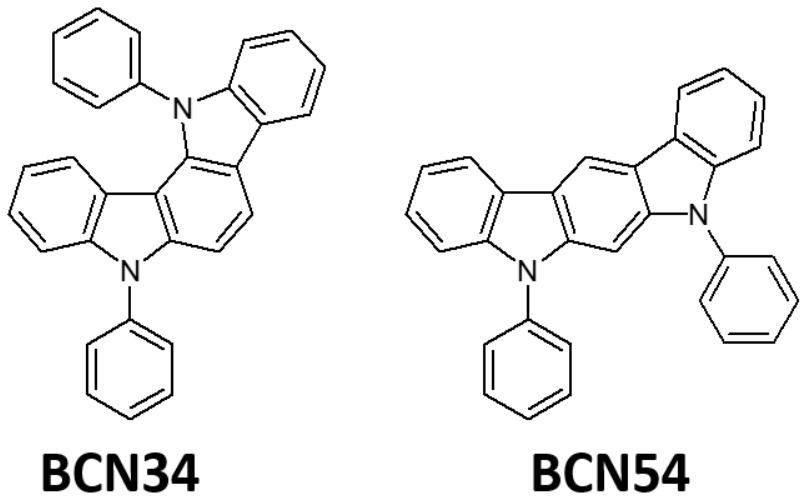

Figure 32. Structures of (a) BCN34 and (b) BCN54.

3.1. Requirement and examples of host and electron blocking material

One of the important roles of host material is transferring the energy that is excited through the hole-electron recombination to the emitters effectively. Thus, host materials are required to have higher triplet energy (E_T) than phosphorescent emitters for preventing the undesirable reverse transfer of energy and confining triplet excitons in the emitter molecules efficiently. Typically, host materials with E_T over 2.8 eV are needed in OLED devices involving blue phosphorescent emitters [73]. Also, the ability to inject and transport the charge carriers is essential for host materials with respect to the operational mechanism of OLED. It is preferred that holes and electrons have high and balanced mobilities in the host material for high charge recombination efficiency within the EML [95].

In the case of the electron blocking materials, they are required to have high E_T for preventing unwanted energy transfer and confining the triplet excitons within EML. The appropriate HOMO and high LUMO levels of the EBL materials are desirable as well for injecting holes into EML and blocking electrons effectively [98].

Based on the above requirements, the carbazole-based moiety has been widely used as the core structure of host materials or EBL materials. Some well-known carbazole-based host materials are 4,4′-bis(9-carbazolyl)-1,1′-biphenyl (CBP), 3,5-bis(9-carbazolyl)benzene (mCP), and 3,3′-bis(9-carbazolyl)-1,1′-biphenyl (mCBP) [99]–[101]. And extensively used carbazole-based EBL materials are 9,9′,9″-triphenyl-9H,9′H,9″H-3,3′:6′3″-tercarbazole (TrisPCz) and 4,4',4"-tris(carbazol-9-yl)-triphenylamine (TCTA) [100], [102]. The molecular structures are in Figure 33.

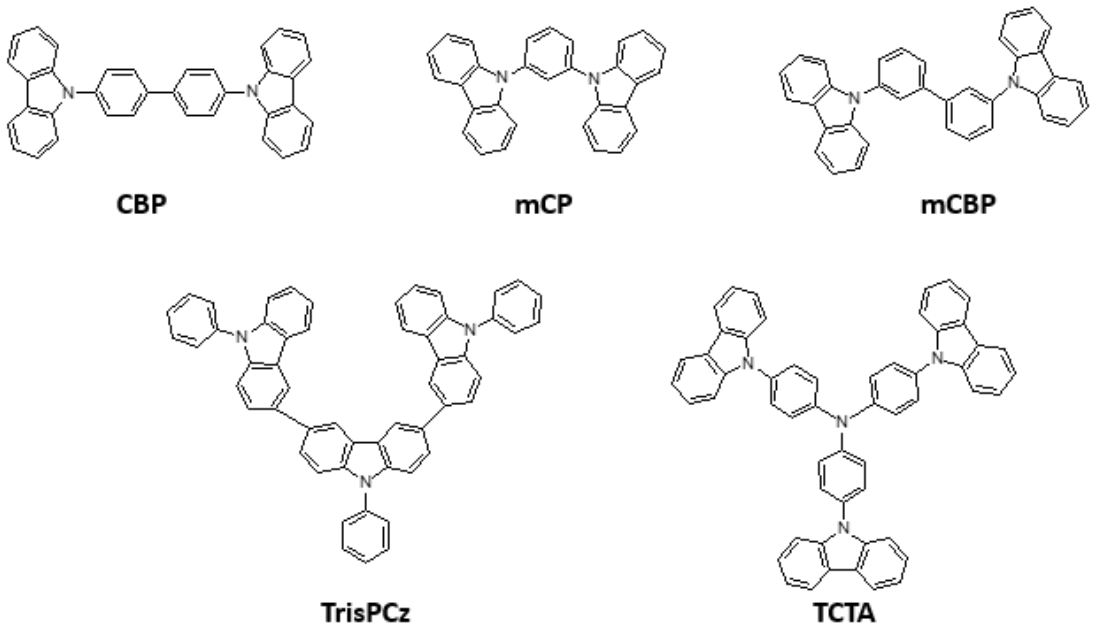

Figure 33. Structures of CBP, mCP, mCBP, TrisPCz, and TCTA.

3.2. Experimental section

Synthesis of Materials. The regioisomer materials, BCN34 and BCN54, are designed by incorporating 1-phenyl-1H-indole on 3, 4 positions and 5, 4 positions of 9-phenylcarbazole, respectively (Figure 32). Both materials have the indolocarbazole core structure that shows good hole mobility. BCN34 and BCN54 were synthesized through the routes as described in Figure 34. The initial step is the Suzuki coupling reaction of 9-phenyl-9H-carbazol-3-yl-3-boronic acid (**1**) and 1-bromo-2-nitrobenzene (**2**) catalyzed by $Pd(dppf)Cl_2 \cdot CH_2Cl_2$ to get the intermediate **3,** where $Pd(dppf)Cl_2 \cdot CH_2Cl_2$ is (1,1'-bis(diphenylphosphino)ferrocene)palladium(II) dichloride. Then, ring closure was achieved through a reduction reaction induced by excess PPh_3, which produces the regioisomer molecules **A** and **B**.

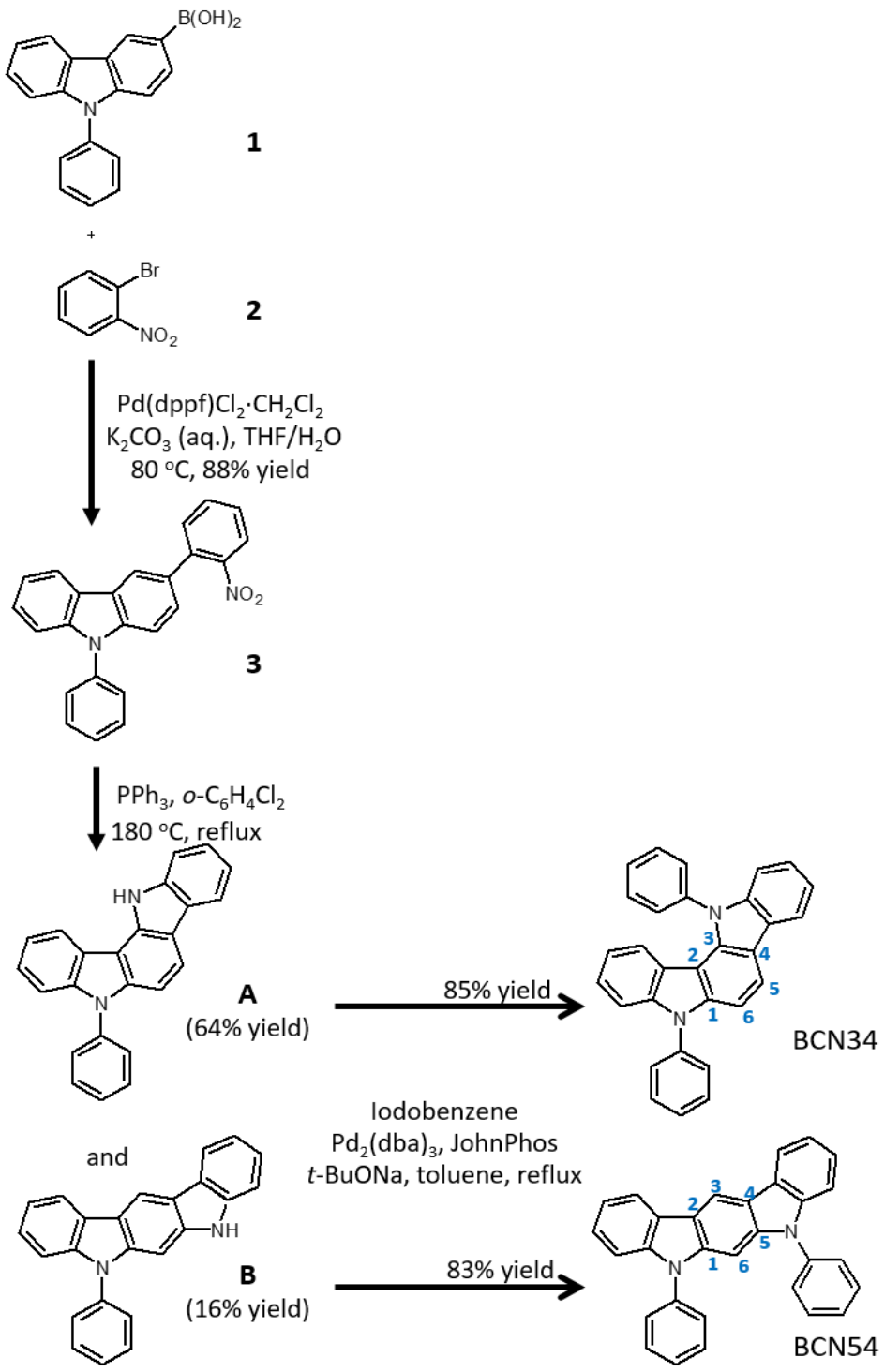

Figure 34. Synthetic routes of BCN34 and BCN54.

The intermediates, **A** and **B**, were coupled with functionalized iodobenzene catalyzed by $Pd_2(dba)_3$/JohnPhos under nitrogen atmosphere, where $Pd_2(dba)_3$ is tris(dibenzylideneacetone)dipalladium and JohnPhos is (2-biphenyl)di-tert-butylphosphine. BCN34 and BCN54 were prepared by this coupling reaction from the precursor A and B, respectively. Both two materials were characterized by ^{1}H NMR spectroscopy (Figure 35 and Figure 36).

5,12-diphenyl-5,12-dihydroindolo[3,2-a]carbazole (**BCN34**): To a solution of the precursor (5-phenyl-5,12- dihydroindolo [3,2-a]carbazole, 1.39 g, 4.18 mmol) in toluene (30 mL, 0.14 M) were added iodobenzene (2.56 g, 12.54 mmol), $Pd_2(dba)_3$ (192 mg, 0.209 mmol), JohnPhos (125 mg, 0.418 mmol), and *t*-BuONa (804 mg, 8.36 mmol). The mixture was heated to reflux for 24 h and cooled down to room temperature. Then, purification through silica gel for column chromatography (hexanes:DCM = 5:1) gave BCN34 (1.45 g, 3.55 mmol, yield: 85%) as a white solid. ^{1}H NMR (400 MHz, DMSO- d_6, δ): 8.31 (d, J = 8.6 Hz, 1 H), 8.24 (d, J = 7.7

Hz, 1 H), 7.79-7.58 (m, 10 H), 7.40-7.20 (m, 6 H), 6.74 (m, 1 H), 5.85 (d, *J* = 8.1 Hz, 1 H).

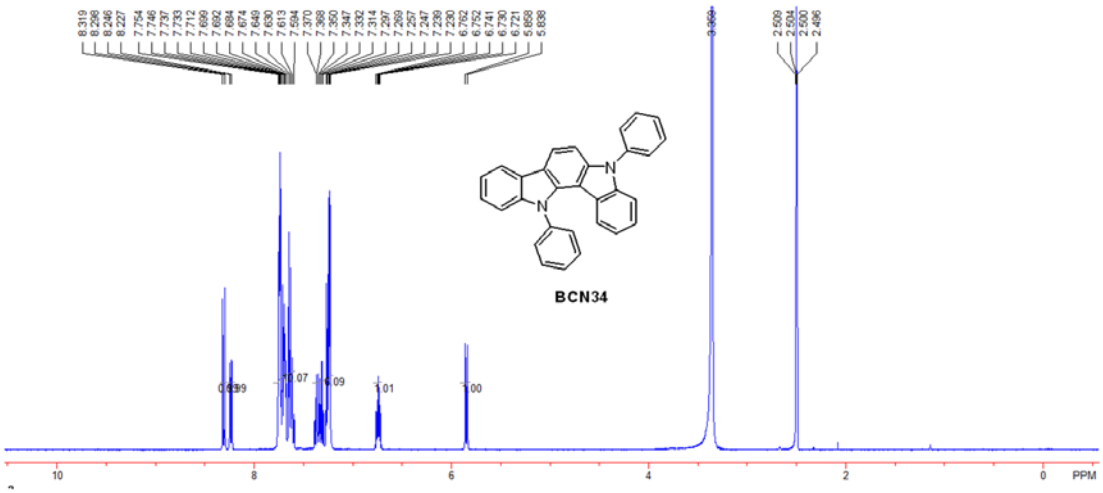

Figure 35. ^{1}H NMR spectrum of BCN34 at 400 MHz instrument in DMSO-d_6 solution.

5,7 diphenyl 5,7 dihydroindolo[2,3 b]carbazole (**BCN54**): To a solution of the pr ecursor (5-phenyl-

5,7 dihydroindolo[2,3b]carbazole, 910 mg, 2.74 mmol) in toluene (18 mL, 0.15 M) were added iodobenzene (1.68 g, 8.22 mmol), $Pd_2(dba)_3$ (126 mg, 0.137 mmol), JohnPhos (81. 8 mg, 0.274 mmol), and *t*-BuONa (526.68 mg, 5.48 mmol). The mixture was heated to re flux for 24 h and cooled down to room temperature. Then, purification through silica gel f or column chromatography (hexanes:DCM = 5:1) gave BCN54 (928.9 mg, 2.274 mmol, yield: 83%) as a white solid. ^{1}H NMR (400 MHz, DMSO-d_6, δ): 9.08 (s, 1 H), 8.34

-8.28 (m, 2 H), 7.66-7.59 (m, 8 H), 7.52-7.44 (m, 2 H), 7.40-7.33 (m, 2 H), 7.32 -7.26 (m, 4 H), 7.10 (s, 1 H).

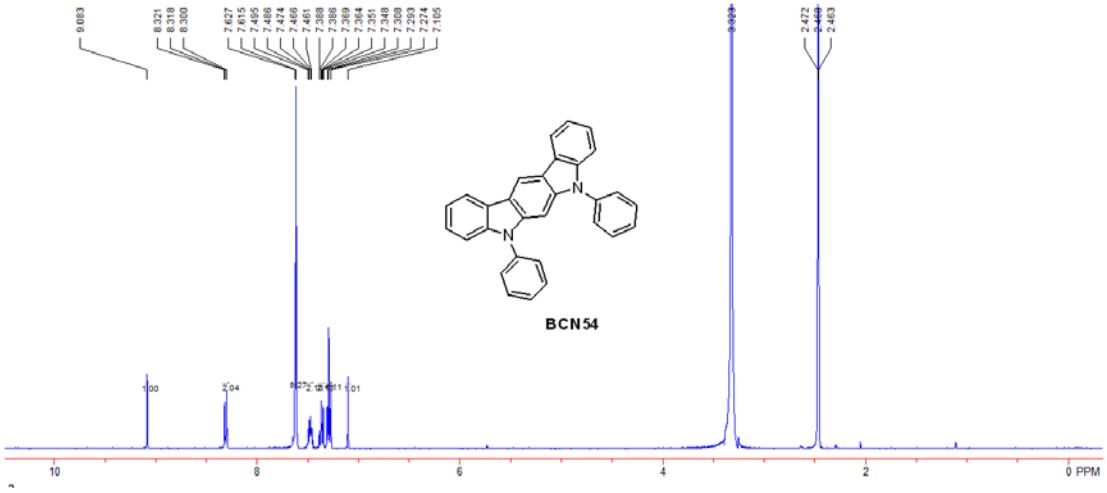

Figure 36. ^{1}H NMR spectrum of BCN54 at 400 MHz instrument in DMSO-d_6 solution.

Material characterization. For the cyclic voltammetry (CV) and different pulsed voltammetry (DPV) measurements, a CH Instrument 610B electrochemical a nalyzer was used. 0.1 M tetra(*n*-butyl) ammonium hexafluorophosphate and anhydrous dimethylformamide were used as the supporting electrolyte and the solvent, respectively, under a nitrogen atmosphere. Platinum, silver, and carbon were used as the counter electrode, pseudo-reference electrode, and working electrode, respectively.

Also, the absorption spectra were recorded on an Agilent 8453 UV-Visible Spectrometer. The photoluminescence (PL) spectra at room temperature were obtained on a Horiba Jobin Yvon FluoroLog-3 spectrometer in dichloromethane solution, and the cryogenic PL spectra were performed in 2-MeTHF at 77 K cooled with liquid nitrogen.

Device fabrication and characterization. The pre-patterned ITO coated glass substrate was cleaned by deionized water, acetone, and isopropyl alcohol. Organic materials, which were purified under high vacuum by sublimation with a four-zone thermal-gradient furnace, aluminum, and substrates were loaded in the custom-made vacuum thermal evaporation build by Travato Man. The organic materials were deposited on the substrates under high vacuum (between 10^{-8} and 10^{-7} torr). The depositing rates of organic materials were between 0.2 and 1.0 Å s^{-1} and that of aluminum cathode was 1 – 2 Å s^{-1} through a shadow mask. The current-voltage-luminance and EQE measurement were performed by a Keithley 2400 source meter with a Thorlabs FDS10X10 Si photodiode. EL spectra were measured by an Ocean Optics USB2000 spectrometer. All devices were tested in a nitrogen filled glovebox without encapsulation.

3.3. Results and Discussion

Electrochemical properties. The electrochemical properties of BCN34 and BCN54 were examined by using cyclic voltammetry (CV) and differential pulsed voltammetry (DPV). The oxidation and reduction potentials were measured relative to an internal ferrocenium/ferrocene (Fc^+/Fc) reference in anhydrous dimethylformamide (DMF) solution under a nitrogen atmosphere. All the redox potentials, the highest occupied molecular orbital (HOMO) energy levels, and the lowest unoccupied molecular orbital (LUMO) energy levels are summarized in Table 5. Both BCN34 and BCN54 showed irreversible oxidation at 0.62 V and 0.64 V, respectively. The reduction potential of BCN54 also exhibited an irreversible process at -2.95 V, while BCN34 had a quasi-reversible reduction process at -3.09 V (Figure 37). These results indicate that the position changes of the 1-phenyl-1H-indole group have a negligible effect on the

oxidation potentials. On the other hand, the reduction potential of BCN34 is found to be 140 mV more negative than BCN54. The HOMO levels of both materials are 5.5 eV, and the LUMO levels of BCN34 and BCN54 are 2.07 eV and 2.1 eV, respectively [76], [77]. Figure 38 is a reference CV data of CBP for comparing oxidation and reduction potentials with BCN34 and BCN54.

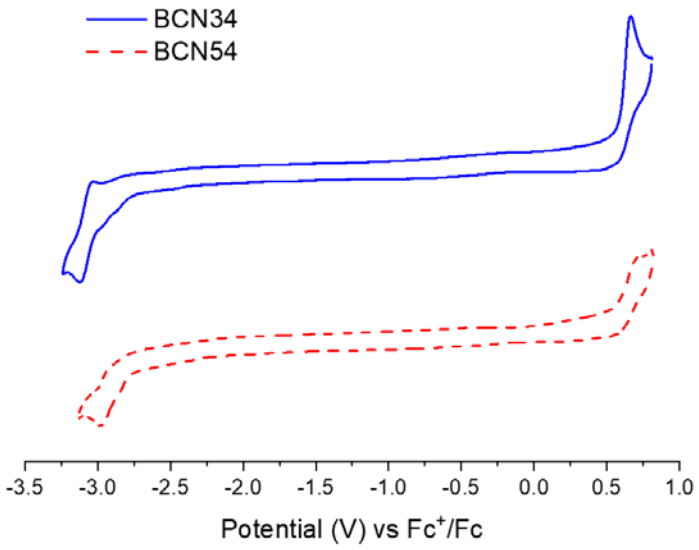

Figure 37. Cyclic voltammograms of BCN34 (blue solid line) and BCN54 (red dashed line).

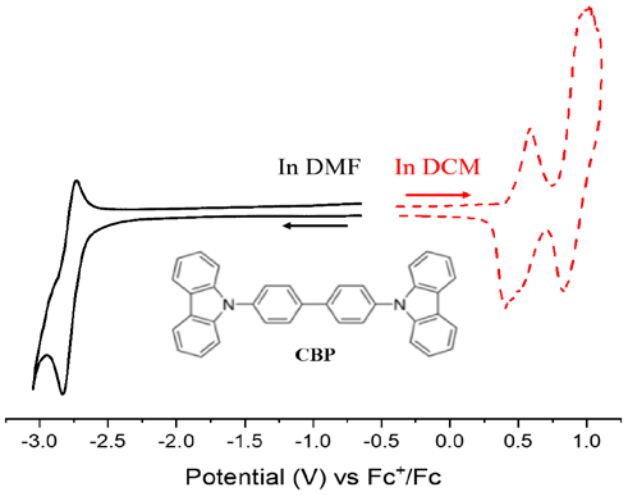

Figure 38. Cyclic voltammogram of CBP. (DMF: *N*,*N*-dimethylformamide; DCM: dichloromethane)

Table 5. Electrochemical and photophysical properties of BCN34 and BCN54.

The room temperature (RT) absorption and emission spectra were measured in a solution of dichloromethane and low temperature (77 K) emission spectra were measured in a solution of 2-methyl-THF. Triplet energies (E_T) are estimated from phosphorescent emission spectra at 77 K in 2-methyl-THF.

compound	absorption at RT	emission at RT		emission at 77 K						
	λ_{max} (nm) {ε, $10^4 cm^{-1}M^{-1}$}	λ_{PL} (nm)	τ (ns)	λ_{PL} (nm)	τ (μs)	E_T (eV)	E_{ox} (V)	E_{red} (V)	HOMO (eV)	LUMO (eV)
BCN34	272{4.37}, 284{4.80}, 310{2.67}, 324{1.43}, 345{1.12}, 361{2.02}	364, 382	3.7	428, 452	13.8	2.9	0.62	-3.09	5.5	2.07
BCN54	276{4.27}, 286{4.68}, 308{13.5}, 328{1.22}, 346{1.44}, 364{2.00}	368, 386	3.8	430, 456	14.1	2.88	0.64	-2.95	5.5	2.1

Photophysical properties. The absorption and emission spectra of BCN34 and BCN54 were measured, and the data are recorded in Table 5. The absorption spectra at room temperature are presented in Figure 39a. The high energy absorption bands between 250 and 290 nm ($\varepsilon > 3.5 \times 10^4$ cm^{-1} M^{-1}) are assigned to the aromatic group for both BCN34 and BCN54. Due to their identical amounts of phenyl rings, the extinction coefficient values of BCN34 at 272 nm ($\varepsilon = 4.37 \times 10^4$ cm^{-1} M^{-1}) and BCN54 at 276 nm ($\varepsilon = 4.27 \times 10^4$ cm^{-1} M^{-1}) are similar. The weaker absorption bands located in the 290-320 nm demonstrate somewhat different absorption between BCN34 at 310 nm ($\varepsilon = 2.67 \times 10^4$ cm^{-1} M^{-1}) and BCN54 at 308 nm ($\varepsilon = 1.35 \times 10^5$ cm^{-1} M^{-1}), which is possibly attributed to the position changes of the 1-phenyl-1H-indole group on carbazole moiety. The lowest energy absorption bands between 350 and 370 nm can be identified as the transitions to the lowest singlet energy state (S_1) based on the small energy shift at room temperature between absorption and emission. The extinction coefficient values of BCN34 at 361 nm ($\varepsilon = 2.02 \times 10^4$ cm^{-1} M^{-1}) and BCN54 at 364 nm ($\varepsilon = 2 \times 10^4$ cm^{-1} M^{-1}) are almost identical.

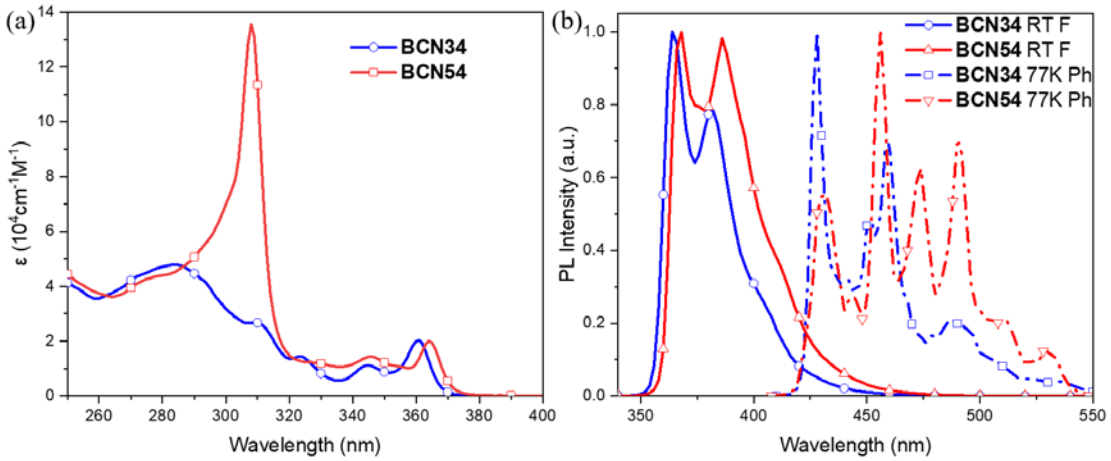

Figure 39. (a) Comparison of room temperature absorption spectra of BCN34 and BCN54 in CH_2Cl_2. (b) The fluorescent spectra (F) of BCN34 and BCN54 in CH_2Cl_2 solution at room temperature and their phosphorescent spectra (Ph) in 2-MeTHF solution at 77 K.

Figure 39b demonstrates the fluorescent spectra of BCN34 and BCN54 at room temperature in dichloromethane and their phosphorescent spectra at 77 K in 2-methyltetrahydrofuran. Both BCN34 and BCN54 had structured fluorescent emission spectra at room temperature with emission peak (λ_{max}) at short wavelengths of 364 and 368 nm, respectively. And they showed the luminescent lifetime (τ) values of 3.7 and 3.8 ns, respectively. The phosphorescent spectra of BCN34 and BCN54 at 77K exhibited peaks at short wavelengths of 428 and 430 nm with the luminescent lifetimes of 13.8 and 14.1 μs, respectively. Therefore, the triplet energy of BCN34 and BCN54 can be calculated to be 2.9 and 2.88 eV, respectively, which are sufficiently high energy to be employed as blockers or host materials in OLED devices with typical blue emitters as well as the red and green emitters [103], [104].

BCN34 and BCN54 as blockers for stable and efficient OLEDs. The molecular stabilities of BCN34 and BCN54 were investigated in a device setting by employing a palladium-based stable phosphorescent emitter, Pd3O3, which shows aggregate emission in the orange-red region of the visible spectrum [105]. BCN34 and BCN54 were used as electron blocking layers (EBL) in the devices because they demonstrated high triplet energy and appropriate energy levels of HOMO and LUMO (Table 5). The devices were fabricated and tested using a known stable structure, ITO /HATCN (10 nm) /NPD (60 nm) /EBL (10 nm)/ Pd3O3 (15 nm) /BAlq (10 nm) /BPyTP (40 nm) /Liq (2 nm) /Al (100 nm) with corresponding EBLs of BCN34 for device 1, BCN54 for device 2, TrisPCz for device 3, and no EBL for device 4 where HATCN is 1,4,5,8,9,11-hexaazatriphenylene-hexacarbonitrile, NPD is N,N′-diphenyl-N,N′-bis(1-naphthyl)-1,1′-biphenyl-4,4″-diamine, BAlq is bis(2-methyl-8-quinolinolato) (biphenyl-4-olato) aluminum, and BPyTP is 2,7-di(2,2′-bipyridin-5-yl)triphenylene (11, 32-35).

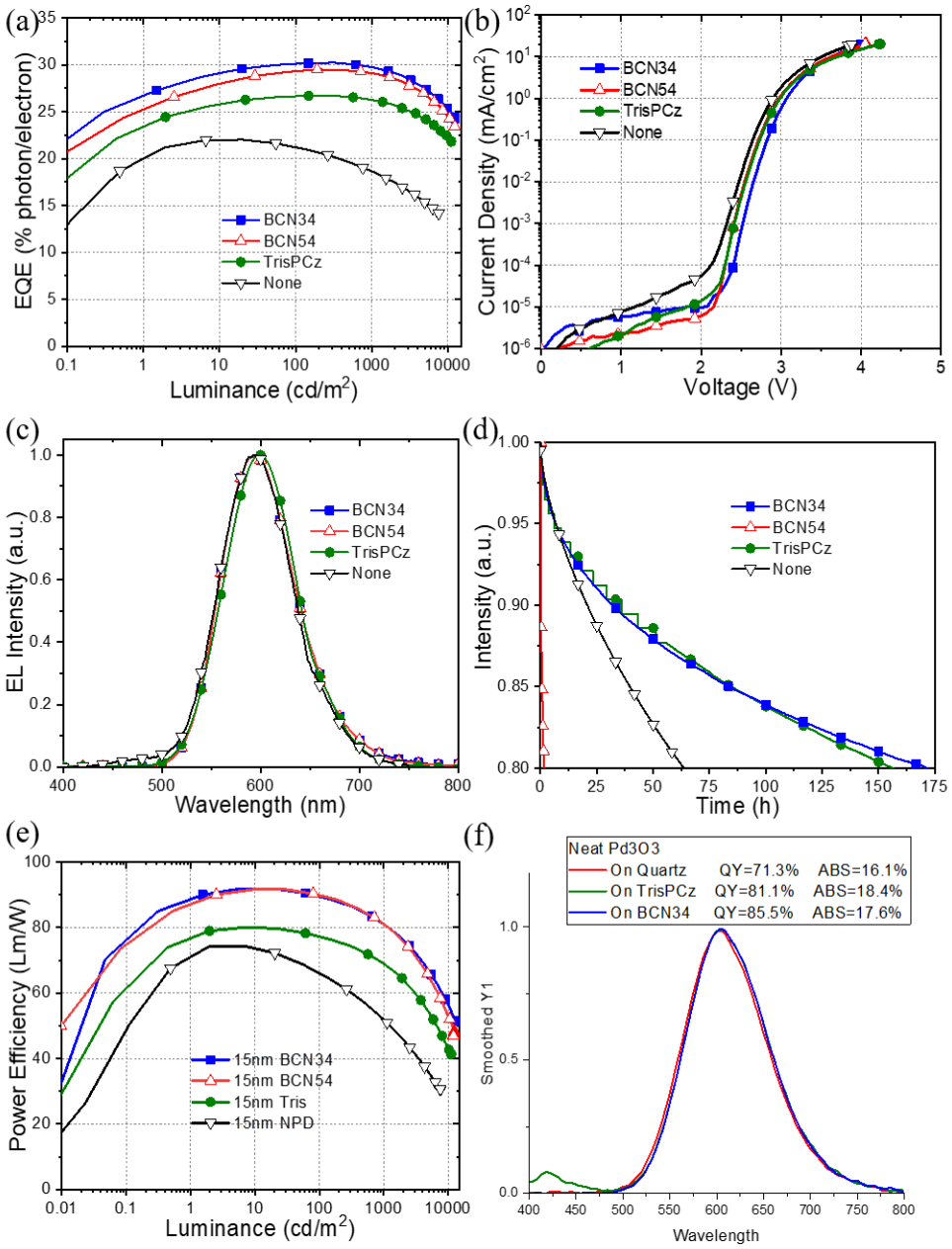

Figure 40. (a) External quantum efficiency versus luminance, (b) current density-voltage characteristics, (c) normalized electroluminescent spectra, (d) normalized luminance intensity versus operational time at constant current of 20 mA cm^{-2}, and (e) power efficiency versus luminance for the devices 1-4. (f) photoluminescent spectra of emitter thin films on quartz, TrisPCz, BCN34. Device structure: ITO /HATCN (10 nm) /NPD (60 nm) /EBL (10 nm) /Pd3O3 (15 nm) /BALq (10 nm) /BPyTP (40 nm) /Liq (2 nm) /Al with corresponding EBLs of BCN34 for device 1, BCN54 for device 2, TrisPCz for device 3, and no EBL for device 4.

TrisPCz is a well-known stable EBL material, which has similar HOMO and LUMO levels (5.6 eV and 2.1 eV) with lower triplet energy (2.7 eV) compared to BCN34 or BCN54 [100]. External quantum efficiency (EQE) versus luminance plots, current density-voltage (J-V) characteristics, electroluminescent (EL) spectra, luminance intensity versus operational time, power efficiency versus luminance of the devices and photoluminescent spectra of emitter thin films are presented in Figure 40, and the device performances are summarized in Table 6.

Device 1 and Device 2 demonstrated similar peak EQEs of 30.3% and 29.5%, respectively, which are superior to the peak EQE of device 3 (26.7%). Device 4 showed much lower peak EQE of 22.1%. Such different EQE values between device 1 and device 3 can be attributed to the photoluminescent quantum yield (PLQY) of the emitter. The PLQY value of Pd3O3 on BCN34 thin film is 0.86 ± 0.1, which is higher than that of Pd3O3 on TrisPCz thin film (0.81 ± 0.1). All the devices exhibited low turn-on voltages at about 2-3 V and broad emission spectra in the orange-red visible region with peaks at about 596 nm. Device 1 and Device 2 showed similar peak power efficiency of 91.6%% and 91.4%, respectively, which are superior to the peak power efficiency of device 3 (80.1%) and device 4 (74.1%).

Table 6. Summary of devices 1- 3 performances.

[a)] Structure of devices 1-4: ITO /HATCN /NPD /EBL /Pd3O3 /BAlq /BPyTP /Liq /Al.
[b)] Estimated from the equation $LT(L_1) = LT(L_0)\cdot(L_0/L_1)^n$, where n is chosen to be 1.7.

device [a)]	EBL	EQE (%)			Power Efficiency (Lm/W)	L_0 (cd/m^2)	LT_{80} (h) at L_0	LT_{80} (h) [b)] at 1000 cd/m^2	CIE (x,y)
		peak	100 (cd/m^2)	1000 (cd/m^2)					
1	BCN34	30.3	30.0	29.8	91.6	12470	171.5	12509	(0.55, 0.45)
2	BCN54	29.5	29.4	29.1	91.4	12324	1.6	114	(0.54, 0.45)
3	TrisPCz	26.7	26.6	26.3	80.1	11153	156.4	9436	(0.55, 0.44)
4	None	22.1	21.5	18.6	74.1	7567	64.2	2003	(0.55, 0.44)

The stability of device was evaluated by operational lifetime at a constant driving current of 20 mA cm^{-2}. Device 1 had the estimated operational lifetime to 80% of the initial luminance (LT_{80}) of 12509 h at 1000 cd m^{-2}, which was longer than that of device 3 (9436 h at 1000 cd m^{-2}). These performances indicated that the device with BCN34 had better EQE and operational stability than the device with TrisPCZ in this device setting. The device 4 showed 2003 h of LT_{80} at 1000 cd m^{-2}. On the other hand, the device 2 showed only 114 h of LT_{80} at 1000 cd m^{-2}, indicating the instability of BCN54 in a device setting. This can be attributed to the fast degradation of BCN54 potentially induced by less stable molecular structure than BCN34.

Device 5 and device 6 are same structures with devices 1-4 but the thickness of EML is increased to 25 nm. The EBLs are BCN34 for device 5 and TrisPCz for device 6. EQE versus luminance plots, J-V characteristics, EL spectra, luminance intensity versus operational time, power efficiency versus luminance of the device 5 and device 6 are shown in Figure 41.

Device 5 and device 6 demonstrated peak EQEs of 33.5% and 26.1%, respectively. Both devices exhibited low turn-on voltages at about 2-3 V and broad emission spectra in the orange-red visible region with peaks at about 596 nm. Device 5 and Device 6 showed peak power efficiencies of 99.3%% and 84.1%, respectively. And the device 5 had the estimated operational lifetime to 80% of the initial luminance (LT_{80}) of 2783 h at 1000 cd m^{-2}, which was shorter than that of device 6 (4706 h at 1000 cd m^{-2}).

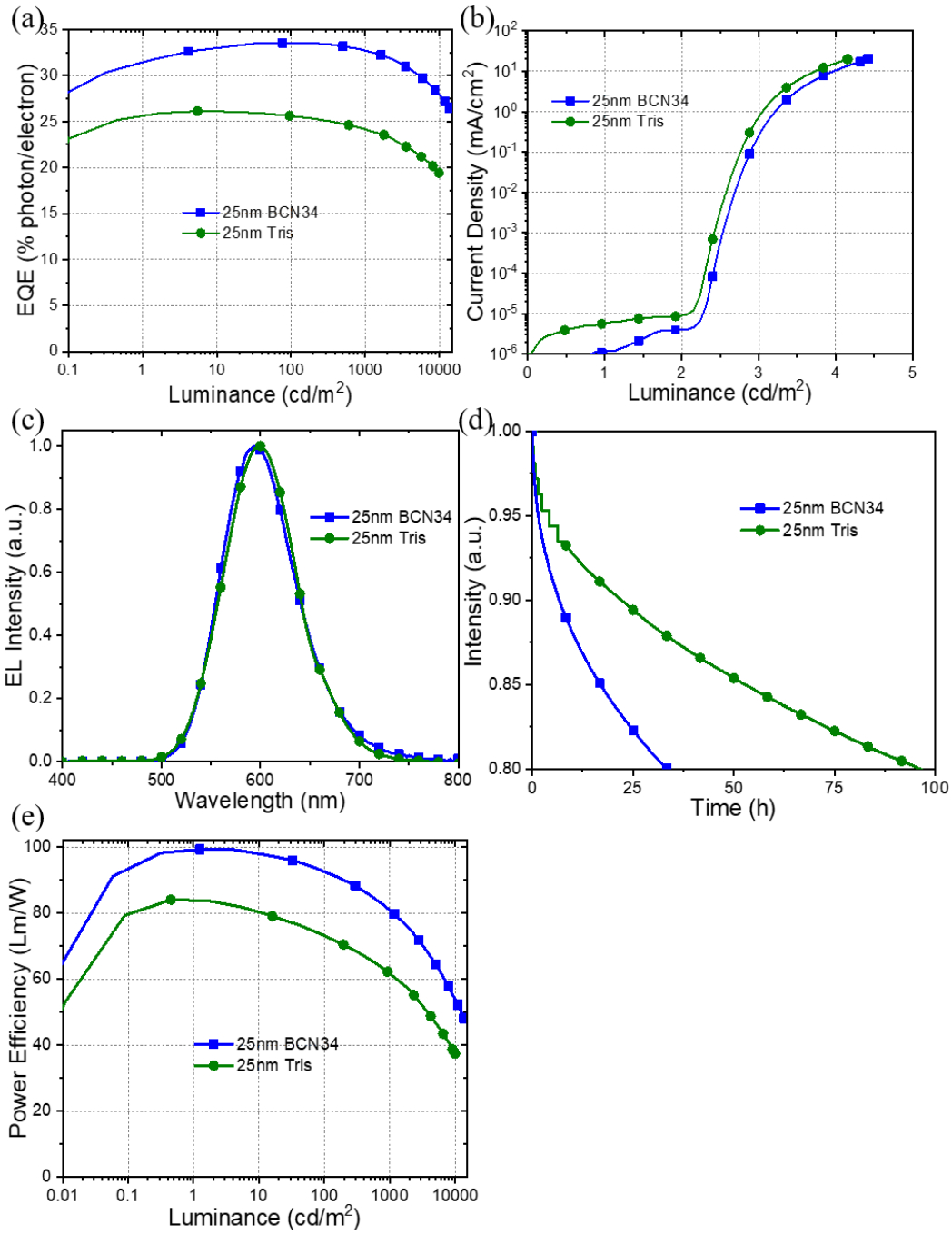

Figure 41. (a) External quantum efficiency versus luminance, (b) current density-voltage characteristics, (c) normalized electroluminescent spectra, (d) normalized luminance intensity versus operational time at constant current of 20 mA cm^{-2}, and (e) power efficiency versus luminance for the device 5 and device 6. Device structure: ITO /HATCN (10 nm) /NPD (60 nm) /EBL (10 nm) /Pd3O3 (25 nm) /BALq (10 nm) /BPyTP (40 nm) /Liq (2 nm) /Al with corresponding EBLs of BCN34 for device 5 and TrisPCz for device 6.

BCN34 as a host for stable and efficient OLEDs. BCN34 could also be employed as a host in OLED devices due to its molecular stability, high triplet energy, and good charge transporting ability. Recently, our group reported CBP-based orange-red OLED devices employing platinum complex, PtN3N, as an emitter [99]. In the paper, despite its high peak EQE, the single EML device showed low operational lifetime, which was possibly attributed to the electron build-up at the EBL-EML interface. It is believed that higher electron mobility than hole mobility within CBP caused the charge build-up. Therefore, BCN34 was used as a host because its indolocarbazole moiety can lead to higher hole transporting ability than CBP. Devices 7 and 8 were fabricated and tested using a known stable structure, ITO /HATCN (10 nm) /NPD (40 nm) /TrisPCz (10 nm) /10% PtN3N:Host (25 nm) /BALq (10 nm) /BPyTP (40 nm) /LiF (1 nm) /Al [99]. The corresponding host materials are CBP for device 7 and BCN34 for device 8.

The angle-dependent photoluminescence (PL) intensities of the *p*-polarized light for Pd3O3 in CBP and in BCN34 films are depicted in Figure 42a. The 10% doped PtN3N in CBP film (15 nm) on a bare glass maintained the horizontal emitting dipole ratio (Θ) value of 70%, where Θ is defined as the ratio of the horizontal emitting dipoles to the total emitting dipoles. On the other hand, the 10% doped PtN3N in BCN34 film (15 nm) on a bare glass showed lower Θ value of 67%. Additionally, the EQE versus luminance plots, J-V characteristics, luminance-device operational time, and electroluminescect spectra of device 7 and device 8 are plotted in Figure 42b-e, and the device performances are summarized in Table 7. As shown in Figure 42b, device 8 displayed a smaller peak EQE of 12.6% compared to device 7 (peak EQE of 18.2%), which could be attributed to its smaller Θ value and PLQY value. The PLQY value of

PtN3N in CBP thin film is 0.63 ± 0.1, which is lower than that of PtN3N in BCN34 thin film (0.55 ± 0.1).

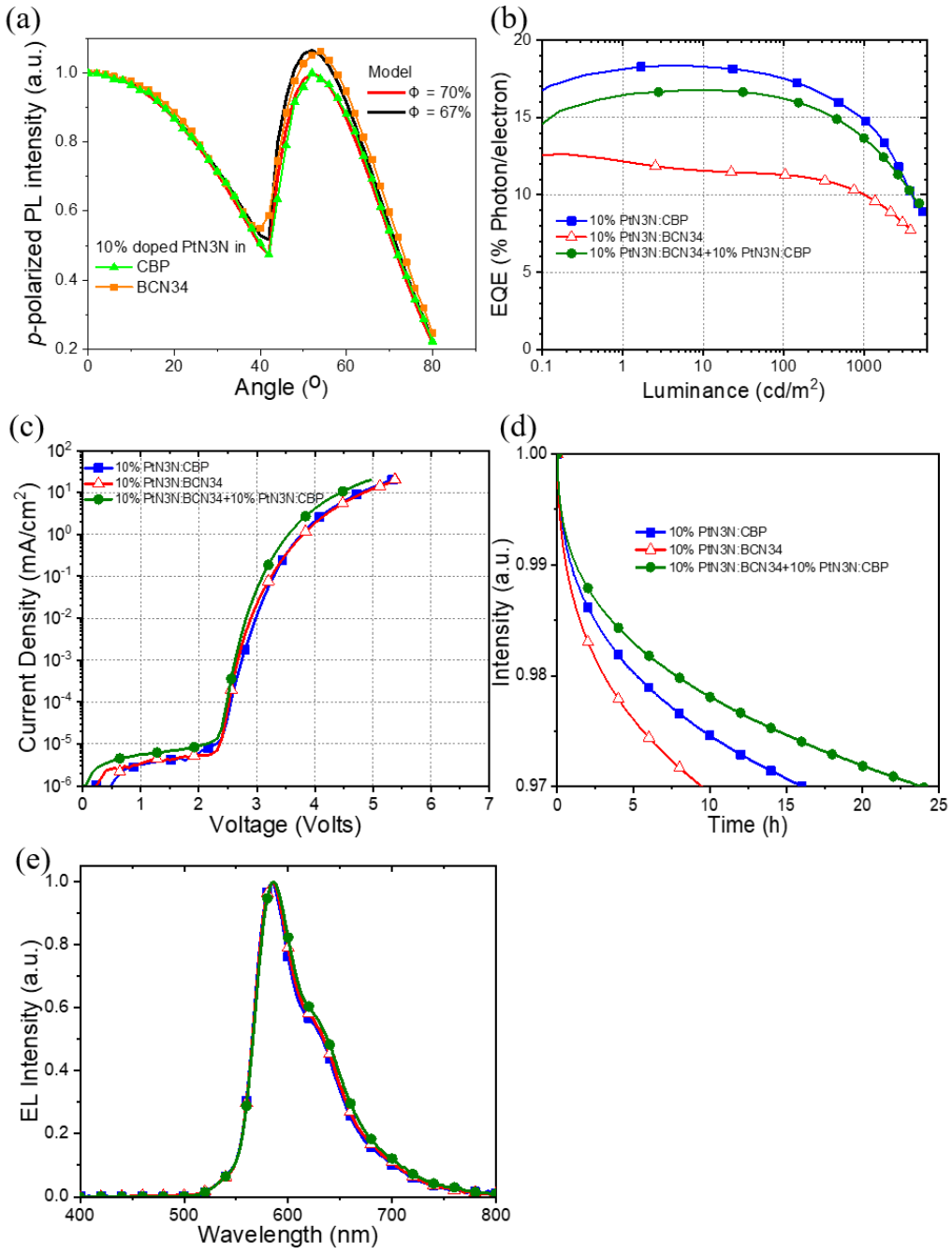

Figure 42. (a) Experimentally obtained angle-dependent PL intensities of the p-polarized light for 15 nm thick of 10% doped PtN3N in CBP and in BCN34 films grown on glass substrate. (b) EQE versus luminance, (c) J-V characteristics, (d) normalized luminance

intensity versus time at constant current of 20 mA cm^{-2}, and (e) normalized electroluminescent spectra for the devices 7-9. Device structure: ITO /HATCN (10 nm) /NPD (40 nm) /TrisPCz (10 nm) /EML /BALq (10 nm) /BPyTP (40 nm) /LiF (1 nm) /Al. The corresponding EMLs are 10% PtN3N:CBP (25 nm) for device 4, 10% PtN3N:BCN34 (25 nm) for device 5, and 10% PtN3N:BCN34 (15 nm) + 10% PtN3N:CBP (10nm) for device 6 [99].

Furthermore, both devices exhibited low turn-on voltages at about 2-3 V. Device 8 has an estimated operational lifetime to 97% of the initial luminance (LT_{97}) of 102 h at 1000 cd m^{-2}, which is even shorter than that of device 7 (281 h at 1000 cd m^{-2}), as shown in Figure 42d. This could be attributed to the imbalanced charge transporting ability of BCN34. Contrary to the property of CBP, it is believed that the hole mobility is higher than the electron mobility within BCN34, which can cause the hole build-up at the interface between EML and hole blocking layer (HBL). Therefore, the accumulation of holes at the interface potentially narrows the exciton formation zone, leading to the low operational lifetime of device 8.

To alleviate the charge accumulation at the EML-HBL interface, it is necessary to shift the exciton formation zone deep into the emissive layer, which can be achieved by employing a bi-layer EML with different host materials. BCN34 and CBP were used as host materials for the bi-layer structure with PtN3N as an emitter. Device 9 was fabricated and tested using a structure, ITO /HATCN (10 nm) /NPD (40 nm) /TrisPCz (10 nm) /10%PtN3N:BCN34 (15 nm) + 10%PtN3N:CBP (10nm) /BALq (10 nm) /BPyTP (40 nm) /LiF (2 nm) /Al. The EQE versus luminance plots, J-V characteristics, and luminance-device operational time for device 9 are plotted in Figure 42b-e, and the device performances are summarized in Table 7. Device 9 achieved a peak EQE of 16.5% and maintained EQE of 13.4% at the brightness of 1000 cd m^{-2}, which are improved compared to device 8.

Table 7. Summary of devices 7-9 performances.

[a)] Structure of device 4 and device 5: ITO /HATCN /NPD /EBL /10% PtN3N:Host /BAlq /BPyTP /LiF /Al.
Structure of devices 6: ITO /HATCN /NPD /EBL /10% PtN3N:BCN34 + 10% PtN3N:CBP /BAlq /BPyTP /LiF /Al.
[b)] Estimated from the equation $LT(L_1) = LT(L_0)\cdot(L_0/L_1)^n$, where n is chosen to be 1.7.

Device [a)]	Host material	EQE (%)			L_0 (cd/m^2)	LT_{97} (h) at L_0	LT_{97} (h) [b)] at 1000 cd/m^2	CIE (x,y)
		peak	100 (cd/m^2)	1000 (cd/m^2)				
7	CBP	18.2	17.4	14.9	5400	16.0	281	(0.55, 0.45)
8	BCN34	12.6	11.3	10.1	4086	9.3	102	(0.57, 0.43)
9	CBP, BCN34	16.5	16.0	13.4	4861	23.9	351	(0.57, 0.43)

Moreover, the LT_{97} of device 9 is 351 h at 1000 cd m^{-2}, which is much improved than device 7 and device 8 with single EML structures, as depicted in Figure 42d. These improved EQEs and operational lifetimes can support our device design strategy that shifts the exciton formation zone deep into the EML. The exciton formation zone is believed to be formed between BCN34-based and CBP-based EMLs because the transporting ability of hole is higher than that of electron in BCN34, while the electron mobility is higher than the hole mobility within CBP. The structures of devices 7-9 was depicted in Figure 43.

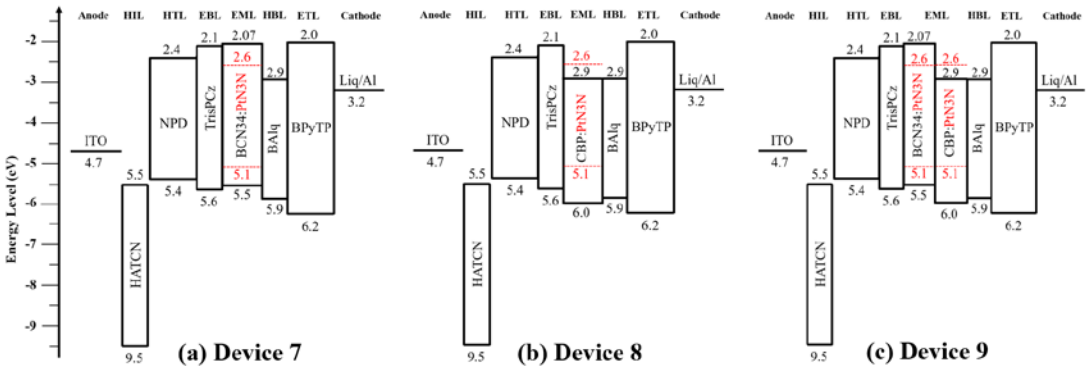

Figure 43. Energy level diagram for the PtN3N doped OLEDs (devices 4-6) using BCN34, CBP, or BCN34 and CBP as hosts. HIL, hole injection layer; HTL, hole transporting layer; EBL, electron blocking layer; EML, emissive layer; HBL, hole blocking layer; and ETL, electron transporting layer.

3.4. Conclusion

In this chapter, new indolocarbazole-based materials, BCN34 and BCN54, were designed and synthesized to have good hole mobility and high triplet energy. The electrochemical and photophysical properties were discussed to characterize BCN34 and BCN54. Owing to their high triplet energy and appropriate energy levels of HOMO and LUMO, both new materials were used as EBLs in devices employing Pd3O3 emitter. The

device using BCN34 as an EBL showed its good molecular stability by achieving the estimated LT_{80} of 12509 h at 1000 cd m^{-2} with a peak EQE of 30.3%. Also, BCN34 was employed as a host material in OLED devices. The device with bi-layer EML structure, which used BCN34 and CBP as host materials doped with PtN3N emitter, were fabricated and achieved a peak EQE of 16.5% with the LT_{97} of 351 h at 1000 cd m^{-2}. The device performances support our design principle of BCN34 to have higher hole transporting ability than electron transporting ability by employing the indolocarbazole moiety. With the incorporation of state-of-the-art blue phosphorescent emitters and device structures, efficient and stable devices employing BCN34 as an EBL or a host will be further fabricated.

4. EMULATING SHORT-TERM PLASTICITY WITH ORGANIC MEMRISTOR

A new class of emerging neuromorphic devices, namely, memristor or resistive random access memory (ReRAM), has been vigorously investigated. Memristors encode information in their resistance states according to the history of applied stimulations through the physical mechanism of ion or oxygen vacancy drift [43]–[45]. Therefore, long-term plasticity (LTP) and short-term plasticity (STP), which are the fundamental properties of biological synapses, can be implemented through memristive devices. In a biological system, LTP is regarded as a primary cellular substrate for learning and memory owing to its non-volatile characteristic, while STP is generally considered to perform a crucial computational role because its memory lasts only seconds to minutes [32]. However, the development of memristive devices has primarily focused on emulating LTP through the formation of conducting filaments composed of metal ions or oxygen vacancies. Many research groups implemented LTP by using memristors such as Ag/Si, SiN_x/a-Si, TiN/TaO_x, TiO_x/Al_2O_3, HfO_x/AlO_x based devices [106]–[110].

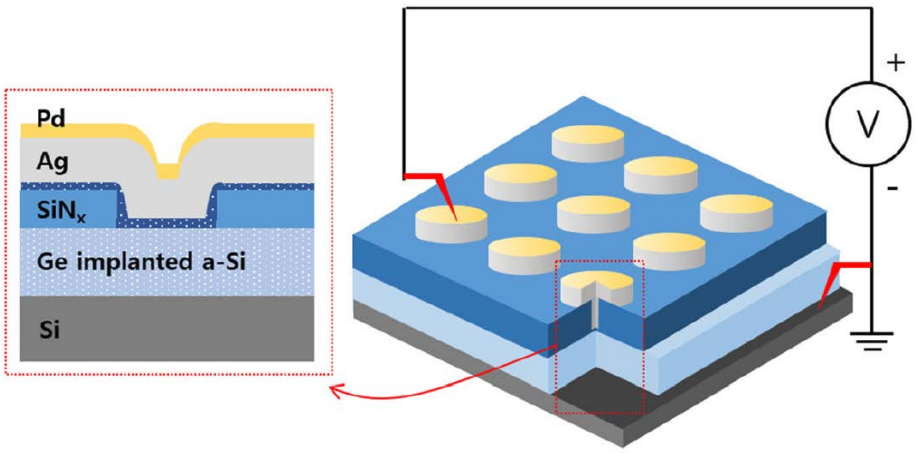

Figure 44. An example of LTP-based memristor: SiN_x/a-Si bilayer memristor structure [107].

On the other hand, a relatively small number of STP-based memristors have been developed, although their volatile characteristics can be used in spatio-temporal or reservoir computing in the recurrent neural network [111], [112]. The STP memristors are also potentially applicable to a synaptic memory, which comprises both long-term and short-term partitions, to improve learning efficiency as shown in Figure 45 [113]. Wang *et al.* demonstrated short-term memory (STM) properties using a SiO_xN_y/Ag diffusive memristor, but the device shows too short relaxation time compared to the biological synapse [114]. The STP behavior can also be found in GeSe/Ag based memristor. However, their uncontrollable weak filament possibly makes incoherent experimental data [115].

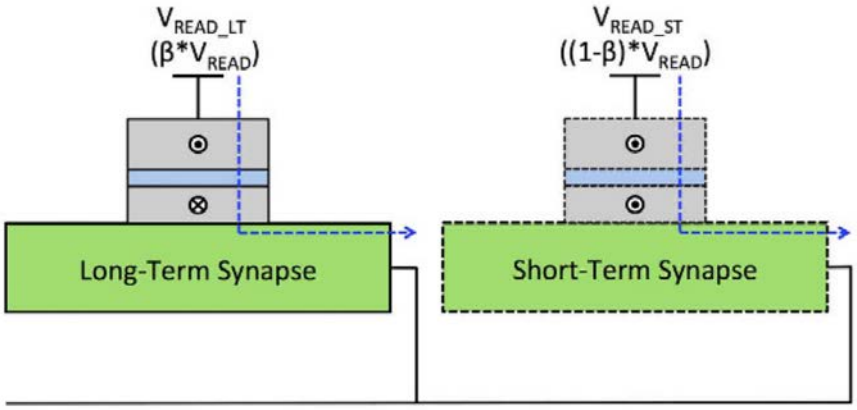

Figure 45. An example of STP-based memristor application as a synaptic memory by combining with LTP-based memristor [113].

Here, we mimic for the first time the STP properties of the biological synapse through an organic mixed ionic-electronic conductor (OMIEC) memristor. OMIECs have been used in various applications such as batteries, light-emitting devices, transistors, sensors, and neuromorphic devices [116]–[120]. Interestingly, non-volatile OMIEC

memristors have been studied in the literature, but some OMIEC materials can also be employed as STP-based memristors due to the mechanisms similar to biological synapse [121], [122]. In this study, a ruthenium complex with varying concentrations of salts was used as an OMIEC memristor to have timescales similar to STP in a biological synapse. The ion conductivities of our OMIEC memristors were extracted from electrochemical impedance spectroscopy measurements and found to be closely correlated with the salt concentrations. Current-voltage characteristics, turn-on time, relaxation time, and PPF indices of OMIEC memristors are described as well to explain the correlation with biological synaptic properties. Finally, short-term synaptic plasticity is emulated by applying 4 + 1 spikes and measuring current to confirm the STP characteristics of our memristive devices.

4.1. Analogy between OMIEC memristor and biological synapses

Figure 46 shows similar operational mechanisms between a biological synapse and a ruthenium complex-based OMIEC memristive device. In a biological system, neurotransmitters were initially stored in synaptic vesicles (Figure 46a), which corresponds to the primary state of the OMIEC memristor as described in Figure 46b. The activation of the presynaptic neuron, i.e., a spike arrival in the biological presynaptic terminal, causes neurotransmitters to be released into the synaptic cleft and pile up on the AMPA receptors located in the postsynaptic membrane (Figure 46c) [123]. Similarly, applying an external voltage to the OMIEC memristor makes cations and anions migrate to the respective interfaces between the active layer and electrodes as shown in Figure 46d. And then, the accumulation of ions brings about the formation of electric double layers (EDLs) at the electrode interfaces, leading to the strong bending of the energy level

due to their high charge concentrations at the interfaces [124]. Figure 46e illustrates that the neurotransmitters in the biological system trigger the AMPA ion channels to be opened, and thus particular positive ions can travel into the postsynaptic terminal to convey a spike signal [125]. Likewise, by applying a sufficiently high voltage to the OMIEC memristive device, more ions can be accumulated on the electrode surfaces, which leads to a sharp increase in the electric field at the interfaces. Subsequently, the injection of electrons and holes is induced, and then electrochemically doped zones are formed, causing the current flow in the device through the charge recombination in the intrinsic region (Figure 46f) [126].

Therefore, the accumulation of ions plays a critical role in the OMIEC memristor, which demonstrates a similar operational mechanism with biological synapse for transmitting a signal by piling up neurotransmitters on receptors. For tuning the various short-term memory (STM) properties of OMIEC memristors, the ion conductivity in the device was optimized by adding salt. In this chapter, three devices with varied concentration of additive were designed; i.e., pristine $Ru(bpy)_3(PF_6)_2$ device (Device 0), $Ru(bpy)_3(PF_6)_2$ with 1 wt % of $LiClO_4$ device (Device 1), and $Ru(bpy)_3(PF_6)_2$ with 2 wt % of $LiClO_4$ device (Device 2). The schematic structure of our OMIEC memristive device is shown in Figure 47.

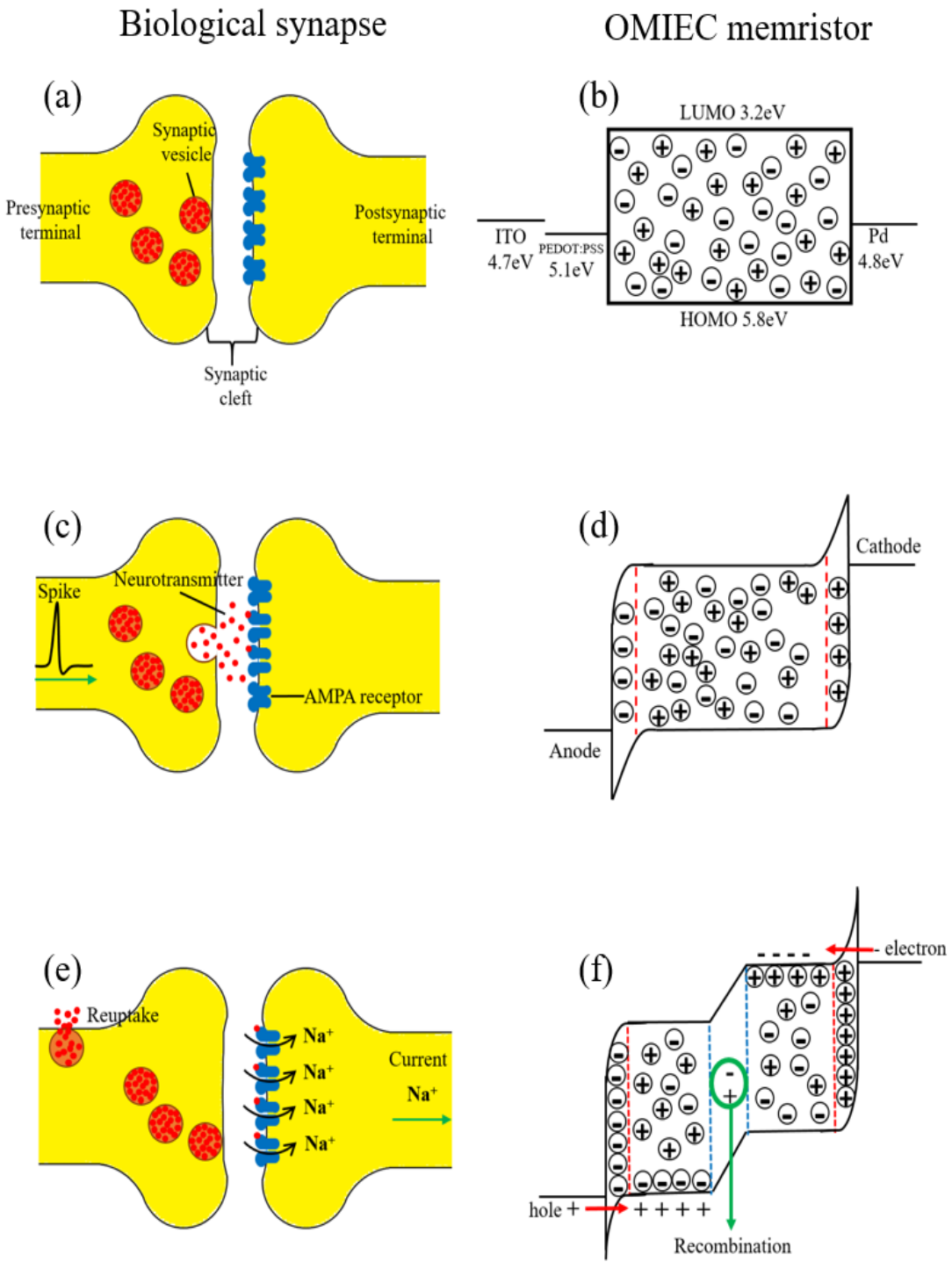

Figure 46. Schematic illustration of biological synapse and OMIEC memristor mechanisms.

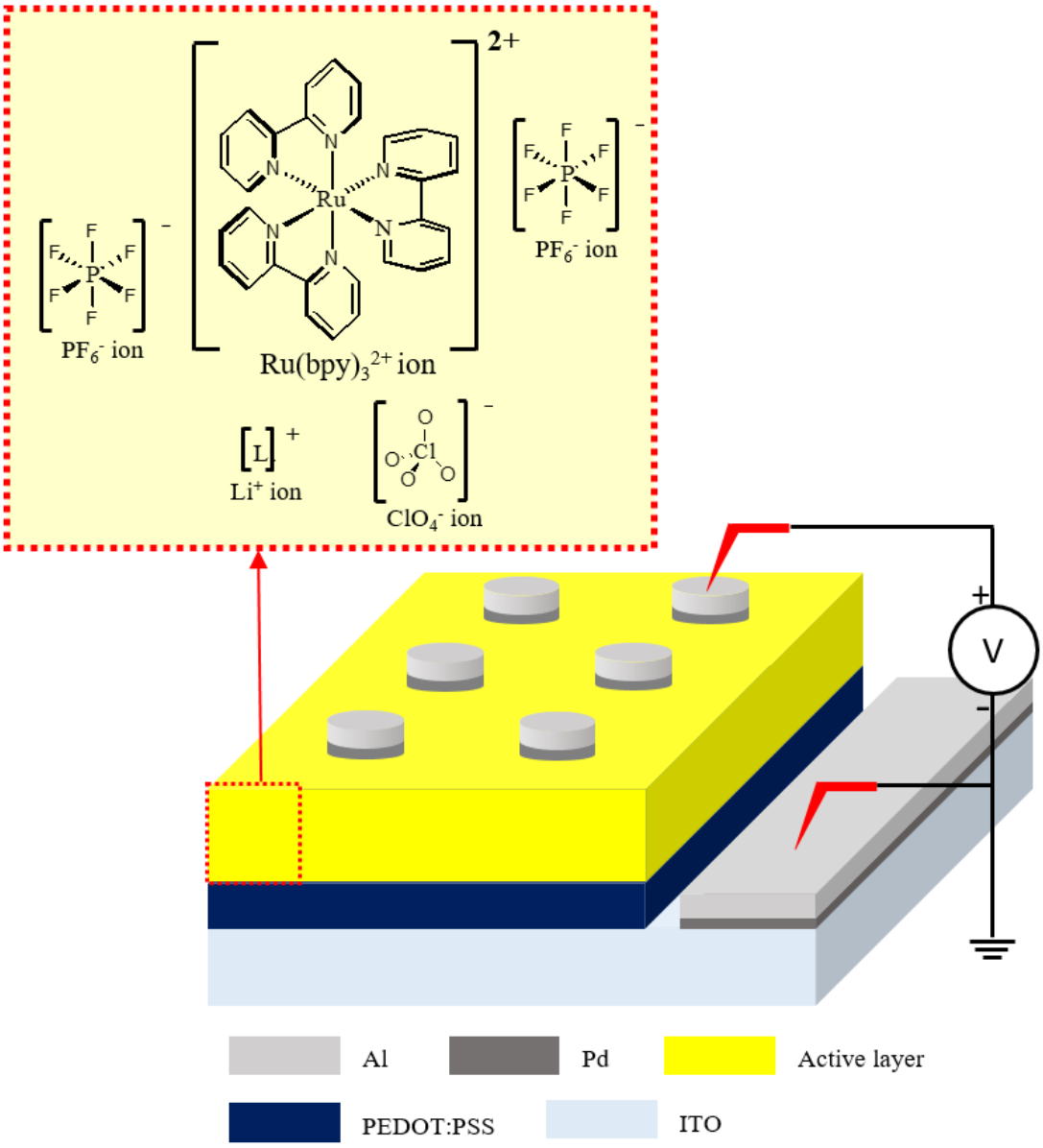

Figure 47. Schematic structure of an OMIEC memristive device. The active layer consists of $Ru(bpy)_3^{2+}$ ions and PF_6^- ions with various concentrations of Li^+ ions and ClO_4^- ions.

4.2. Experimental section

Preparation of active layer solution. Tris(2,2'-bipyridine)ruthenium(II) hexafluorophosphate ($Ru(bpy)_3(PF_6)_2$), lithium perchlorate ($LiClO_4$), and acetonitrile

were purchased from Sigma-Aldrich and used as received. Active layers consisted of $Ru(bpy)_3(PF_6)_2$ with varied concentrations of $LiClO_4$ salt additive. $Ru(bpy)_3(PF_6)_2$ and $LiClO_4$ solutions were separately prepared at the same concentration of 40 mg/mL in acetonitrile and mixed at a ratio by weight noted [127]. The mixed solution was kept on stirring overnight at room temperature and then filtered through a 0.2 μm PTFE membrane filter.

Device fabrication process. The overall OMIEC memristive device composition is as follows: ITO/PEDOT:PSS/active layer/Pd/Al. Indium tin oxide (ITO; 150 nm thick) coated glass substrates were cleaned with deionized water, acetone, and isopropyl alcohol. Then, the substrates were treated with oxygen plasma cleaning for 15 min. Poly(3,4-ethylenedioxythiophene):poly(styrenesulfonate) (PEDOT:PSS; Clevious PH 1000) filtered through a 0.45 μm nylon filter was spin-coated on the ITO substrates at 3000 rpm for 30 s followed by thermal annealing on a hot plate at 120 °C for 15 min (yielding 50 nm film). The active layer solutions were then spin-coated onto the PEDOT:PSS layers at 1500 rpm for 30 s. After the spin coating process of the active layer, the obtained films were annealed at 120 °C for 2 h under the nitrogen atmosphere. The $Ru(bpy)_3(PF_6)_2$ films with or without $LiClO_4$ were generally 100 nm thick. Before depositing the top electrode, a small part of the deposited layers (i.e., PEDOT:PSS and active layer) was scratched off using a sharp tweezer to expose the conductive ITO layer underneath, where is a connection point of the bottom electrode. Finally, the devices were completed with the deposition of 5 nm thick Pd and 200 nm thick Al through electron beam evaporation.

Characterizations. The ionic conductivities of the devices were measured by

electrochemical impedance spectroscopy using a Solartron SI-1260 gain/phase analyzer. The devices were measured with alternating voltage (100 mV amplitude) in the frequency range from 1 to 10^6 Hz. Impedance spectra were then fitted using MATLAB. The other electrical characterizations were conducted by a Keithley 4200 source meter connected with a probe station under the nitrogen atmosphere.

4.3. Results and discussion

Effect of salt concentrations on ion conductivity. Electrochemical impedance spectroscopy (EIS) was performed to understand how the concentration of $LiClO_4$ salt affects the trend of ion conductivity in the active layer of the OMIEC memristor. To minimize the influence of electronic carriers, the offset voltage was set to 0 V so that the inherent potential of the contacts prevented the electronic charge injection into the active layer. The frequency-dependent impedance and phase spectra of OMIEC memristors are illustrated in Figure 48.

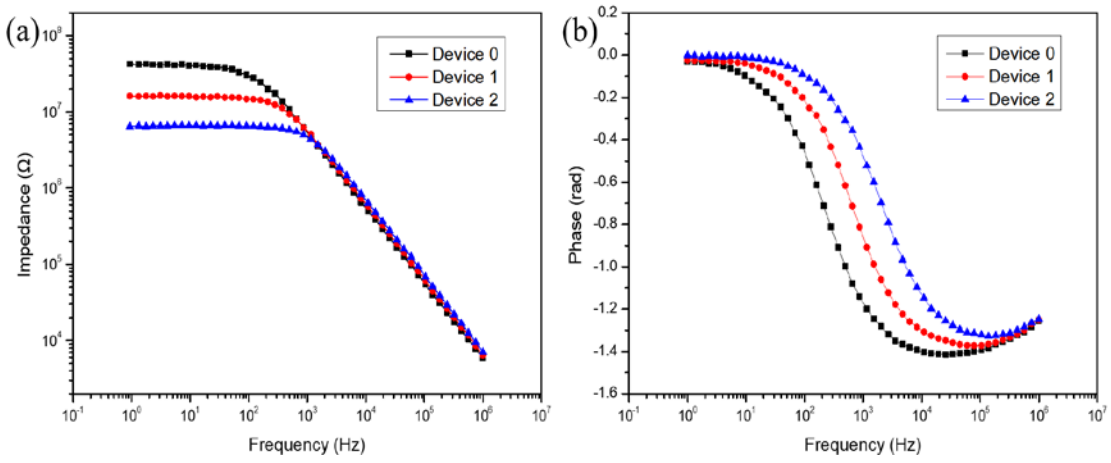

Figure 48. EIS of $Ru(bpy)_3(PF_6)_2$ memristor devices with different concentrations of $LiClO_4$ additives. (a) Impedance versus frequency data and (b) phase versus frequency data for Device 0 (black square), Device 1 (red circle), and Device 2 (blue triangle).

The impedance plateaus in the low-frequency range in Figure 48a indicate a strong correlation with the fraction of the lithium salt additive. Namely, with an increasing concentration of $LiClO_4$ from 0 to 2 wt %, a decreased impedance plateau was observed. The ion conductivity of Device 0 only depends on the anions (PF_6^- ions) as a result of negligible $Ru(bpy)_3^{2+}$ ion mobility because the cations are bulky in their size. Therefore, the low cation conductivity was compensated by adding Li^+ ions that are smaller in their size and thus have higher mobility than $Ru(bpy)_3^{2+}$ ions. Consequently, the device with a higher concentration of $LiClO_4$ salt showed a decreased impedance plateau in Figure 48a. A similar trend can be found in the previously reported literature [128]–[130].

For additional analysis of the EIS data, an equivalent circuit was modified and employed for our memristor devices as shown in Figure 49 [131]–[133]. The selected equivalent circuit includes a parallel circuit which consists of total electrical resistance of active layer (R_E), a constant phase element of geometric capacitance (CPE_{GEO}), capacitors of the electric double layers (EDLs) at the anode and cathode (C_{EDL1} and C_{EDL2}), resistances of the EDLs (R_{EDL1} and R_{EDL2}), and bulk ionic resistance of active layer (R_{ions}). This parallel circuit is connected with all external resistance (R_{EXT}) in series. Constant phase element (CPE) was used because it is a model of an imperfect capacitor in an equivalent electrical circuit [133]. The impedance of the CPE can be described by the function

Equation 3

$$Z_{CPE} = 1 / (Q(i\omega)^{\alpha})$$

where ω is the applied frequency, Q is the magnitude of 1/|Z| at ω = 1 rad/s, and α is the phase of the element. Q does not have meaningful physical value, but Q is a capacitor or a resistor when α is 1 or 0, respectively.

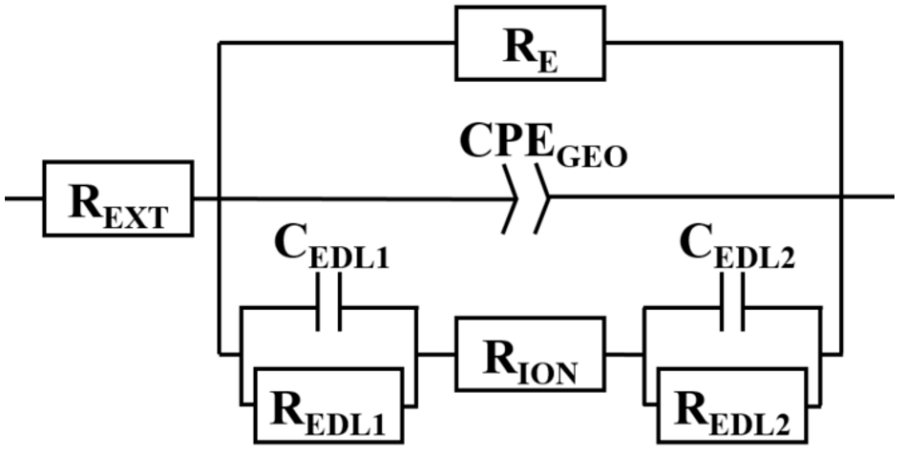

Figure 49. Illustration of equivalent circuit employed for EIS fitting of OMIEC memristor devices.

The spectra data of Figure 48a and 48b were fitted to extract typical device parameters from the equivalent circuit (provided in Table 8). The decreased bulk ionic resistance (R_{ION}) was observed in the device with a higher Li^+ concentration, which corroborates the trend of the impedance plateau. The calculated ion conductivities σ in the active layer are 2.79×10^{-11} S/cm for Device 0, 7.72×10^{-11} S/cm for Device 1, and 1.9×10^{-10} S/cm for Device 2.

Pinched memristor hysteresis behavior. One of the distinctive signatures of the memristor is the hysteresis loop pinched at the I-V origin [134]. Figure 50a demonstrates a typical hysteresis loop with the ion distributions of our OMIEC memristive device while the voltage is swept. When a negative voltage is applied to the initial state (step 1)

of the device, the ions build up on the electrode surfaces, and then the recombination current starts to flow as shown in step 2. However, it is challenging for electrons and holes to be injected into the active layer owing to the relatively small amount of accumulated ions in step 2.

Table 8. Parameters extracted from the equivalent circuit model of OMIEC memristor devices.

	R_{EXT} (kΩ)	R_E (MΩ)	Q_{GEO} ($\times 10^{-11}$)	α_{GEO}	R_{ION} (MΩ)	C_{EDL1} (nF)	R_{EDL1} (pΩ)	C_{EDL2} (nF)	R_{EDL2} (pΩ)
Device 0	40	233	4.6	0.87	51.1	71	3.7	88	3.9
Device 1	40	125	4.8	0.86	18.5	24	8.3	74	4.8
Device 2	40	49.8	5.1	0.85	7.5	93	4.2	53	7

On the other hand, step 3 shows more accumulated ions on the electrode surfaces than step 2, which leads to a sharp increase in the electric field near the interfaces and promoting the injection of electrons and holes. Therefore, the value of recombination current in step 3 is much higher than that of step 2 despite their same applied voltage. It is worth noting that our OMIEC memristive device remembers its most recent resistance through the number of accumulated ions. Also, it can be observed that the accumulated ions on the electrode surfaces diffuse back to their stable state very fast, which is a characteristic of STM. Steps 4 and 5 indicate the same phenomenon as steps 2 and 3 when a positive voltage is applied to the OMIEC memristor.

Figure 50b-d shows the hysteresis curves pinched at the origin in current-voltage (I-V) sweep graphs. The I-V curves of our OMIEC memristors were obtained by sequential direct voltage sweep from 0 V to -4 V and from 0 V to +4 V with a scan rate of 0.1 V/s. In Figure 50b-d, a broad shape of hysteresis was obtained for Device 0, while the hysteresis shape is narrower for Device 1 and the narrowest for Device 2. The device with a higher concentration of additive acquired a narrower shape of the hysteresis because it shows faster ion accumulation and diffusion in the active layer. Figure 51, which is the I-V curves in semi-log scales of devices, demonstrated that the turn-on voltages of devices are between 2-3 V for all three memristive devices.

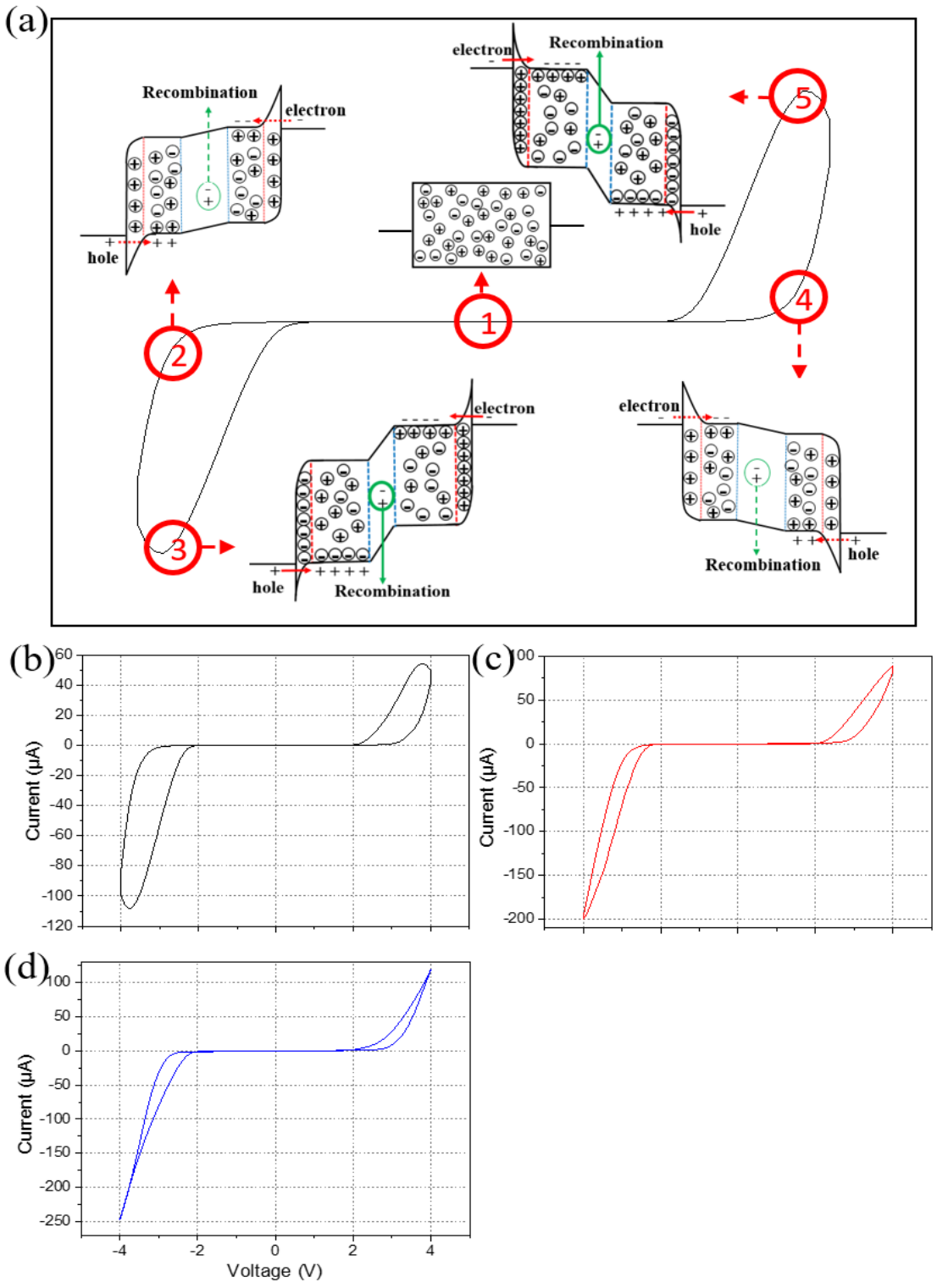

Figure 50. (a) A representative current versus voltage curve and the ion distributions of the OMIEC memristor describing each sequential step. The numbers on the curve indicate the initial state at 0 V for step 1 (①), negatively biased states at -3.5 V for step 2

(②) and step 3 (③), positively biased states at 3.5 V for step (④) and step 5 (⑤). Current-voltage curves of (b) Device 0, (c) Device 1, and (d) Device 2. The voltage was swept following the sequence 0 → -4 → 0 → +4 → 0 with a scan rate of 0.1 V/s.

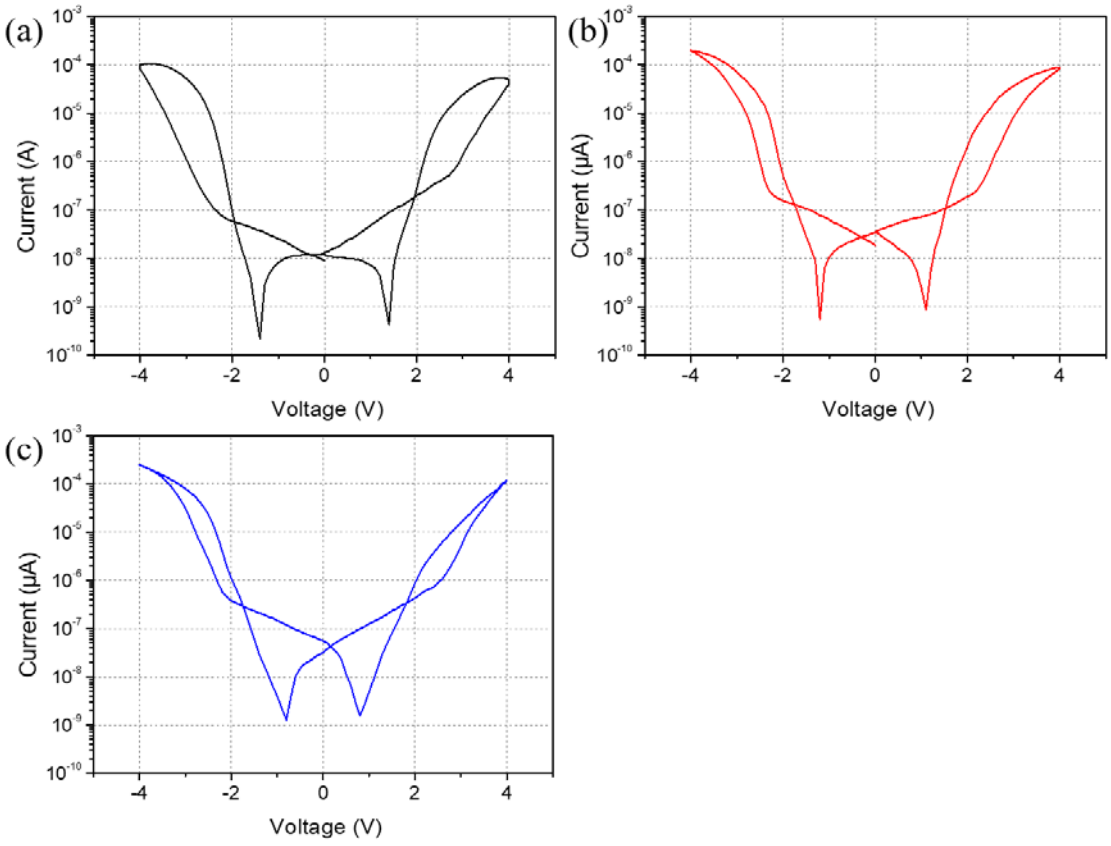

Figure 51. Current versus voltage curves in semi-log scales of (a) Device 0, (b) Device 1, and (c) Device 2.

turn-on time and relaxation time. Turn-on time is the time it takes for ions to accumulate on electrode surfaces due to the low ionic conductivity in solid-state. The turn-on time of the OMIEC memristor corresponds to the required time for released neurotransmitters to bind with AMPA receptors in the biological synapse. In previous literature, it has been studied that the turn-on time is related to the average consuming

time for crossing the half of two electrodes [126], [130], [135], [136]. As the variations of the device thickness were minimized during the fabrication process, it is believed that ion conductivity is a dominant factor to characterize the turn-on time of our OMIEC memristors. Figure 52a shows the time-dependent current spectra for measuring the turn-on time of our OMIEC devices by applying a constant voltage of 3.5 V on unbiased devices. All three curves, which demonstrate current increasing from low to the saturated level, were fitted to an exponential equation

Equation 4

$$Y = A_o \exp(-t / \tau_{on}) + Y_o$$

where A_0 and Y_0 are constants, τ_{on} is the turn-on time as illustrated with green fitting curves in Figure 52a. The values of turn-on time are 3.8 s for Device 0, 1.7 s for Device 1, and 640 ms for Device 2. These data indicate that the device with a higher concentration of $LiClO_4$ salt has a short turn-on time due to its high ion conductivity. The values of turn-on time by varying the applied voltage were also measured and illustrated in Figure 53. It demonstrates that the turn-on time decreases with higher biased voltage for all devices.

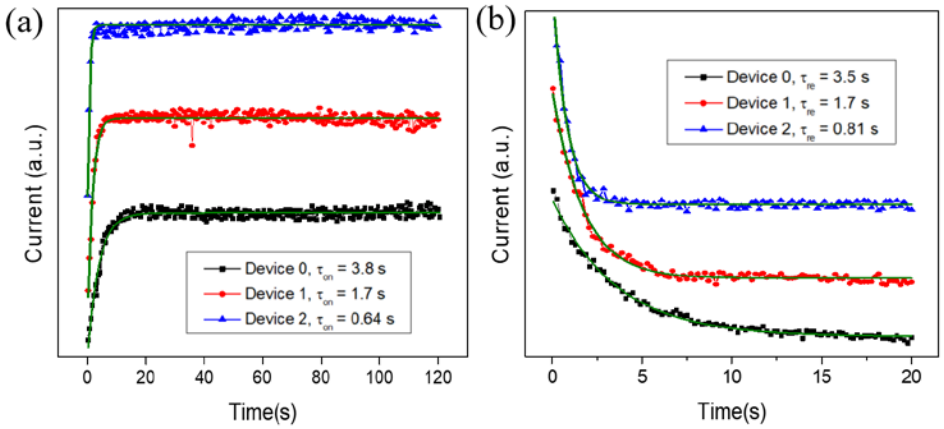

Figure 52. The time-dependent current spectra for (a) turn-on time and (b) relaxation time of Device 0 (black square), Device 1 (red circle), and Device 2 (blue triangle) as indicated. The acquired data of turn-on time and relaxation time were fitted to Eq. 4 and Eq. 5, respectively, as depicted with solid green lines.

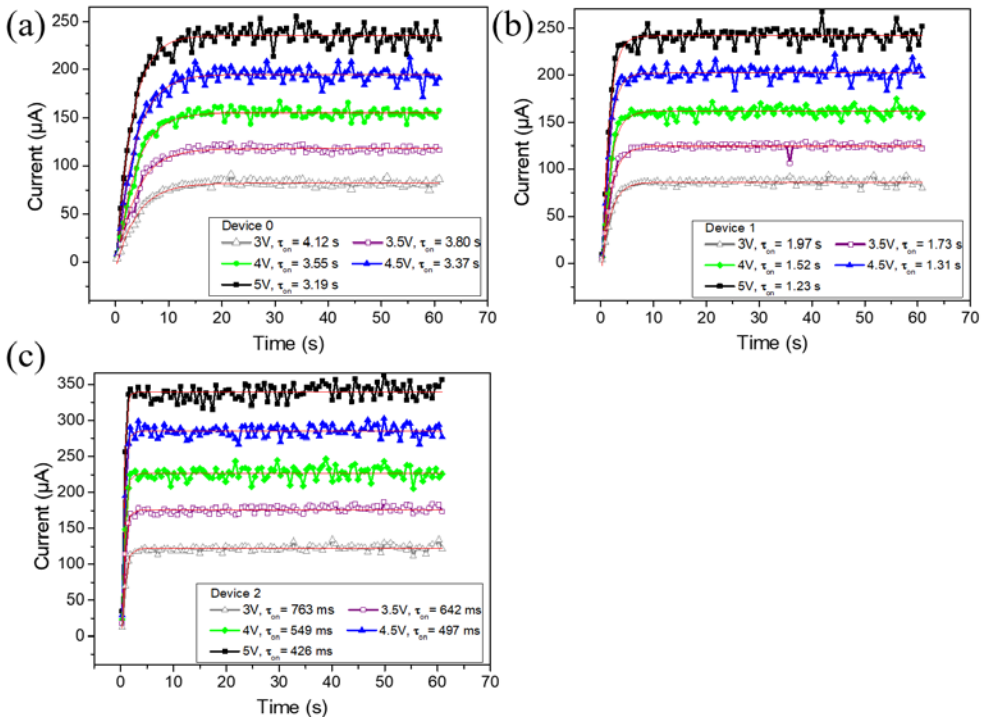

Figure 53. The time-dependent current spectra for turn-on time of (a) Device 0, (b) Device 1, and (c) Device 2 by varying the applied voltage from 3 to 5 V as indicated. The acquired data were fitted to Eq. 4 as illustrated with solid red lines.

On the other hand, relaxation time is defined as the time it takes for ions accumulated on the electrode surfaces to diffuse back to a stable state [137]. The relaxation time of the OMIEC memristor can be assumed to be correlated with the duration time of neurotransmitters to be bound with receptors. Figure 52b shows the time-dependent current spectra to measure the relaxation time of OMIEC devices by applying a read voltage of 1.5 V on the already turned-on devices. Since biased voltage dropped from 3.5 V to 1.5 V, the current level was also decreased and saturated. The curves were fitted to an exponential equation

Equation 5

$$Y = A_o \exp(-t / \tau_{re}) + Y_o$$

A_0 and Y_0 are constants, τ_{re} is the relaxation time as depicted with green fitting curves in Figure 52b. The values of relaxation time are 3.5 s for Device 0, 1.7 s for Device 1, and 810 ms for Device 2. The data indicate that higher ion conductivity causes a faster relaxation time. For the accurate results, measurements of turn-on time and relaxation time were conducted on 10 virgin devices each, described with their average and standard deviation in Table 9 and Table 10, respectively.

Table 9. Measured turn-on time values by conducting on 10 virgin devices and their average, standard deviation.

	1 (s)	2 (s)	3 (s)	4 (s)	5 (s)	6 (s)	7 (s)	8 (s)	9 (s)	10 (s)	Average (s)	Standard deviation (s)
Device 0	3.8	4.1	3.9	4	3.4	3.8	3.7	3.5	3.9	3.8	3.8	0.21
Device 1	1.7	1.3	2	2.2	1.8	1.5	1.7	1.7	1.5	1.9	1.7	0.26
Device 2	0.64	0.49	0.74	0.66	0.71	0.52	0.58	0.62	0.79	0.6	0.64	0.09

Table 10. Measured relaxation time values by conducting on 10 virgin devices and their average, standard deviation.

	1 (s)	2 (s)	3 (s)	4 (s)	5 (s)	6 (s)	7 (s)	8 (s)	9 (s)	10 (s)	Average (s)	Standard deviation (s)
Device 0	3.5	2.8	3.3	4.3	1.0	3.5	2.9	3.2	3.7	3.8	3.5	0.47
Device 1	1.7	1.2	1.7	2.3	1.9	2.6	2.0	1.3	1.1	1.5	1.7	0.48
Device 2	0.81	0.72	0.77	0.80	0.91	0.88	0.87	0.82	0.79	0.75	0.81	0.06

Paired-pulse facilitation. Fig. 54a illustrated the paired-pulse facilitation (PPF) in a biological synapse. PPF is a phenomenon of the synaptic enhancement to the second pulse when two presynaptic spikes closely follow [138]–[141]. For emulating the presynaptic spikes, two 3.5 V pulses (100 ms in duration and 50 ms in interval time) were applied to the OMIEC memristors as depicted in Figure 54b-d.

For all three memristive devices, the current level of the second spike (I_2) is larger than the first one (I_1), where I_1 and I_2 are the average values of measured current data in the range of duration time. Since the duration time of each spike and the interval time between two pulses are shorter than the turn-on time and relaxation time of the devices, respectively, the conductance was enhanced as shown in Fig. 54b-d.

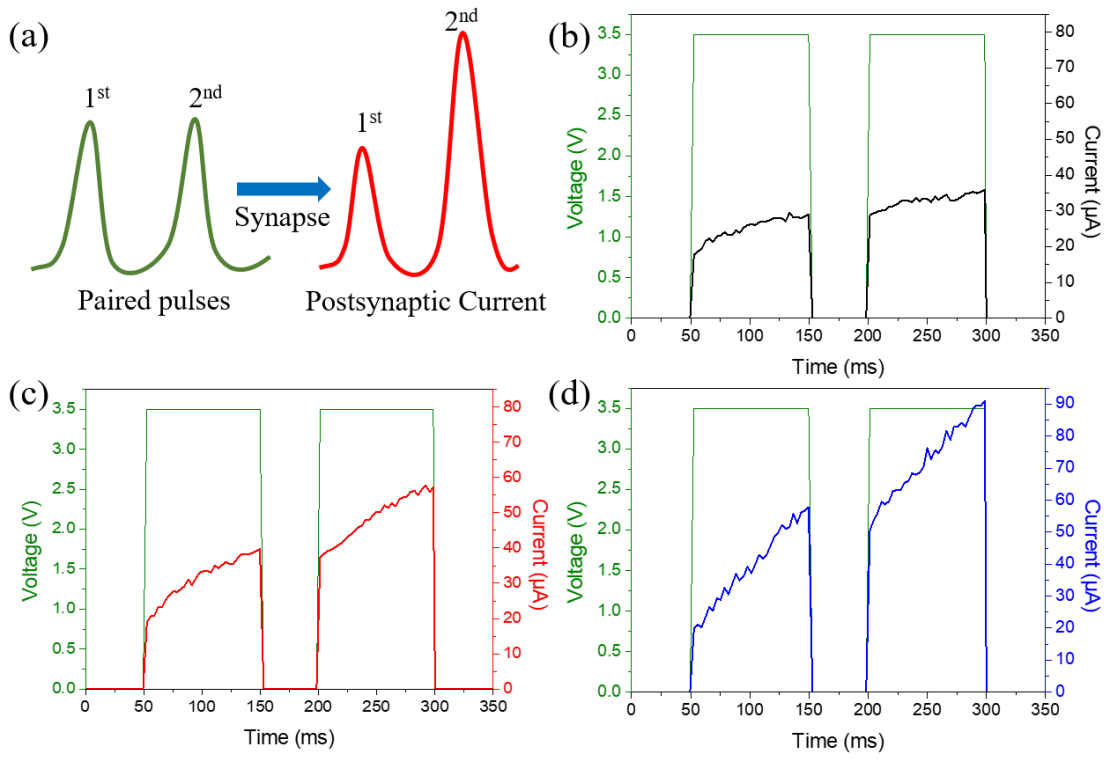

Figure 54. (a) Schematic illustration of PPF phenomenon in a biological synapse between a presynaptic neuron and a postsynaptic neuron. Two 3.5 V applied pulses (100 ms in duration and 50 ms in interval time) and the consequent current are depicted for (b) Device 0, (c) Device 1, and (d) Device 2.

The PPF index is largely affected by the concentration of $LiClO_4$ additive.

Equation 6

$$(I_2 - I_1)/I_1 \times 100\%$$

Their values are 24.2%, 44.4%, and 84.1% for Device 0, Device 1, and Device 2, respectively. These different values of the PPF index can be explained by ion conductivity. Device 2 shows a larger PPF index because the current level increased more than Device 0 or Device 1 during the same 100 ms, which is contributed to its high ion conductivity. Figure 55 presents the PPF data and its statistical distribution as a function

of the interval time. Here, the pulse magnitude and duration were fixed at 3.5 V and 100 ms, respectively, and the pulse interval was increased from 50 ms to 20 s. The relationship between the PPF and interval time was fitted by the equation

Equation 7

$$PPF\ (\%) = C_1 \exp(-t / \tau_1) + C_2 \exp(-t / \tau_2) + C_0$$

are constants and τ_1, τ_2 are PPF relaxation times as shown with the green fitting curves in Figure 55a-c. In our fitting results, τ_1 = 223 ms and τ_2 = 3.28 s for Device 0, τ_1 = 96 ms and τ_2 = 2.14 s for Device 1, τ_1 = 75 ms and τ_2 = 1.07 s for Device 2 were calculated. In the biological synapse, the timescale of two phases (τ_1 and τ_2) are tens of milliseconds and hundreds of milliseconds [142]. Therefore, the fitting results of Device 2 showed closer PPF relaxation time with biological synapses compared to Device 0 or Device 1.

Figure 56 indicates the PPF as a function of pulse magnitude (ranged from 3 to 4.5 V) with fixed 50 ms of interval time and 100 ms of pulse duration time. Also, the pulse duration time (ranged from 50 to 300 ms) dependent PPF data are shown in Figure 57 with fixed 50 ms of interval time and 3.5 V of pulse magnitude. These data demonstrated that the average PPF increases with higher pulse magnitude or longer pulse duration.

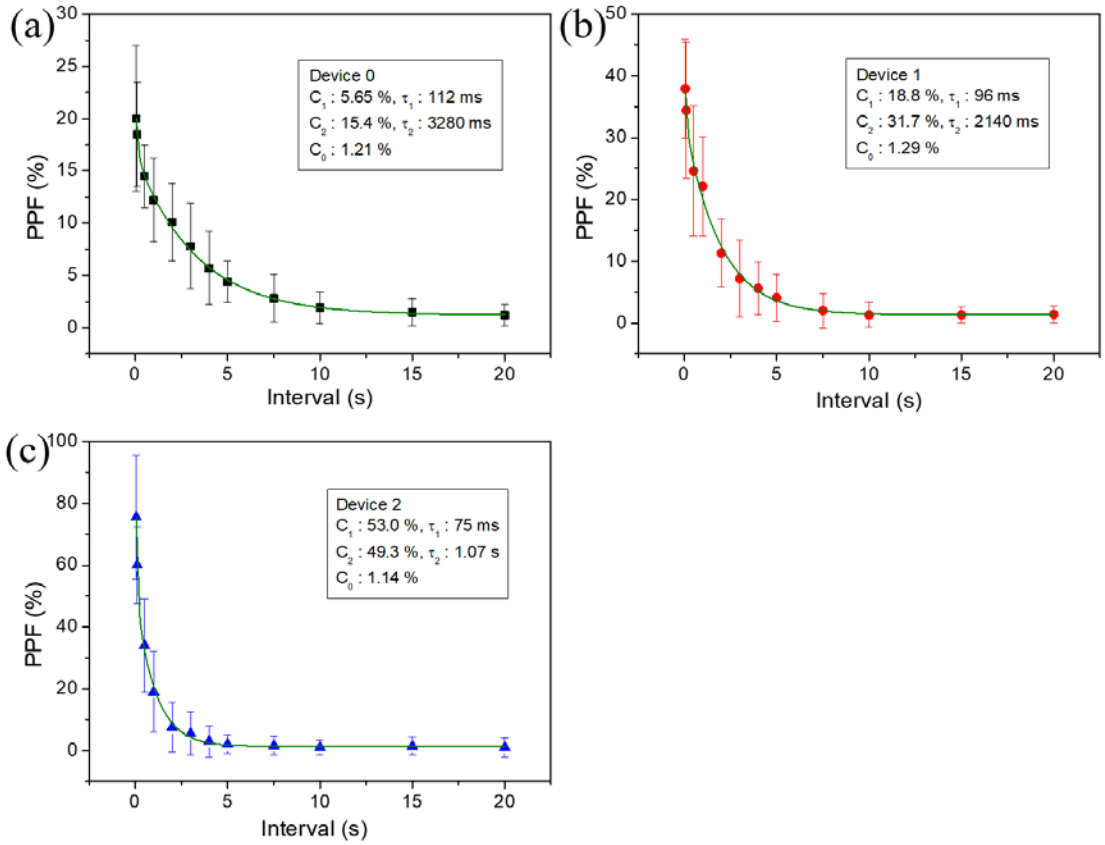

Figure 55. PPF data and its statistical distribution as a function of the pulse interval with fixed pulse magnitude and duration at 3.5 V and 100 ms, respectively, for (a) Device 0 (black square), (b) Device 1 (red circle), and (c) Device 2 (blue triangle). The measured PPF data were fitted with Eq. 7 and illustrated with green curves. The acquired parameters by fitting are demonstrated in the inset of each graph.

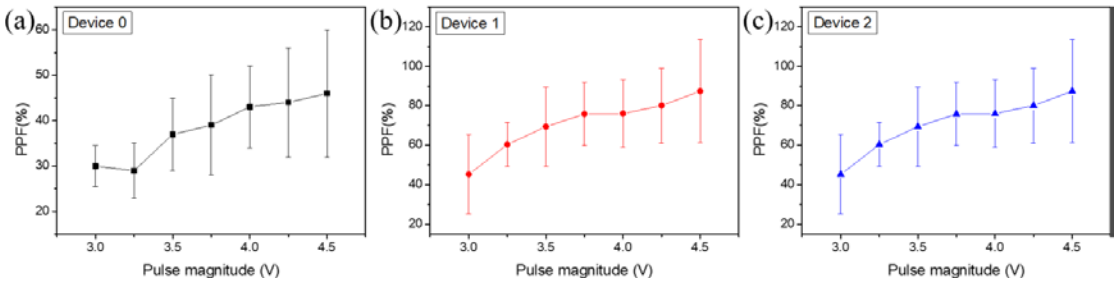

Figure 56. PPF data and its statistical distribution as a function of the pulse magnitude with fixed pulse interval and duration at 50 ms and 100 ms, respectively, for (a) Device 0 (black square), (b) Device 1 (red circle), and (c) Device 2 (blue triangle).

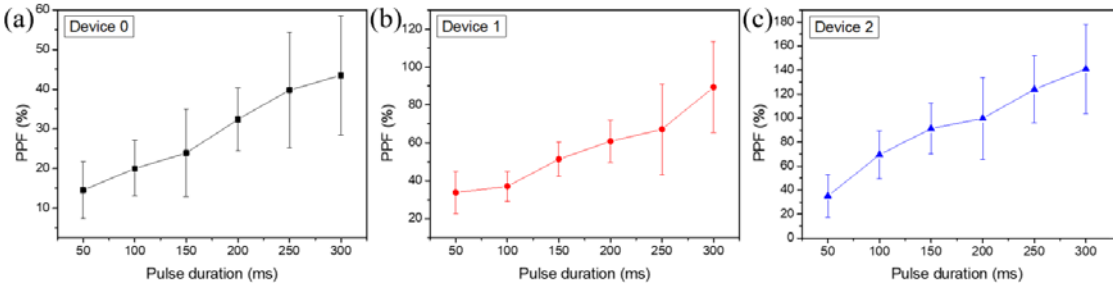

Figure 57. PPF data and its statistical distribution as a function of the pulse duration with fixed pulse interval and magnitude at 50 ms and 3.5 V, respectively, for (a) Device 0 (black square), (b) Device 1 (red circle), and (c) Device 2 (blue triangle).

Short-term synaptic plasticity. Dynamic change of a synapse, which decays back to its normal state within hundreds of milliseconds to a few seconds, is termed short-term synaptic plasticity (STP) in biological synapses [123]. The STP in biology can be measured by activating 4 presynaptic spikes sequentially and a fifth spike after a few seconds, observing the recovery of conductance level. To emulate the STP property, current changes of our OMIEC memristors were measured while 4 + 1 spikes were applied, as depicted in Figure 58.

During the 4 presynaptic spikes (3.5 V of pulse magnitude, 100 ms in duration, and 50 ms in interval time), the current was enhanced following the PPF index, which means the current level of Device 2 increased more than Device 0 or Device 1. After the fourth spike, a read voltage of 1.5 V was applied to the device for measuring the recovery of their initial current level. The decay curves were following the relaxation time, i.e., the pristine device takes a longer time to recover its initial state than the device with a higher concentration of additive salt.

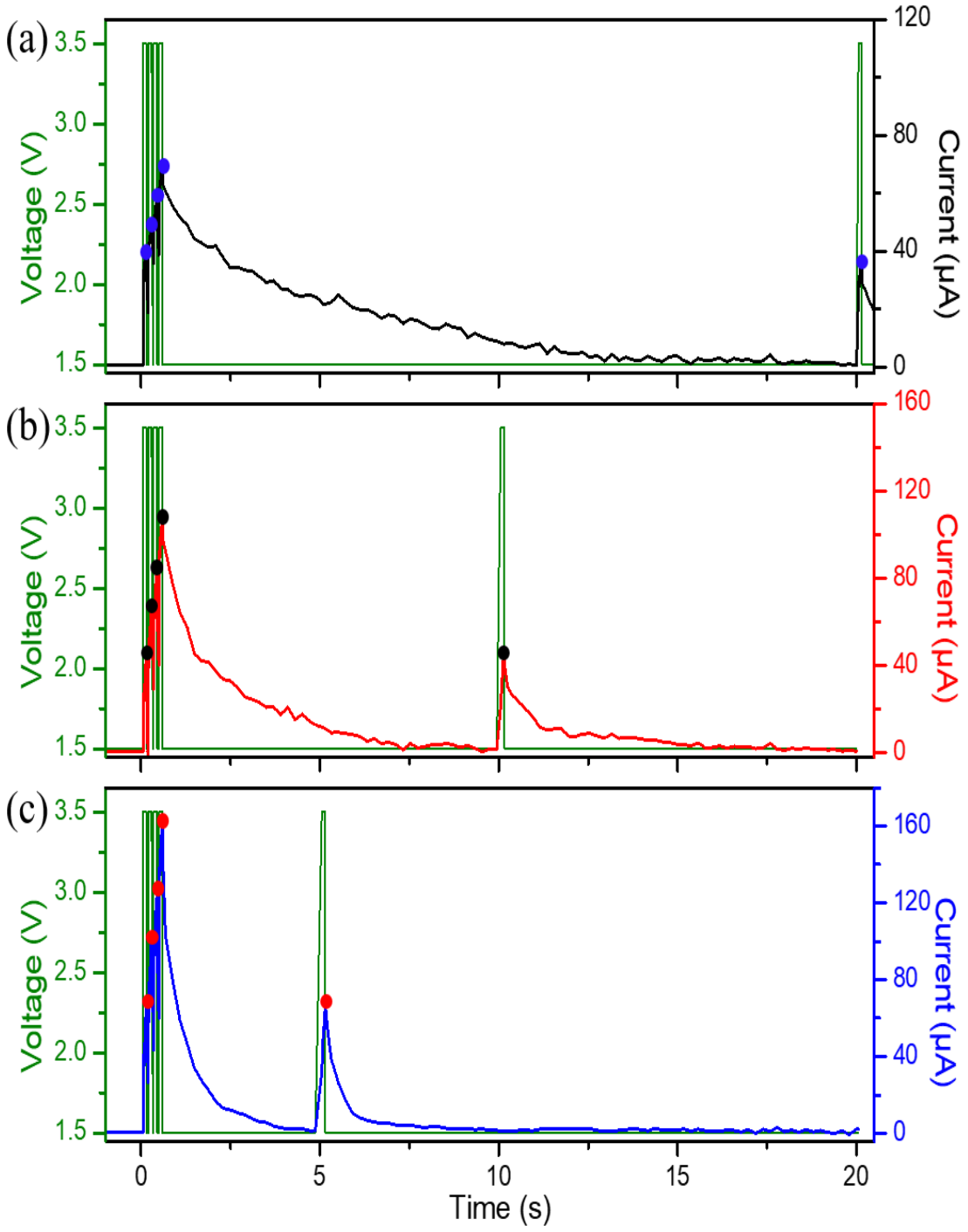

Figure 58. Emulating short-term synaptic plasticity. The current change was measured while 4 + 1 presynaptic spikes were applied on (a) Device 0, (b) Device 1, and (c) Device 2.

Table 11. Device parameters of three OMIEC memristors with varying salt concentrations (Device 0, Device 1, and Device 2).

Device	Active layer	Ion conductivity	Turn-on time	Relaxation time	PPF index	PPF relaxation time		4 + 1 PPF index
		σ ($\times 10^{-11}$ S/cm)	τ_{on} (s)	τ_{re} (s)	(%)	τ_1 (ms)	τ_2 (s)	(%)
Device 0	$Ru(bpy)_3(PF_6)_2$	2.79	3.8	3.5	24.2	112	3.28	1.9
Device 1	$Ru(bpy)_3(PF_6)_2$ + 1 wt % of $LiClO_4$	7.72	1.7	1.7	44.4	96	2.14	1.4
Device 2	$Ru(bpy)_3(PF_6)_2$ + 2 wt % of $LiClO_4$	19.0	0.64	0.81	84.1	75	1.07	2.3

The recovery timescale of Device 2 is similar to that of a biological synapse. The PPF indices between the first and fifth spikes, i.e., $(I_5 - I_1)/I_1 \times 100\%$, are 1.9 % for Device 0, 1.4 % for Device 1, and 2.3 % for Device 2, which indicates the current level of devices were recovered after enough decay time. Therefore, our OMIEC devices can be described as memristors that have STM properties. Furthermore, easily tunable property by adding salt shows the OMIEC memristor's potential as a neuromorphic device for emulating the STP timescale of a biological synapse. All the device parameters of Device 0, Device 1, and Device 2 mentioned above are summarized in Table 11.

4.3. Conclusion

In this chapter, I demonstrated a new memristive device using $Ru(bpy)_3(PF_6)_2$ as an active layer that emulates the short-term characteristics of a biological synapse. Besides, the performances of the memristors can be tunable by adding $LiClO_4$ salt, which affects the ion conductivity of the active layer. EIS was performed to measure the ion conductivities of devices. Also, I-V characteristics, turn-on time, relaxation time, and PPF indices of OMIEC memristors were measured to explain the correlation with biological synaptic properties. Finally, short-term synaptic plasticity was mimicked by applying 4 + 1 spikes and measured current to verify the STM characteristics of our memristive devices. The above data confirmed that Device 2, which consisted of $Ru(bpy)_3(PF_6)_2$ with 2% $LiClO_4$, shows similar timescales to STP characteristics of biological synapses. These results make my OMIEC memristor a good candidate for the neuromorphic device, paving the way to implement electronic synapses in future applications.

5. CONCLUSIONS

In this dissertation, a number of materials, device structures, and techniques were presented for developing deep blue OLED devices, achieving efficient OLEDs through the newly designed host and blocking materials, and emulating short-term plasticity of biological synapse with organic materials.

For the blue emitter of OLEDs, a new platinum complex, PtNONS56-dtb, was designed through the color tuning strategy that controls the energy gap between T_1 and T_2 to achieve deep blue color. Consequently, the new complex showed an emission spectrum at 460 nm with a FWHM of 59 nm at room temperature in PMMA film, which is significantly narrowed and blueshifted compared to the parent structure, PtNON. PtNONS56-dtb in a device achieved a peak EQE of 8.5% with CIE coordinates of (0.14, 0.27). The development of deep blue emitters in OLED devices has remained a challenge for more than a decade. However, the new Pt complex, PTNONS56-dtb, and its color tuning strategy can pave the way to solve the remained challenge.

Advanced OLED devices generally have multilayer structures, and it is crucial to employ appropriate materials for each layer. In this respect, designing host/blocking materials with high triplet energy is meaningful. A newly developed host/charge blocking materials, BCN34 and BCN54, and their performances were presented in detail. BCN34 as an EBL in devices employing Pd3O3 emitter achieved the estimated LT80 of 12509 h at 1000 cd m^{-2} with a peak EQE of 30.3%. Also, a device with bi-layer emissive layer structure, using BCN34 and CBP as host materials doped with PtN3N emitter, achieved a peak EQE of 16.5% with the LT_{97} of 351 h at 1000 cd m^{-2}.

The OMIEC devices that employed $Ru(bpy)_3(PF_6)_2$ with different concentrations of $LiClO_4$ salt demonstrated a similar operational mechanism with biological synapses. Therefore, optimizing the salt concentration was essential for OMIEC devices to have similar timescales to biological synapses. Ultimately, the device with 2% $LiClO_4$ salt shows similar timescales to short-term plasticity characteristics of biological synapses.

All the research in this dissertation will have an impact on the OLED research field, neuromorphic device engineering field, and help to bring these technologies closer to widespread adoption.

REFERENCES

[1] C. W. Tang and S. A. VanSlyke, “Organic electroluminescent diodes,” *Appl. Phys. Lett.*, vol. 51, no. 12, pp. 913–915, Sep. 1987, doi: 10.1063/1.98799.

[2] P. Peumans, S. Uchida, and S. R. Forrest, “Efficient bulk heterojunction photovoltaic cells using small-molecular-weight organic thin films,” in *Materials for Sustainable Energy*, 0 vols., Co-Published with Macmillan Publishers Ltd, UK, 2010, pp. 94–98. doi: 10.1142/9789814317665_0015.

[3] C. Reese, M. Roberts, M. Ling, and Z. Bao, “Organic thin film transistors,” *Mater. Today*, vol. 7, no. 9, pp. 20–27, Sep. 2004, doi: 10.1016/S1369-7021(04)00398-0.

[4] I. Valov and M. Kozicki, “Organic memristors come of age,” *Nat. Mater.*, vol. 16, no. 12, Art. no. 12, Dec. 2017, doi: 10.1038/nmat5014.

[5] U. I. Gaya, *Heterogeneous Photocatalysis Using Inorganic Semiconductor Solids*. Springer Science & Business Media, 2013.

[6] C. Wang, H. Dong, L. Jiang, and W. Hu, “Organic semiconductor crystals,” *Chem. Soc. Rev.*, vol. 47, no. 2, pp. 422–500, Jan. 2018, doi: 10.1039/C7CS00490G.

[7] C.-T. Sah, *Fundamentals of Solid-state Electronics*. World Scientific, 1991.

[8] A. Köhler and H. Bässler, *Electronic Processes in Organic Semiconductors: An Introduction*. John Wiley & Sons, 2015.

[9] D. Schlettwein, “Chapter 3 - Electronic Properties of Molecular Organic Semiconductor Thin Films,” in *Supramolecular Photosensitive and Electroactive Materials*, H. S. Nalwa, Ed. San Diego: Academic Press, 2001, pp. 211–338. doi: 10.1016/B978-012513904-5/50005-3.

[10] V. Coropceanu, J. Cornil, D. A. da Silva Filho, Y. Olivier, R. Silbey, and J.-L. Brédas, “Charge Transport in Organic Semiconductors,” *Chem. Rev.*, vol. 107, no. 4, pp. 926–952, Apr. 2007, doi: 10.1021/cr050140x.

[11] S. R. Forrest, “The path to ubiquitous and low-cost organic electronic appliances on plastic,” *Nature*, vol. 428, no. 6986, pp. 911–918, Apr. 2004, doi: 10.1038/nature02498.

[12] F. So, J. Kido, and P. Burrows, “Organic Light-Emitting Devices for Solid-State Lighting,” *MRS Bull.*, vol. 33, no. 7, pp. 663–669, Jul. 2008, doi: 10.1557/mrs2008.137.

[13] A. Salehi, X. Fu, D.-H. Shin, and F. So, “Recent Advances in OLED Optical Design,” *Adv. Funct. Mater.*, vol. 29, no. 15, p. 1808803, 2019, doi: 10.1002/adfm.201808803.

[14] M. Pope, H. P. Kallmann, and P. Magnante, “Electroluminescence in Organic Crystals,” p. 3.

[15] C. W. Tang, S. A. VanSlyke, and C. H. Chen, “Electroluminescence of doped organic thin films,” *J. Appl. Phys.*, vol. 65, no. 9, pp. 3610–3616, May 1989, doi: 10.1063/1.343409.

[16] M. A. Baldo *et al.*, “Highly efficient phosphorescent emission from organic electroluminescent devices,” *Nature*, vol. 395, no. 6698, p. 151, Sep. 1998, doi: 10.1038/25954.

[17] M. A. Baldo, S. Lamansky, P. E. Burrows, M. E. Thompson, and S. R. Forrest, “Very high-efficiency green organic light-emitting devices based on electrophosphorescence,” *Appl. Phys. Lett.*, vol. 75, no. 1, pp. 4–6, Jun. 1999, doi: 10.1063/1.124258.

[18] H. Uoyama, K. Goushi, K. Shizu, H. Nomura, and C. Adachi, “Highly efficient organic light-emitting diodes from delayed fluorescence,” *Nature*, vol. 492, no. 7428, pp. 234–238, Dec. 2012, doi: 10.1038/nature11687.

[19] H. Nakanotani *et al.*, “High-efficiency organic light-emitting diodes with fluorescent emitters,” *Nat. Commun.*, vol. 5, no. 1, p. 4016, May 2014, doi: 10.1038/ncomms5016.

[20] D. P.-K. Tsang, T. Matsushima, and C. Adachi, “Operational stability enhancement in organic light-emitting diodes with ultrathin Liq interlayers,” *Sci. Rep.*, vol. 6, no. 1, p. 22463, Mar. 2016, doi: 10.1038/srep22463.

[21] C. Mead, “Neuromorphic electronic systems,” *Proc. IEEE*, vol. 78, no. 10, pp. 1629–1636, Oct. 1990, doi: 10.1109/5.58356.

[22] G. Indiveri and S.-C. Liu, “Memory and Information Processing in Neuromorphic Systems,” *Proc. IEEE*, vol. 103, no. 8, pp. 1379–1397, Aug. 2015, doi: 10.1109/JPROC.2015.2444094.

[23] G. E. Moore, “Cramming more components onto integrated circuits,” vol. 38, no. 8, p. 6, 1965.

[24] M. M. Waldrop, “The chips are down for Moore’s law,” *Nat. News*, vol. 530, no. 7589, p. 144, Feb. 2016, doi: 10.1038/530144a.

[25] H. N. Khan, D. A. Hounshell, and E. R. H. Fuchs, “Science and research policy at the end of Moore’s law,” *Nat. Electron.*, vol. 1, no. 1, pp. 14–21, Jan. 2018, doi: 10.1038/s41928-017-0005-9.

[26] J. von Neumann, “First draft of a report on the EDVAC,” *IEEE Ann. Hist. Comput.*, vol. 15, no. 4, pp. 27–75, 1993, doi: 10.1109/85.238389.

[27] “Reflections on the memory wall | Proceedings of the 1st conference on Computing frontiers.” https://dl.acm.org/doi/abs/10.1145/977091.977115 (accessed Jan. 05, 2021).

[28] H. G. Cragon, “Computer Architecture and Implementation,” *Meas. Sci. Technol.*, vol. 12, no. 10, pp. 1744–1745, Sep. 2001, doi: 10.1088/0957-0233/12/10/704.

[29] J. Fan, F. Han, and H. Liu, “Challenges of Big Data analysis,” *Natl. Sci. Rev.*, vol. 1, no. 2, pp. 293–314, Jun. 2014, doi: 10.1093/nsr/nwt032.

[30] Z. Allam and Z. A. Dhunny, “On big data, artificial intelligence and smart cities,” *Cities*, vol. 89, pp. 80–91, Jun. 2019, doi: 10.1016/j.cities.2019.01.032.

[31] R. A. Nawrocki, R. M. Voyles, and S. E. Shaheen, “A Mini Review of Neuromorphic Architectures and Implementations,” *IEEE Trans. Electron Devices*, vol. 63, no. 10, pp. 3819–3829, Oct. 2016, doi: 10.1109/TED.2016.2598413.

[32] L. F. Abbott and W. G. Regehr, “Synaptic computation,” *Nature*, vol. 431, no. 7010, Art. no. 7010, Oct. 2004, doi: 10.1038/nature03010.

[33] R. Sarpeshkar, “Analog Versus Digital: Extrapolating from Electronics to

Neurobiology," *Neural Comput.*, vol. 10, no. 7, pp. 1601–1638, Oct. 1998, doi: 10.1162/089976698300017052.

[34] G. Indiveri *et al.*, "Neuromorphic Silicon Neuron Circuits," *Front. Neurosci.*, vol. 5, 2011, doi: 10.3389/fnins.2011.00073.

[35] A. R. Young, M. E. Dean, J. S. Plank, and G. S. Rose, "A Review of Spiking Neuromorphic Hardware Communication Systems," *IEEE Access*, vol. 7, pp. 135606–135620, 2019, doi: 10.1109/ACCESS.2019.2941772.

[36] B. V. Benjamin *et al.*, "Neurogrid: A Mixed-Analog-Digital Multichip System for Large-Scale Neural Simulations," *Proc. IEEE*, vol. 102, no. 5, pp. 699–716, May 2014, doi: 10.1109/JPROC.2014.2313565.

[37] K. Meier, "A mixed-signal universal neuromorphic computing system," in *2015 IEEE International Electron Devices Meeting (IEDM)*, Dec. 2015, p. 4.6.1-4.6.4. doi: 10.1109/IEDM.2015.7409627.

[38] "TrueNorth: Design and Tool Flow of a 65 mW 1 Million Neuron Programmable Neurosynaptic Chip - IEEE Journals & Magazine." https://ieeexplore.ieee.org/abstract/document/7229264 (accessed Jan. 15, 2021).

[39] S. B. Furber, F. Galluppi, S. Temple, and L. A. Plana, "The SpiNNaker Project," *Proc. IEEE*, vol. 102, no. 5, pp. 652–665, May 2014, doi: 10.1109/JPROC.2014.2304638.

[40] M. Davies *et al.*, "Loihi: A Neuromorphic Manycore Processor with On-Chip Learning," *IEEE Micro*, vol. 38, no. 1, pp. 82–99, Jan. 2018, doi: 10.1109/MM.2018.112130359.

[41] "RRAM-based synapse for neuromorphic system with pattern recognition function - IEEE Conference Publication." https://ieeexplore.ieee.org/document/6479016 (accessed Jan. 15, 2021).

[42] D. S. Jeong, "Hardware Spiking Artificial Neurons, Their Response Function, and Noises," in *Advances in Neuromorphic Hardware Exploiting Emerging Nanoscale Devices*, M. Suri, Ed. New Delhi: Springer India, 2017, pp. 1–16. doi: 10.1007/978-81-322-3703-7_1.

[43] L. Chua, "Memristor-The missing circuit element," *IEEE Trans. Circuit Theory*,

vol. 18, no. 5, pp. 507–519, Sep. 1971, doi: 10.1109/TCT.1971.1083337.

[44] J. J. Yang, D. B. Strukov, and D. R. Stewart, “Memristive devices for computing,” *Nat. Nanotechnol.*, vol. 8, no. 1, Art. no. 1, Jan. 2013, doi: 10.1038/nnano.2012.240.

[45] R. Waser and M. Aono, “Nanoionics-based resistive switching memories,” in *Nanoscience and Technology*, 0 vols., Co-Published with Macmillan Publishers Ltd, UK, 2009, pp. 158–165. doi: 10.1142/9789814287005_0016.

[46] L. Chua, “If it’s pinched it’s a memristor,” *Semicond. Sci. Technol.*, vol. 29, no. 10, p. 104001, Sep. 2014, doi: 10.1088/0268-1242/29/10/104001.

[47] D. B. Strukov, G. S. Snider, D. R. Stewart, and R. S. Williams, “The missing memristor found,” *Nature*, vol. 453, no. 7191, Art. no. 7191, May 2008, doi: 10.1038/nature06932.

[48] L. Xiao *et al.*, “Recent Progresses on Materials for Electrophosphorescent Organic Light-Emitting Devices,” *Adv. Mater.*, vol. 23, no. 8, pp. 926–952, 2011, doi: 10.1002/adma.201003128.

[49] M. A. Baldo, D. F. O’Brien, M. E. Thompson, and S. R. Forrest, “Excitonic singlet-triplet ratio in a semiconducting organic thin film,” *Phys. Rev. B*, vol. 60, no. 20, pp. 14422–14428, Nov. 1999, doi: 10.1103/PhysRevB.60.14422.

[50] C. Adachi, M. A. Baldo, M. E. Thompson, and S. R. Forrest, “Nearly 100% internal phosphorescence efficiency in an organic light-emitting device,” *J. Appl. Phys.*, vol. 90, no. 10, pp. 5048–5051, Oct. 2001, doi: 10.1063/1.1409582.

[51] T. Fleetham, L. Huang, and J. Li, “Tetradentate Platinum Complexes for Efficient and Stable Excimer-Based White OLEDs,” *Adv. Funct. Mater.*, vol. 24, no. 38, pp. 6066–6073, 2014, doi: 10.1002/adfm.201401244.

[52] S.-Y. Kim *et al.*, “Organic Light-Emitting Diodes with 30% External Quantum Efficiency Based on a Horizontally Oriented Emitter,” *Adv. Funct. Mater.*, vol. 23, no. 31, pp. 3896–3900, 2013, doi: 10.1002/adfm.201300104.

[53] T. Fleetham, G. Li, and J. Li, “Efficient Red-Emitting Platinum Complex with Long Operational Stability,” *ACS Appl. Mater. Interfaces*, vol. 7, no. 30, pp. 16240–16246, Aug. 2015, doi: 10.1021/acsami.5b01596.

[54] “Low-Driving-Voltage Blue Phosphorescent Organic Light-Emitting Devices with External Quantum Efficiency of 30% - Udagawa - 2014 - Advanced Materials - Wiley Online Library.” https://onlinelibrary.wiley.com/doi/full/10.1002/adma.201401621 (accessed Mar. 14, 2020).

[55] S. Lamansky *et al.*, “Synthesis and Characterization of Phosphorescent Cyclometalated Iridium Complexes,” *Inorg. Chem.*, vol. 40, no. 7, pp. 1704–1711, Mar. 2001, doi: 10.1021/ic0008969.

[56] T. B. Fleetham, L. Huang, K. Klimes, J. Brooks, and J. Li, “Tetradentate Pt(II) Complexes with 6-Membered Chelate Rings: A New Route for Stable and Efficient Blue Organic Light Emitting Diodes,” *Chem. Mater.*, vol. 28, no. 10, pp. 3276–3282, May 2016, doi: 10.1021/acs.chemmater.5b04957.

[57] T. Fleetham, G. Li, L. Wen, and J. Li, “Efficient ‘Pure’ Blue OLEDs Employing Tetradentate Pt Complexes with a Narrow Spectral Bandwidth,” *Adv. Mater.*, vol. 26, no. 41, pp. 7116–7121, 2014, doi: 10.1002/adma.201401759.

[58] S. Haneder *et al.*, “Controlling the Radiative Rate of Deep-Blue Electrophosphorescent Organometallic Complexes by Singlet-Triplet Gap Engineering,” *Adv. Mater.*, vol. 20, no. 17, pp. 3325–3330, 2008, doi: 10.1002/adma.200800630.

[59] G. Li, A. Wolfe, J. Brooks, Z.-Q. Zhu, and J. Li, “Modifying Emission Spectral Bandwidth of Phosphorescent Platinum(II) Complexes Through Synthetic Control,” *Inorg. Chem.*, vol. 56, no. 14, pp. 8244–8256, Jul. 2017, doi: 10.1021/acs.inorgchem.7b00961.

[60] K. Klimes, Z.-Q. Zhu, and J. Li, “Efficient Blue Phosphorescent OLEDs with Improved Stability and Color Purity through Judicious Triplet Exciton Management,” *Adv. Funct. Mater.*, vol. 29, no. 31, p. 1903068, 2019, doi: 10.1002/adfm.201903068.

[61] T. Suzuki *et al.*, “Highly efficient long-life blue fluorescent organic light-emitting diode exhibiting triplet–triplet annihilation effects enhanced by a novel hole-transporting material,” *Jpn. J. Appl. Phys.*, vol. 53, no. 5, p. 052102, Apr. 2014, doi: 10.7567/JJAP.53.052102.

[62] C.-F. Chang *et al.*, “Highly Efficient Blue-Emitting Iridium(III) Carbene Complexes and Phosphorescent OLEDs,” *Angew. Chem. Int. Ed.*, vol. 47, no. 24, pp.

4542–4545, 2008, doi: 10.1002/anie.200800748.

[63] “Bis-Tridentate Ir(III) Metal Phosphors for Efficient Deep-Blue Organic Light-Emitting Diodes - Kuo - 2017 - Advanced Materials - Wiley Online Library.” https://onlinelibrary.wiley.com/doi/full/10.1002/adma.201702464 (accessed Mar. 21, 2020).

[64] R. C. Kwong *et al.*, “High operational stability of electrophosphorescent devices,” *Appl. Phys. Lett.*, vol. 81, no. 1, pp. 162–164, Jun. 2002, doi: 10.1063/1.1489503.

[65] J. Brooks *et al.*, “Synthesis and Characterization of Phosphorescent Cyclometalated Platinum Complexes,” *Inorg. Chem.*, vol. 41, no. 12, pp. 3055–3066, Jun. 2002, doi: 10.1021/ic0255508.

[66] R. J. Holmes, B. W. D’Andrade, S. R. Forrest, X. Ren, J. Li, and M. E. Thompson, “Efficient, deep-blue organic electrophosphorescence by guest charge trapping,” *Appl. Phys. Lett.*, vol. 83, no. 18, pp. 3818–3820, Oct. 2003, doi: 10.1063/1.1624639.

[67] S. Develay, O. Blackburn, A. L. Thompson, and J. A. G. Williams, “Cyclometalated Platinum(II) Complexes of Pyrazole-Based, NΛCΛN-Coordinating, Terdentate Ligands: the Contrasting Influence of Pyrazolyl and Pyridyl Rings on Luminescence,” *Inorg. Chem.*, vol. 47, no. 23, pp. 11129–11142, Dec. 2008, doi: 10.1021/ic8014157.

[68] P. Kiprof, J. C. Carlson, D. R. Anderson, and V. N. Nemykin, “Systematic color tuning of a family of luminescent azole -based organoboron compounds suitable for OLED applications,” *Dalton Trans.*, vol. 42, no. 42, pp. 15120–15132, 2013, doi: 10.1039/C3DT51853A.

[69] K. Li *et al.*, “Light-emitting platinum(ii) complexes supported by tetradentate dianionic bis(N -heterocyclic carbene) ligands : towards robust blue electrophosphors,” *Chem. Sci.*, vol. 4, no. 6, pp. 2630–2644, 2013, doi: 10.1039/C3SC21822H.

[70] A. B. Tamayo *et al.*, “Synthesis and Characterization of Facial and Meridional Tris-cyclometalated Iridium(III) Complexes,” *J. Am. Chem. Soc.*, vol. 125, no. 24, pp. 7377–7387, Jun. 2003, doi: 10.1021/ja034537z.

[71] “Synthetic Control of Excited-State Properties in Cyclometalated Ir(III)

Complexes Using Ancillary Ligands | Inorganic Chemistry.” https://pubs.acs.org/doi/abs/10.1021/ic048599h (accessed Jul. 04, 2020).

[72] “Cyclometalated Platinum Complexes with Luminescent Quantum Yields Approaching 100% | Inorganic Chemistry.” https://pubs.acs.org/doi/abs/10.1021/ic302490c (accessed Mar. 12, 2020).

[73] G. Li *et al.*, “Novel Carbazole/Fluorene-Based Host Material for Stable and Efficient Phosphorescent OLEDs,” *ACS Appl. Mater. Interfaces*, vol. 11, no. 43, pp. 40320–40331, Oct. 2019, doi: 10.1021/acsami.9b13245.

[74] P.-I. Kvam, M. V. Puzyk, K. P. Balashev, and J. Songstad, “Spectroscopic and Electrochemical Properties of Some Mixed-Ligand Cyclometalated Platinum(II) Complexes Derived from 2-Phenylpyridine,” *Acta Chem. Scand.*, vol. 49, pp. 335–343, 1995.

[75] Z. Wang, E. Turner, V. Mahoney, S. Madakuni, T. Groy, and J. Li, “Facile Synthesis and Characterization of Phosphorescent Pt(N^C^N)X Complexes,” *Inorg. Chem.*, vol. 49, no. 24, pp. 11276–11286, Dec. 2010, doi: 10.1021/ic100740e.

[76] B. W. D’Andrade, S. Datta, S. R. Forrest, P. Djurovich, E. Polikarpov, and M. E. Thompson, “Relationship between the ionization and oxidation potentials of molecular organic semiconductors,” *Org. Electron.*, vol. 6, no. 1, pp. 11–20, Feb. 2005, doi: 10.1016/j.orgel.2005.01.002.

[77] P. I. Djurovich, E. I. Mayo, S. R. Forrest, and M. E. Thompson, “Measurement of the lowest unoccupied molecular orbital energies of molecular organic semiconductors,” *Org. Electron.*, vol. 10, no. 3, pp. 515–520, May 2009, doi: 10.1016/j.orgel.2008.12.011.

[78] M. G. Colombo, T. C. Brunold, T. Riedener, H. U. Guedel, M. Fortsch, and H.-B. Buergi, “Facial tris cyclometalated rhodium(3+) and iridium(3+) complexes: their synthesis, structure, and optical spectroscopic properties,” *Inorg. Chem.*, vol. 33, no. 3, pp. 545–550, Feb. 1994, doi: 10.1021/ic00081a024.

[79] F. O. Garces, K. A. King, and R. J. Watts, “Synthesis, structure, electrochemistry, and photophysics of methyl-substituted phenylpyridine ortho-metalated iridium(III) complexes,” *Inorg. Chem.*, vol. 27, no. 20, pp. 3464–3471, Oct. 1988, doi: 10.1021/ic00293a008.

[80] Md. K. Nazeeruddin, R. Humphry-Baker, D. Berner, S. Rivier, L. Zuppiroli, and

M. Graetzel, “Highly Phosphorescence Iridium Complexes and Their Application in Organic Light-Emitting Devices,” *J. Am. Chem. Soc.*, vol. 125, no. 29, pp. 8790–8797, Jul. 2003, doi: 10.1021/ja021413y.

[81] J. Li *et al.*, “Synthetic Control of Excited-State Properties in Cyclometalated Ir(III) Complexes Using Ancillary Ligands,” *Inorg. Chem.*, vol. 44, no. 6, pp. 1713–1727, Mar. 2005, doi: 10.1021/ic048599h.

[82] K. P. Balashev, M. V. Puzyk, V. S. Kotlyar, and M. V. Kulikova, “Photophysics, photochemistry and electrochemistry of mixed-ligand platinum(II) complexes with 2-phenylpyridine and 2-(2′-thienyl)pyridine as cyclometalating ligands,” *Coord. Chem. Rev.*, vol. 159, pp. 109–120, Mar. 1997, doi: 10.1016/S0010-8545(96)01300-8.

[83] A. Rodrigue-Witchel *et al.*, “Pressure-induced variations of MLCT and ligand-centered luminescence spectra in square-planar platinum(II) complexes,” *Polyhedron*, vol. 108, pp. 151–155, Mar. 2016, doi: 10.1016/j.poly.2015.12.011.

[84] A. Aliprandi, D. Genovese, M. Mauro, and L. De Cola, “Recent Advances in Phosphorescent Pt(II) Complexes Featuring Metallophilic Interactions: Properties and Applications,” *Chem. Lett.*, vol. 44, no. 9, pp. 1152–1169, Jul. 2015, doi: 10.1246/cl.150592.

[85] “Phosphorescent Pt(II) and Pd(II) Complexes for Efficient, High-Color-Quality, and Stable OLEDs - Fleetham - 2017 - Advanced Materials - Wiley Online Library.” https://onlinelibrary.wiley.com/doi/full/10.1002/adma.201601861 (accessed Oct. 21, 2019).

[86] “Nearly 100% Internal Quantum Efficiency in an Organic Blue-Light Electrophosphorescent Device Using a Weak Electron Transporting Material with a Wide Energy Gap - Xiao - 2009 - Advanced Materials - Wiley Online Library.” https://onlinelibrary.wiley.com/doi/abs/10.1002/adma.200802034 (accessed Mar. 13, 2020).

[87] G. Li, J. Ecton, B. O′Brien, and J. Li, “Efficient and stable red organic light emitting devices from a tetradentate cyclometalated platinum complex,” *Org. Electron.*, vol. 15, no. 8, pp. 1862–1867, Aug. 2014, doi: 10.1016/j.orgel.2014.04.020.

[88] N. Chopra, J. S. Swensen, E. Polikarpov, L. Cosimbescu, F. So, and A. B. Padmaperuma, “High efficiency and low roll-off blue phosphorescent organic light-emitting devices using mixed host architecture,” *Appl. Phys. Lett.*, vol. 97, no. 3, p.

033304, Jul. 2010, doi: 10.1063/1.3464969.

[89] K. Togashi, S. Nomura, N. Yokoyama, T. Yasuda, and C. Adachi, “Low driving voltage characteristics of triphenylene derivatives as electron transport materials in organic light-emitting diodes,” *J. Mater. Chem.*, vol. 22, no. 38, pp. 20689–20695, 2012, doi: 10.1039/C2JM33669C.

[90] C.-H. Shih, P. Rajamalli, C.-A. Wu, W.-T. Hsieh, and C.-H. Cheng, “A Universal Electron-Transporting/Exciton-Blocking Material for Blue, Green, and Red Phosphorescent Organic Light-Emitting Diodes (OLEDs),” *ACS Appl. Mater. Interfaces*, vol. 7, no. 19, pp. 10466–10474, May 2015, doi: 10.1021/acsami.5b01872.

[91] A. Tomkeviciene *et al.*, “Impact of Linking Topology on the Properties of Carbazole Trimers and Dimers,” *J. Phys. Chem. C*, vol. 115, no. 11, pp. 4887–4897, Mar. 2011, doi: 10.1021/jp111333v.

[92] J. Zhuang, W. Su, W. Li, Y. Zhou, Q. Shen, and M. Zhou, “Configuration effect of novel bipolar triazole/carbazole-based host materials on the performance of phosphorescent OLED devices,” *Org. Electron.*, vol. 13, no. 10, pp. 2210–2219, Oct. 2012, doi: 10.1016/j.orgel.2012.06.025.

[93] M. Tanaka, R. Nagata, H. Nakanotani, and C. Adachi, “Understanding degradation of organic light-emitting diodes from magnetic field effects,” *Commun. Mater.*, vol. 1, no. 1, Art. no. 1, Apr. 2020, doi: 10.1038/s43246-020-0019-0.

[94] R. Coehoorn, P. A. Bobbert, and H. van Eersel, “F\"orster-type triplet-polaron quenching in disordered organic semiconductors,” *Phys. Rev. B*, vol. 96, no. 18, p. 184203, Nov. 2017, doi: 10.1103/PhysRevB.96.184203.

[95] X. Yang, G. Zhou, and W.-Y. Wong, “Functionalization of phosphorescent emitters and their host materials by main-group elements for phosphorescent organic light-emitting devices,” *Chem. Soc. Rev.*, vol. 44, no. 23, pp. 8484–8575, 2015, doi: 10.1039/C5CS00424A.

[96] Y. Sun, N. C. Giebink, H. Kanno, B. Ma, M. E. Thompson, and S. R. Forrest, “Management of singlet and triplet excitons for efficient white organic light-emitting devices,” *Nature*, vol. 440, no. 7086, Art. no. 7086, Apr. 2006, doi: 10.1038/nature04645.

[97] S.-J. Yoo, H.-J. Yun, I. Kang, K. Thangaraju, S.-K. Kwon, and Y.-H. Kim, “A

new electron transporting material for effective hole-blocking and improved charge balance in highly efficient phosphorescent organic light emitting diodes," *J. Mater. Chem. C*, vol. 1, no. 11, pp. 2217–2223, 2013, doi: 10.1039/C3TC00801K.

[98] B. Ma, B. J. Kim, D. A. Poulsen, S. J. Pastine, and J. M. J. Fréchet, "Multifunctional Crosslinkable Iridium Complexes as Hole Transporting/Electron Blocking and Emitting Materials for Solution-Processed Multilayer Organic Light-Emitting Diodes," *Adv. Funct. Mater.*, vol. 19, no. 7, pp. 1024–1031, 2009, doi: https://doi.org/10.1002/adfm.200801071.

[99] Z.-Q. Zhu, K. Klimes, S. Holloway, and J. Li, "Efficient Cyclometalated Platinum(II) Complex with Superior Operational Stability," *Adv. Mater.*, vol. 29, no. 6, p. 1605002, 2017, doi: 10.1002/adma.201605002.

[100] H. Nakanotani, K. Masui, J. Nishide, T. Shibata, and C. Adachi, "Promising operational stability of high-efficiency organic light-emitting diodes based on thermally activated delayed fluorescence," *Sci. Rep.*, vol. 3, no. 1, Art. no. 1, Jul. 2013, doi: 10.1038/srep02127.

[101] R. J. Holmes *et al.*, "Blue organic electrophosphorescence using exothermic host–guest energy transfer," *Appl. Phys. Lett.*, vol. 82, no. 15, pp. 2422–2424, Apr. 2003, doi: 10.1063/1.1568146.

[102] Y. Sun and S. R. Forrest, "High-efficiency white organic light emitting devices with three separate phosphorescent emission layers," *Appl Phys Lett*, p. 4.

[103] C.-H. Wu, P.-I. Shih, C.-F. Shu, and Y. Chi, "Highly efficient red organic light-emitting devices based on a fluorene-triphenylamine host doped with an Os(II) phosphor," *Appl. Phys. Lett.*, vol. 92, no. 23, p. 233303, Jun. 2008, doi: 10.1063/1.2943155.

[104] C. Fan *et al.*, "Diarylmethylene-bridged triphenylamine derivatives encapsulated with fluorene : very high T g host materials for efficient blue and green phosphorescent OLEDs," *J. Mater. Chem.*, vol. 20, no. 16, pp. 3232–3237, 2010, doi: 10.1039/B927576B.

[105] T. Fleetham, Y. Ji, L. Huang, T. S. Fleetham, and J. Li, "Efficient and stable single-doped white OLEDs using a palladium-based phosphorescent excimer," *Chem. Sci.*, vol. 8, no. 12, pp. 7983–7990, 2017, doi: 10.1039/C7SC02512B.

[106] S. H. Jo, T. Chang, I. Ebong, B. B. Bhadviya, P. Mazumder, and W. Lu,

"Nanoscale Memristor Device as Synapse in Neuromorphic Systems," *Nano Lett.*, vol. 10, no. 4, pp. 1297–1301, Apr. 2010, doi: 10.1021/nl904092h.

[107] K. Kim *et al.*, "Enhanced analog synaptic behavior of SiN x /a-Si bilayer memristors through Ge implantation," *NPG Asia Mater.*, vol. 12, no. 1, Art. no. 1, Dec. 2020, doi: 10.1038/s41427-020-00261-0.

[108] Z. Wang *et al.*, "Engineering incremental resistive switching in TaOx based memristors for brain-inspired computing," *Nanoscale*, vol. 8, no. 29, pp. 14015–14022, Jul. 2016, doi: 10.1039/C6NR00476H.

[109] W. Banerjee, Q. Liu, H. Lv, S. Long, and M. Liu, "Electronic imitation of behavioral and psychological synaptic activities using TiOx/Al2O3-based memristor devices," *Nanoscale*, vol. 9, no. 38, pp. 14442–14450, Oct. 2017, doi: 10.1039/C7NR04741J.

[110] S. Yu, Y. Wu, R. Jeyasingh, D. Kuzum, and H.-S. P. Wong, "An Electronic Synapse Device Based on Metal Oxide Resistive Switching Memory for Neuromorphic Computation," *IEEE Trans. Electron Devices*, vol. 58, no. 8, pp. 2729–2737, Aug. 2011, doi: 10.1109/TED.2011.2147791.

[111] R. Berdan, E. Vasilaki, A. Khiat, G. Indiveri, A. Serb, and T. Prodromakis, "Emulating short-term synaptic dynamics with memristive devices," *Sci. Rep.*, vol. 6, Jan. 2016, doi: 10.1038/srep18639.

[112] C. Du, F. Cai, M. A. Zidan, W. Ma, S. H. Lee, and W. D. Lu, "Reservoir computing using dynamic memristors for temporal information processing," *Nat. Commun.*, vol. 8, no. 1, Art. no. 1, Dec. 2017, doi: 10.1038/s41467-017-02337-y.

[113] G. Srinivasan, A. Sengupta, and K. Roy, "Magnetic Tunnel Junction Based Long-Term Short-Term Stochastic Synapse for a Spiking Neural Network with On-Chip STDP Learning," *Sci. Rep.*, vol. 6, no. 1, Art. no. 1, Jul. 2016, doi: 10.1038/srep29545.

[114] Z. Wang *et al.*, "Memristors with diffusive dynamics as synaptic emulators for neuromorphic computing," *Nat. Mater.*, vol. 16, no. 1, pp. 101–108, Jan. 2017, doi: 10.1038/nmat4756.

[115] Y. Sun *et al.*, "Short-Term and Long-Term Plasticity Mimicked in Low-Voltage Ag/GeSe/TiN Electronic Synapse," *IEEE Electron Device Lett.*, vol. 39, no. 4, pp. 492–495, Apr. 2018, doi: 10.1109/LED.2018.2809784.

[116] B. D. Paulsen, K. Tybrandt, E. Stavrinidou, and J. Rivnay, “Organic mixed ionic–electronic conductors,” *Nat. Mater.*, vol. 19, no. 1, Art. no. 1, Jan. 2020, doi: 10.1038/s41563-019-0435-z.

[117] D. Moia *et al.*, “Design and evaluation of conjugated polymers with polar side chains as electrode materials for electrochemical energy storage in aqueous electrolytes,” *Energy Environ. Sci.*, vol. 12, no. 4, pp. 1349–1357, 2019, doi: 10.1039/C8EE03518K.

[118] Y. Cao, G. Yu, A. J. Heeger, and C. Y. Yang, “Efficient, fast response light-emitting electrochemical cells: Electroluminescent and solid electrolyte polymers with interpenetrating network morphology,” *Appl. Phys. Lett.*, vol. 68, no. 23, pp. 3218–3220, Jun. 1996, doi: 10.1063/1.116442.

[119] S. Inal *et al.*, “A High Transconductance Accumulation Mode Electrochemical Transistor,” *Adv. Mater.*, vol. 26, no. 44, pp. 7450–7455, 2014, doi: https://doi.org/10.1002/adma.201403150.

[120] J. Jang, J. Ha, and J. Cho, “Fabrication of Water-Dispersible Polyaniline-Poly(4-styrenesulfonate) Nanoparticles For Inkjet-Printed Chemical-Sensor Applications,” *Adv. Mater.*, vol. 19, no. 13, pp. 1772–1775, 2007, doi: https://doi.org/10.1002/adma.200602127.

[121] C.-C. Shih, C.-W. Huang, M. Gao, C.-C. Chueh, and W.-C. Chen, “Multi-state memristive behavior in a light-emitting electrochemical cell,” *J. Mater. Chem. C*, vol. 5, no. 44, pp. 11421–11428, 2017, doi: 10.1039/C7TC03920D.

[122] Y. van de Burgt *et al.*, “A non-volatile organic electrochemical device as a low-voltage artificial synapse for neuromorphic computing,” *Nat. Mater.*, vol. 16, no. 4, Art. no. 4, Apr. 2017, doi: 10.1038/nmat4856.

[123] W. Gerstner, W. M. Kistler, R. Naud, and L. Paninski, *Neuronal Dynamics: From Single Neurons to Networks and Models of Cognition*. Cambridge University Press, 2014.

[124] R. D. Costa, E. Ortí, H. J. Bolink, F. Monti, G. Accorsi, and N. Armaroli, “Luminescent Ionic Transition-Metal Complexes for Light-Emitting Electrochemical Cells,” *Angew. Chem. Int. Ed.*, vol. 51, no. 33, pp. 8178–8211, 2012, doi: https://doi.org/10.1002/anie.201201471.

[125] M. Bear, B. Connors, and M. A. Paradiso, *Neuroscience: Exploring the Brain, Enhanced Edition*. Jones & Bartlett Learning, 2020.

[126] S. B. Meier, D. Tordera, A. Pertegás, C. Roldán-Carmona, E. Ortí, and H. J. Bolink, "Light-emitting electrochemical cells: recent progress and future prospects," *Mater. Today*, vol. 17, no. 5, pp. 217–223, Jun. 2014, doi: 10.1016/j.mattod.2014.04.029.

[127] H. Rudmann and M. F. Rubner, "Single layer light-emitting devices with high efficiency and long lifetime based on tris(2,2′ bipyridyl) ruthenium(II) hexafluorophosphate," *J. Appl. Phys.*, vol. 90, no. 9, pp. 4338–4345, Oct. 2001, doi: 10.1063/1.1409577.

[128] H. Rudmann, S. Shimada, and M. F. Rubner, "Solid-State Light-Emitting Devices Based on the Tris-Chelated Ruthenium(II) Complex. 4. High-Efficiency Light-Emitting Devices Based on Derivatives of the Tris(2,2‘-bipyridyl) Ruthenium(II) Complex," *J. Am. Chem. Soc.*, vol. 124, no. 17, pp. 4918–4921, May 2002, doi: 10.1021/ja012721j.

[129] Y. Hu and J. Gao, "Cationic effects in polymer light-emitting electrochemical cells," *Appl. Phys. Lett.*, vol. 89, no. 25, p. 253514, Dec. 2006, doi: 10.1063/1.2422877.

[130] Y. Shen *et al.*, "Improving light-emitting electrochemical cells with ionic additives," *Appl. Phys. Lett.*, vol. 102, no. 20, p. 203305, May 2013, doi: 10.1063/1.4807674.

[131] A. Munar, A. Sandström, S. Tang, and L. Edman, "Shedding Light on the Operation of Polymer Light-Emitting Electrochemical Cells Using Impedance Spectroscopy," *Adv. Funct. Mater.*, vol. 22, no. 7, pp. 1511–1517, 2012, doi: https://doi.org/10.1002/adfm.201102687.

[132] "Discerning the Impact of a Lithium Salt Additive in Thin-Film Light-Emitting Electrochemical Cells with Electrochemical Impedance Spectroscopy | Langmuir." https://pubs.acs.org/doi/abs/10.1021/acs.langmuir.6b02415 (accessed Jan. 16, 2021).

[133] S. B. Meier, D. Hartmann, A. Winnacker, and W. Sarfert, "The dynamic behavior of thin-film ionic transition metal complex-based light-emitting electrochemical cells," *J. Appl. Phys.*, vol. 116, no. 10, p. 104504, Sep. 2014, doi: 10.1063/1.4895060.

[134] Y. V. Pershin and M. D. Ventra, "Memory effects in complex materials and

nanoscale systems," *Adv. Phys.*, vol. 60, no. 2, pp. 145–227, Apr. 2011, doi: 10.1080/00018732.2010.544961.

[135] S. van Reenen, R. A. J. Janssen, and M. Kemerink, "Dynamic Processes in Sandwich Polymer Light-Emitting Electrochemical Cells," *Adv. Funct. Mater.*, vol. 22, no. 21, pp. 4547–4556, 2012, doi: https://doi.org/10.1002/adfm.201200880.

[136] "Solid-State Organic Light-Emitting Diodes Based on Tris(2,2'-bipyridine)ruthenium(II) Complexes | Journal of the American Chemical Society." https://pubs.acs.org/doi/full/10.1021/ja000666t (accessed Jan. 17, 2021).

[137] Y. Halawani, B. Mohammad, D. Homouz, M. Al-Qutayri, and H. Saleh, "Embedded memory design using memristor: Retention time versus write energy," in *2013 IEEE 20th International Conference on Electronics, Circuits, and Systems (ICECS)*, Dec. 2013, pp. 41–44. doi: 10.1109/ICECS.2013.6815340.

[138] S. G. Hu *et al.*, "Emulating the paired-pulse facilitation of a biological synapse with a NiOx-based memristor," *Appl. Phys. Lett.*, vol. 102, no. 18, p. 183510, May 2013, doi: 10.1063/1.4804374.

[139] "Neuromorphic Processing of Pressure Signal Using Integrated Sensor-Synaptic Device Capable of Selective and Reversible Short- and Long-Term Plasticity Operation | ACS Applied Materials & Interfaces." https://pubs.acs.org/doi/abs/10.1021/acsami.0c03904 (accessed Jan. 17, 2021).

[140] "Electret-Based Organic Synaptic Transistor for Neuromorphic Computing | ACS Applied Materials & Interfaces." https://pubs.acs.org/doi/abs/10.1021/acsami.9b22925 (accessed Jan. 17, 2021).

[141] Q. Liu *et al.*, "Fully Printed All-Solid-State Organic Flexible Artificial Synapse for Neuromorphic Computing," *ACS Appl. Mater. Interfaces*, vol. 11, no. 18, pp. 16749–16757, May 2019, doi: 10.1021/acsami.9b00226.

[142] R. S. Zucker and W. G. Regehr, "Short-Term Synaptic Plasticity," *Annu. Rev. Physiol.*, vol. 64, no. 1, pp. 355–405, 2002, doi: 10.1146/annurev.physiol.64.092501.114547.